Supporting Information

Unusual Near Infrared (NIR) Fluorescent Palladium(II) Macrocyclic Complexes Containing M-C Bond with the Bioimaging Capability

Yuhang Yao,[a] Chun-Liang Hou,[b] Zi-Shu Yang,[a] Guangliu Ran,[c] Lei Kang,[d] Cuicui Li,[d] Wenkai Zhang,[c,*] Jing Zhang[b,*] and Jun-Long Zhang[a,*]

FAX: (86)10-62767034
Email: wkzhang@bnu.edu.cn
zhangj271@ucas.ac.cn
zhangjunlong@pku.edu.cn

[a]Beijing National Laboratory for Molecular Sciences, State Key Laboratory of Rare Earth Materials Chemistry and Applications, College of Chemistry and Molecular Engineering, Peking University, Beijing 100871, Republic of China.

[b]Center of Materials Science and Optoelectronics Engineering, College of Materials Science and Opto-Electronic Technology, University of Chinese Academy of Sciences, Beijing 100049, Republic of China.

[c]Center for Advanced Quantum Studies, Department of Physics and Applied Optics Beijing Area Major Laboratory, Beijing Normal University, Beijing 100875, People's Republic of China.

[d]Department of Nuclear Medicine, Peking University First Hospital, Beijing 100034, People's Republic of China.

Outline

1. Supporting information for synthesis and characterization.

General information.

All reagents and materials were purchased from commercial suppliers and used as received unless otherwise indicated. UV-vis spectra were recorded on an Agilent 8453 UV-vis spectrometer equipped with an Agilent 89090A thermostat (± 0.1 ^{o}C). ESI-MS spectra were recorded on Bruker APEX IV Fourier Transform Ion Cyclotron Resonance Mass Spectrometer using electrospray ionization. Mass spectrometric simulations were carried out using the IsoPro v3.0 package. MALDI-TOF-MS were recorded on an AB Sciex 5800 MALDI-TOF/TOF mass spectrometer. ^{1}H and ^{13}C NMR spectra were recorded on a Bruker-400 MHz instrument, ^{19}F NMR spectra were recorded on a Bruker-500 MHz instrument. ^{1}H and ^{13}C NMR spectra were referenced to tetramethylsilane as an internal standard. For the ^{19}F NMR spectra, trifluoroacetic acid (-77.5 ppm) was used as an external reference. Fluorescence spectra, lifetime and steady state spectra were recorded using FLS-920 and FLS-980 spectrometers. The absolute quantum yields were determined using an integrating sphere on the FLS-980 spectrometer. IR spectra were recorded on a Tensor 27 FTIR or a Spectrum Spotlight 200 FT-IR microscopic. Transmission electron microscopy was obtained with a JEOL JEM-2100F Field-emission High Resolution Transmission Electron Microscope operated at 200 kV. HeLa cells were obtained from Peking University Health Science Center. Confocal fluorescence microscopy of living cells was performed using an ISS laser scanning CONFOCAL nanoscope Q2.

All animal experiments were implemented in accordance with the Animal Management Rules of the Ministry of Health of the People's Republic of China (Document NO. 55, 2001) and were approved and according to the guidelines from Laboratory Animal Ethics Committee of Peking University First Hospital (Peking University, China) (Approval ID: J201859).

Synthesis.

2,5-bis((5-bromo-1H-pyrrol-2-yl)(perfluorophenyl)methyl)-1H-pyrrole

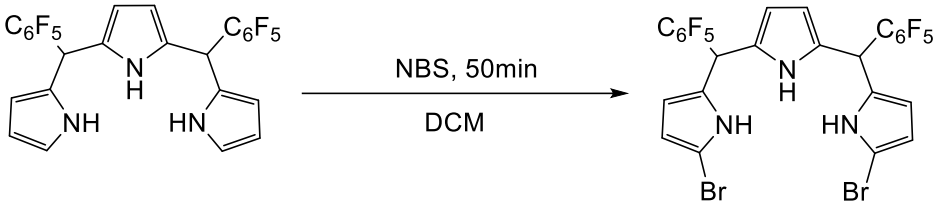

Scheme S1. Synthetic procedure of (i)

A solution of 132 mg (0.724 mmol, 2 equivalents) N-bromosuccinimide (NBS) in anhydrous dichloromethane (10 mL) was slowly added to a solution of 200mg (0.362 mmol, 1 equivalent) tripyrrole in anhydrous dichloromethane (10 mL) in a two-necked flask under conditions of -78 ℃ with the nitrogen protection. The reaction was stirred for 50 min.

2,5-bis((Z)-(5-bromo-2H-pyrrol-2-ylidene)(perfluorophenyl)methyl)-1H-pyrrole

Scheme S2. Synthetic procedure of (ii)

After stirring for 50 min, the reaction was restored up to room temperature, then 245 mg (1.086 mmol, 3 equivalents) 2,3-dichloro-5,6-dicyanobenzoquinone (DDQ) was directly added to the two-necked flask. The solution was stirred for 10 to 15 minutes, then concentrated under reduced pressure and purified by a flash silica-gel column chromatography (eluent: petroleum ether/CH_2Cl_2, 1:1) to obtain the crude products.

(1^1E,1^2Z,5^1E,5^2Z)-2,4-bis(perfluorophenyl)-1^2H,3^1H,5^2H-6,8-dioxa-1,3,5(2,5)-tripyrrola-7(1,3)-benzenacyclooctaphane (1)

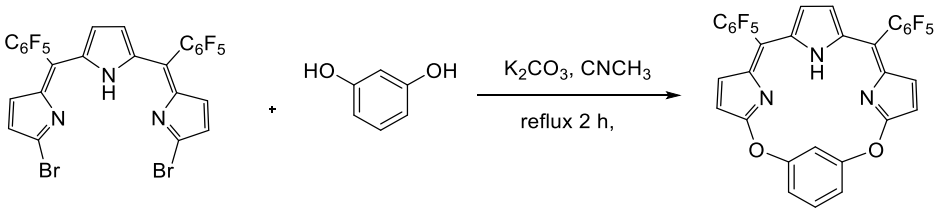

Scheme S3. Synthetic procedure of **1**

The previous crude products were added to a solution of 32 mg (0.290 mmol, 0.8 equivalents) resorcinol and 120 mg (0.869 mmol, 2.4 equivalents) anhydrous potassium carbonate in anhydrous acetonitrile (20 mL). The reaction was stirring and refluxing for 2 h under a nitrogen atmosphere. Then the solution was concentrated under reduced pressure and purified by a silica-gel column chromatography (eluent:

petroleum ether/CH_2Cl_2, 10:1) to give a red solid of compound **1** (120 mg).

1: Yield: 48.2%; ^{1}H NMR (400 MHz, Chloroform-*d*) δ 12.74 (s, 1H), 9.34 (s, 1H), 7.35 (s, 1H), 7.04 (s, 2H), 6.62 (s, 2H), 6.45 (s, 2H), 5.93 (s, 2H). ^{13}C NMR (101 MHz, Chloroform-*d*) δ 175.0, 153.4, 148.1, 136.3, 135.9, 129.0, 121.9, 120.7, 118.9, 117.4, 116.4, 77.0, 32.0, 29.7. ^{19}F NMR (377 MHz, Chloroform-*d*) δ -138.4 (dd, *J* = 22.5, 7.0 Hz), -152.2 (t, *J* = 20.9 Hz), -160.8 (td, *J* = 21.8, 6.7 Hz). MALDI-TOF-MS m/z: Calcd. For $C_{32}H_{11}F_{10}N_3O_2$ $[M]^+$ 659.0686, found 659.0667. IR (cm^{-1}): 3315, 2019, 1651, 1521, 1447, 1329, 1259, 1153, 1060, 905, 828, 764, 576. UV-vis absorption (CH_2Cl_2): λ_{max} (lg ε) = 323 (4.71), 514 (4.40), 541 (4.41).

(1^{1}E,1^{2}Z,5^{1}E,5^{2}Z)-N,N-dimethyl-2,4-bis(perfluorophenyl)-1^{2}H,3^{1}H,5^{2}H-6,8-dioxa-1,3,5(2,5)-tripyrrola-7(1,3)-benzenacyclooctaphan-75-amine (2)

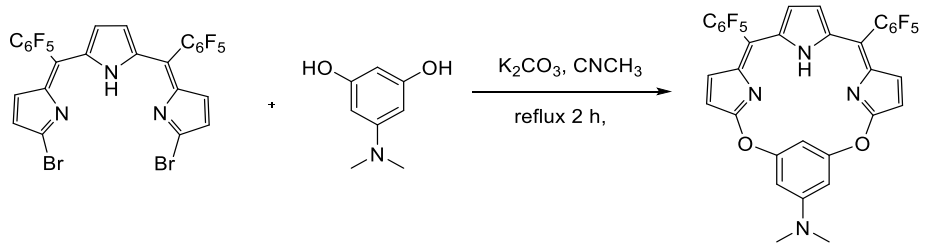

Scheme S4. Synthetic procedure of **2**

The previous crude products were added to a solution of 44 mg (0.290 mmol, 0.8 equivalents) 5-(dimethylamino)-1,3-benzenediol and 120 mg (0.869 mmol, 2.4 equivalents) anhydrous potassium carbonate in anhydrous acetonitrile (20 mL). The reaction was stirring and refluxing for 2 h under a nitrogen atmosphere. Then the solution was concentrated under reduced pressure and purified by a silica-gel column chromatography (eluent: petroleum ether/CH_2Cl_2, 5:1) to give a red solid of compound **2** (85 mg)

2: Yield: 34.1%; ^{1}H NMR (400 MHz, Chloroform-*d*) δ 12.69 (s, 1H), 8.54 (s, 1H), 6.60 (s, 2H), 6.43 (s, 2H), 6.35 (s, 2H), 5.90 (s, 2H), 2.96 (s, 6H). ^{13}C NMR (101 MHz, Chloroform-*d*) δ 175.3, 154.0, 150.9, 136.3, 135.8, 121.9, 118.7, 109.4, 101.3, 40.3. ^{19}F NMR (471 MHz, Chloroform-*d*) δ -138.4 – -138.5 (m), -152.4 (t, *J* = 20.9 Hz), -161.0 (td, *J* = 21.9, 7.0 Hz). MALDI-TOF-MS m/z: Calcd. For $C_{34}H_{16}F_{10}N_4O_2$ $[M]^+$ 701.1029, found 701.1012. IR (cm^{-1}): 3339 1069, 1552, 1497, 1384, 1260, 1147, 1061, 907, 821, 708. UV-vis absorption(CH_2Cl_2): λ_{max} (lg ε) = 332 (4.75), 512 (4.42), 541 (4.39).

(1^{1}E,1^{2}Z,5^{1}E,5^{2}Z)-2,4-bis(perfluorophenyl)-1^{2}H,3^{1}H,5^{2}H-6,8-dioxa-1,3,5(2,5)-tripyrrola-7(1,3)-benzenacyclooctaphane-7^5-carbonitrile (3)

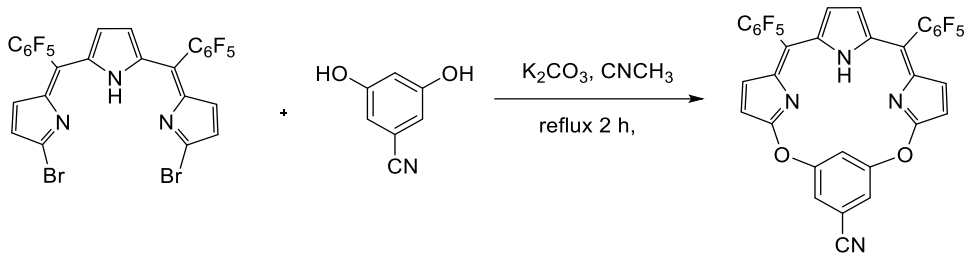

Scheme S5. Synthetic procedure of **3**

The previous crude products were added to a solution of 39 mg (0.290 mmol, 0.8 equivalents) 3,5-dihydroxycyanobenzene and 120 mg (0.869 mmol, 2.4 equivalents) anhydrous potassium carbonate in anhydrous acetonitrile (20 mL). The reaction was stirring and refluxing for 2 h under a nitrogen atmosphere. Then the solution was concentrated under reduced pressure and purified by a silica-gel column chromatography (eluent: petroleum ether/CH_2Cl_2, 2:1) to give a red solid of compound **3** (129 mg)

3: Yield: 52.1%; ^{1}H NMR (400 MHz, Chloroform-*d*) δ 12.60 (s, 1H), 9.66 (t, *J* = 2.2 Hz, 1H), 7.32 (d, *J* = 2.2 Hz, 2H), 6.67 (d, *J* = 4.8 Hz, 2H), 6.46 (d, *J* = 4.8 Hz, 2H), 5.99 (d, *J* = 2.3 Hz, 2H). ^{13}C NMR (101 MHz, Chloroform-*d*) δ 136.4, 136.2, 136.2, 133.5, 121.8, 121.8, 119.8, 119.7, 118.8, 117.3, 77.0. ^{19}F NMR (471 MHz, Chloroform-*d*) δ -138.2 – -138.4 (m), -152.2 (t, *J* = 20.8 Hz), -160.7 (td, *J* = 21.7, 6.7 Hz). MALDI-TOF-MS m/z: Calcd. For $C_{33}H_{10}F_{10}N_4O_2$ $[M]^+$ 684.0638, found 684.0625. IR (cm^{-1}): 3445, 1606, 1524, 1387, 1309, 1259 1188, 909, 830, 767, 708, 570. UV-vis absorption (CH_2Cl_2): λ_{max} (lg ε) = 324 (4.58), 513 (4.41), 541 (4.34).

(1^{1}E,1^{2}Z,5^{1}E,5^{2}Z)-7^4-methoxy-2,4-bis(perfluorophenyl)-1^{2}H,3^{1}H,5^{2}H-6,8-dioxa-1,3,5(2,5)-tripyrrola-7(1,3)-benzenacyclooctaphane (4)

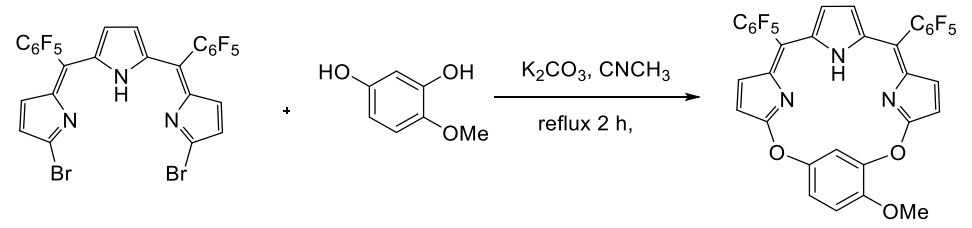

Scheme S6. Synthetic procedure of **4**

The previous crude products were added to a solution of 41 mg (0.290 mmol, 0.8 equivalents) 4-methoxybenzene-1,3-diol and 120 mg (0.869 mmol, 2.4 equivalents) anhydrous potassium carbonate in anhydrous acetonitrile (20 mL). The reaction was stirring and refluxing for 2 h under a nitrogen atmosphere. Then the solution was concentrated under reduced pressure and purified by a silica-gel column chromatography (eluent: petroleum ether/CH_2Cl_2, 3:1) to give a red solid of compound **4** (80 mg)

4: Yield: 32.2%; ^{1}H NMR (400 MHz, Chloroform-*d*) δ 12.68 (s, 1H), 9.05 (s, 1H), 6.96 (s, 2H), 6.61 (s, 2H), 6.53 (s, 2H), 5.90 (s, 2H), 3.88 (s, 3H). ^{13}C NMR (101 MHz,

Chloroform-*d*) δ 148.1, 145.7, 136.4, 136.3, 136.1, 123.3, 121.6, 118.9, 118.8, 117.7, 111.7, 77.0, 56.4. ^{19}F NMR (471 MHz, Chloroform-*d*) δ -138.5 (dd, *J* = 23.0, 7.7 Hz), -152.3 (q, *J* = 20.6 Hz), -160.9 (ddd, *J* = 21.4, 14.8, 7.5 Hz). MALDI-TOF-MS m/z: Calcd. For $C_{33}H_{13}F_{10}N_3O$ $[M]^+$ 689.0791 found 689.0770. IR (cm^{-1}): 3443, 1608, 1523, 1497, 1386, 1329, 1263, 1181, 1062, 989, 767. UV-vis absorption (CH_2Cl_2): λ_{max} (lg ε) = 325 (4.68), 514 (4.37), 538 (4.41).

(1^{1}E,1^{2}Z,5^{1}E,5^{2}Z)-2,4-bis(perfluorophenyl)-1^{2}H,3^{1}H,5^{2}H-6,8-dioxa-1,3,5(2,5)-tripyrrola-7(1,3)-benzenacyclooctaphane-7^4-carbonitrile (5)

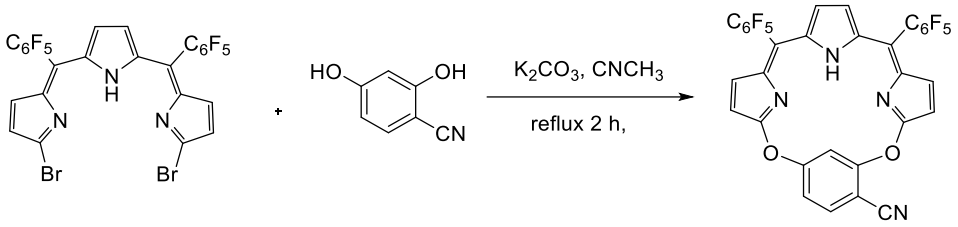

Scheme S7. Synthetic procedure of **5**

The previous crude products were added to a solution of 39 mg (0.290 mmol, 0.8 equivalents) 2,4-dihydroxybenzonitrile and 120 mg (0.869 mmol, 2.4 equivalents) anhydrous potassium carbonate in anhydrous acetonitrile (20 mL). The reaction was stirring and refluxing for 2 h under a nitrogen atmosphere. Then the solution was concentrated under reduced pressure and purified by a silica-gel column chromatography (eluent: petroleum ether/CH_2Cl_2, 2:1) to give a red solid of compound **5** (126 mg).

5: Yield: 50.7%; ^{1}H NMR (400 MHz, Chloroform-*d*) δ 12.62 (s, 1H), 9.81 (s, 1H), 7.66 (s, 1H), 7.08 (s, 1H), 6.71 (s, 2H), 6.48 (s, 2H), 6.02 (s, 2H). ^{13}C NMR (101 MHz, Chloroform-*d*) δ 173.4, 157.0, 147.9, 147.7, 136.4, 136.2, 136.1, 133.5, 121.8, 119.8, 119.7, 118.7, 117.3, 115.0, 101.3. ^{19}F NMR (471 MHz, Chloroform-*d*) δ -138.3 – -138.5 (m), -151.6 (q, *J* = 20.2 Hz), -160.4 -160.6 (m). MALDI-TOF-MS m/z: Calcd. For $C_{33}H_{10}F_{10}N_4O_2$ $[M+H]^+$ 685.0717, found 685.0727. IR (cm^{-1}): 3443, 1605, 1551, 1524, 1497, 1386, 1260, 1187, 1040, 989 866, 709. UV-vis absorption (CH_2Cl_2): λ_{max} (lg ε) = 331 (4.46), 541 (4.51).

Pd-1

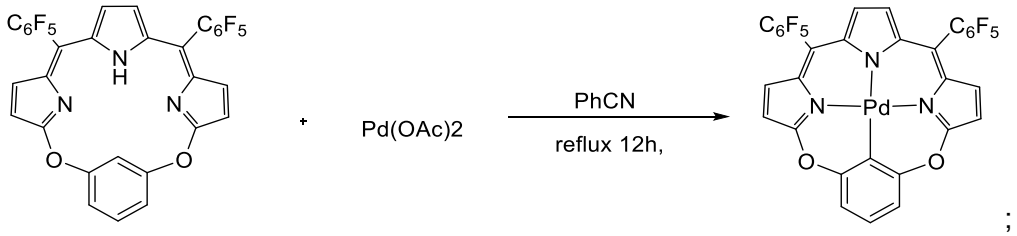

;

Scheme S8. Synthetic procedure of **Pd-1**

A 50 of Schlenk flask was charged with 50 mg Compound **1** (0.076 mmol, 1 equivalents), 170 mg palladium(II) acetate ($Pd(OAc)_2$, 0.76 mmol, 10 equivalents) and 20 mL degassed benzonitrile under a stream of nitrogen. The solution was kept stirring

and refluxing under nitrogen protection until the solution becomes green. The solution was concentrated under reduced pressure to afford a crude product. The crude product was purified by silica gel chromatography eluted with ether: CH_2Cl_2 = 8: 1 to give product (10 mg) as green solid.

Pd-1: Yield: 17.5%; ^{1}H NMR (400 MHz, Methylene Chloride-d_2) δ 7.24 (s, 1H), 6.98 (s, 2H), 6.76 (s, 2H), 6.53 (s, 2H), 6.31 (s, 2H). ^{13}C NMR (101 MHz, Chloroform-*d*) δ 163.2, 136.1, 129.0, 122.1, 115.7, 113.7. ^{19}F NMR (377 MHz, Chloroform-*d*) δ -137.9 – -138.7 (m), -152.0 (t, *J* = 20.9 Hz), -160.6 (td, *J* = 22.2, 21.8, 6.8 Hz). MALDI-TOF-MS m/z: Calcd. For $C_{32}H_9F_{10}N_3O_2Pd$ $[M]^+$ 762.9564, found 762.9564. IR (cm^{-1}): 3422, 2923, 1609, 1575, 1493, 1302 1256, 1114, 1068, 932, 841, 763,706. UV-vis absorption(CH_2Cl_2): λ_{max} (lg ε) = 372 (4.72), 638 (4.34), 693 (4.44).

Pd-2

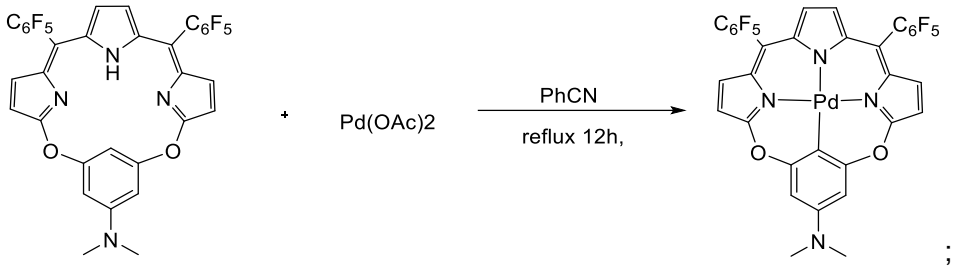

;

Scheme S9. Synthetic procedure of **Pd-2**

A 50 of Schlenk flask was charged with 50 mg Compound **2** (0.071 mmol, 1 equivalents), 160 mg palladium(II) acetate ($Pd(OAc)_2$, 0.71 mmol, 10 equivalents) and 20 mL degassed benzonitrile under a stream of nitrogen. The solution was kept stirring and refluxing under nitrogen protection until the solution becomes green. The solution was concentrated under reduced pressure to afford a crude product. The crude product was purified by silica gel chromatography eluted with ether: CH_2Cl_2 = 3: 1 to give product (8 mg) as green solid.

Pd-2: Yield: 14.0%; ^{1}H NMR (400 MHz, Chloroform-*d*) δ 6.72 (s, 2H), 6.47 (s, 2H), 6.42 (s, 2H), 6.26 (s, 2H), 2.96 (s, 6H). ^{13}C NMR (101 MHz, Chloroform-*d*) δ 135.8, 122.3, 116.6, 98.4, 77.0, 40.4, 29.7. ^{19}F NMR (471 MHz, Chloroform-*d*) δ -138.2 – -138.4 (m), -152.2 (t, *J* = 20.8 Hz), -160.8 (td, *J* = 21.7, 6.8 Hz). MALDI-TOF-MS m/z: Calcd. For $C_{34}H_{14}F_{10}N_4O_2Pd$ $[M]^+$ 805.9986, found 805.9999 IR (cm^{-1}): 3437, 2924, 1594, 1461, 1328, 1189, 1067, 990, 838, 791, 507. UV-vis absorption(CH_2Cl_2): λ_{max} (lg ε) = 368 (4.52), 646 (4.10), 697 (4.15).

Pd-3

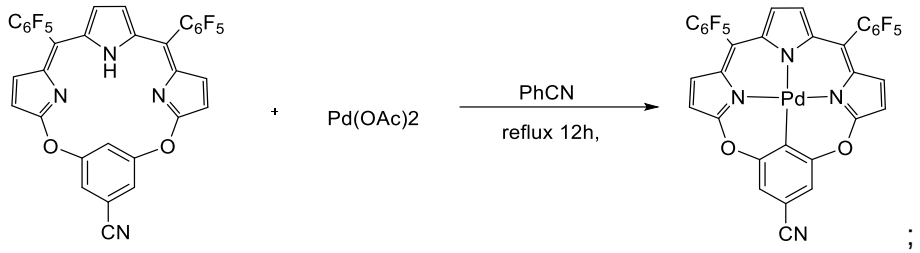

;

Scheme S10. Synthetic procedure of **Pd-3**

A 50 of Schlenk flask was charged with 50 mg Compound **1** (0.073 mmol, 1 equivalents), 286 mg palladium(II) acetate ($Pd(OAc)_2$, 0.73 mmol, 10 equivalents) and 20 mL degassed benzonitrile under a stream of nitrogen. The solution was kept stirring and refluxing under nitrogen protection until the solution becomes green. The solution was concentrated under reduced pressure to afford a crude product. The crude product was purified by silica gel chromatography eluted with ether: CH_2Cl_2 = 8: 1 to give product (15 mg) as green solid.

Pd-3: Yield: 23.4%; ^{1}H NMR (400 MHz, Methylene Chloride-d_2) δ 7.04 (s, 2H), 6.84 (s, 2H), 6.50 (s, 2H), 6.27 (s, 2H). ^{13}C NMR (101 MHz, Chloroform-*d*) δ 140.2, 135.8, 122.3, 116.6, 98.4, 77.0, 40.4, 29.7. ^{19}F NMR (471 MHz, Chloroform-*d*) δ -138.2 – -138.3 (m), -152.0 (t, *J* = 20.9 Hz), -160.6 (td, *J* = 21.6, 6.7 Hz). MALDI-TOF-MS m/z: Calcd. For $C_{33}H_8F_{10}N_4O_2Pd$ $[M]^+$ 787.9517 found 787.9510. IR (cm^{-1}): 3434, 2961, 1786, 1604, 1525, 1423, 1341, 1263, 1166, 1071, 939, 802, 719. UV-vis absorption(CH_2Cl_2): λ_{max} (lg ε) = 370 (4.51), 621 (4.10), 674 (4.30).

Pt-1

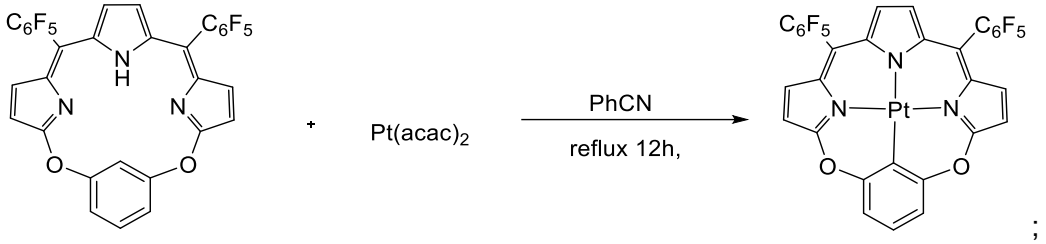

;

Scheme S11. Synthetic procedure of **Pt-1**

A 50 of Schlenk flask was charged with 50 mg Compound **1** (0.076 mmol, 1 equivalents), 170 mg platinum(II) bis(acetylacetonate) ($Pt(acac)_2$, 0.76 mmol, 10 equivalents) and 20 mL degassed Benzonitrile under a stream of nitrogen. The solution was kept stirring and refluxing under nitrogen protection until the solution becomes green. The solution was concentrated under reduced pressure to afford a crude product. The crude product was purified by silica gel chromatography eluted with ether: CH_2Cl_2=10: 1 to give product (10 mg) as green solid.

Pt-1: Yield: 34.1%; ^{1}H NMR (400 MHz, Chloroform-*d*) δ 7.38 (s, 1H), 7.09 (s, 2H), 6.89 (d, *J* = 18.5 Hz, 2H), 6.75 (d, *J* = 15.9 Hz, 2H), 6.62 (s, 2H). ^{13}C NMR (101 MHz, Chloroform-*d*) δ 163.3, 152.3, 138.3, 136.1, 131.9, 124.0, 122.1, 115.7, 113.7, 100.1, 77.0. ^{19}F NMR (471 MHz, Chloroform-*d*) δ -137.9 – -138.2 (m), -151.8 (t, *J* = 20.8 Hz), -160.5 (td, *J* = 21.5, 6.7 Hz). MALDI-TOF-MS m/z: Calcd. For $C_{33}H_9F_{10}N_3O_2Pt$ $[M]^+$ 852.0183, found 852.0151. IR (cm^{-1}): 3441, 2923, 1599, 1495, 1011, 932, 785, 706. UV-vis absorption(CH_2Cl_2): λ_{max} (lg ε) = 372 (4.57), 641 (4.15), 693 (4.23).

2. Supporting information for photophysical properties measurement, cell experiments and computation details.

X-ray diffraction measurement.

X-ray diffraction data were collected on *Rigaku XtaLAB Pro: Kappa single system* equipped with Mo K*α* source. Suitable crystal was mounted on the diffractometer and cooled down under a nitrogen stream as soon as possible to protect from desolvent. *CrysAlisPro* program was employed for data processing. The structure was solved using *SHELXT 2014* program[1] and refined against F^2 anisotropically for all non-hydrogen atoms by full matrix least-squares method using *SHELXL 2016* program in an Olex2 GUI.[2] *Platon* program package[3] was employed for squeeze processing.

Photophysical properties measurement.

Emission, excitation spectra and lifetime were recorded on Edinburgh Analytical Instruments FLS980 and FLS920 lifetime and steady state spectrometer equipped with a 450 W Xe lamp and PMT R928 for visible emission spectrum.

Quantum yields determination.

The absolute quantum yields were determined on an Edinburgh Analytical Instrument FLS-980 equipped with an integrating sphere.

Nanosecond (ns-TA) and femtosecond (fs-TA) transient absorption spectroscopes.

The nanosecond transient absorption spectra and triplet excited state decay dynamics were recorded on an Edinburgh LP920 spectrometer combined with OPO laser excitation pulse (10 Hz, 2 mJ pulse^{-1}). The femtosecond transient spectra and singlet excited state decay dynamics were recorded in HARPIA spectrometer equipped with PHAROS femtosecond laser.

Cell culture

HeLa cells were cultured in Dulbecco's modified Eagle's medium (DMEM, Corning) supplemented with 10% fetal bovine serum (FBS) and 1% penicillin-streptomycin. HeLa cells were grown at 37 °C under a humidified atmosphere containing 5% CO_2.

Cell imaging

Cells were placed on sterile glass coverslips in cell culture dishes containing complete media and allowed to grow to about 80% confluence. A stock suspension of the NIR-MSNs in PBS buffer was prepared at around 0.5 mM. The suspension was diluted to a final concentration of 10 μM (concentration of Pd^{2+}) by the complete growth medium. After incubation for 12 h, the cells were incubated with 75 nM LysoTracker Green DND-26 for another 30 min. Then the cells were washed with PBS buffer twice before the confocal experiments. The NIR-MSNs confocal images were acquired in Channel 1, using a Semrock 776 nm long-pass filter. LysoTracker Green was excited at 488 nm and images were collected in Channel 2, using a Semrock 530/43 nm band-pass filter (EM2). For the intracellular pH experiments, the cells were incubated with a high K^+ buffer (30 mM NaCl, 120 mM KCl, 1 mM $CaCl_2$, 0.5 mM $MgSO_4$, 1 mM NaH_2PO_4, 5 mM glucose, 20 mM HEPES, and 20 mM NaOAc) at various pH values (6–9) in the presence of 10 mM of nigericin. Then the cells were incubated for 30 min at 37 ºC before the fluorescence imaging measurements.

Cytotoxicity assay

HeLa cells were seeded in flat-bottomed 96-well plates, 10^4 cells per well, with 200 μL complete culture media in the dark for 24 h. Cells were incubated with 1~16 μM (concentration of Pd^{2+}) for another 24 h in the dark while wells containing no cells were set as the controls. After washing three times with PBS, 10 μL Cell Counting Kit-8 (CCK-8) solution and 90 μL PBS were added per well. After 2 h, the absorbance at 450 nm was read by a 96-well plate reader. The viability of HeLa cells was calculated by the following equation:

$$\mathrm{CV} = \frac{A_s - A_b}{A_c - A_b} \times 100\% \quad \text{(S1)}$$

CV stands for the viability of cells, A_s, A_c, and A_b stand for the absorbance of cells

containing the studied complexes, cell control (no treated cells), and blank control (wells containing neither cells nor the studied complexes), respectively.

***In vivo* imaging**

Seven-week-old BABLc male mice were obtained from Peking University First Hospital (Beijing, China) and were housed under standard environmental conditions. All animal procedures were performed in accordance with the guidelines from Laboratory Animal Ethics Committee of Peking University First Hospital (Peking University, China) (Approval ID: J201859). Mice were randomly selected from cages for all of the experiments. Imaging was performed with guidelines from Laboratory Animal Ethics Committee of Peking University First Hospital (Peking University, China) (Approval ID: J201859).

The PBS suspension of **Pd-1-MSN-F127** and **Pd-3-MSN-F127** (100 uL, 0.1 mmol/L) were injected intravenously into the mice via tail vein. A preliminary fluorescence image was acquired immediately after injection in an *in vivo* Imaging System (IVIS SPECTRUM). Mice were imaged again at 6, 24, 48, 96 h for comparison. After 96 h, mice were sacrificed and dissected, and the major organs were removed for *ex vivo* imaging.

Theoretical and computational details.

In this work, we performed geometry optimizations for ground (S_0) and excited states (S_1 and T_1) followed by harmonic vibrational frequencies calculation with hybrid density functional, B3LYP,[4] using the program package Gaussian 09 (Revision E.01)[5]. The 6-311G(d) basis set[6] was used for all atoms except Pd and Pt atoms, which was described by the LanL2DZ[7] and SDD[8] pseudopotential and its accompanying basis set respectively. Frequency calculations were performed on the optimized structures to ensure that they were minimum energy structures by the absence of imaginary frequency. Stability calculations were also performed for all the optimized structures to ensure that all the wavefunctions obtained were stable. Vertical transition energies were computed using the linear response TDDFT (LR-TDDFT). Charge decomposition analysis (CDA) was performed using Multiwfn 3.4.1 in the B3LYP/6-311G(d)/Lanl2DZ/SDD level to calculate the composition of molecular orbitals. The natural localized molecular orbital (NLMO) analysis was performed on the optimized structures of ground states using NBO 5.0.[9] The spin-orbit coupling (SOC) integrals between the spin state S_n and T_m, $\langle T_m | \hat{H}_{SO} | S_n \rangle$, were estimated using effective atomic charge (Zeff) method by PySOC.[10]

The radiative decay rate constant, intersystem crossing rate constant and non-radiative decay rate constant were calculated by MOMAP program package using a thermal vibration correlation function formalism for the transition between two adiabatic electronic states considering displacements, distortions, and Duschinsky rotation of potential energy surfaces within the framework of multidimensional harmonic oscillator model and Franck-Condon principle.[11] The vibrationally resolved electronic spectra were simulated by FCclasses 2.1 also under the the framework of multidimensional harmonic oscillator model and Franck-Condon principle.[12]

3. Supporting Tables and Figures.

Table S1. Crystal data and structure refinements.

Complex	**1** (CCDC: 1912139)	**Pd-1** (CCDC: 1912140)	**Pt-1** (CCDC: 1912141)
Molecular formula	$C_{32}H_{11}F_{10}N_3O_2$	$C_{32}H_9F_{10}N_3O_2Pd$	$C_{65}H_{19}Cl_3F_{20}N_6O_4Pt_2$
Formula wt. (g mol^{-1})	702.52	763.82	1824.39
Temperature (K)	180	180	180
Radiation (λ, Å)	0.71073	0.71073	0.71073
Crystal system	monoclinic	triclinic	orthorhombic
Space group	P_1	P_{-1}	P_{ca21}
a (Å)	11.1406(4)	10.6992(4)	12.2124(3)
b (Å)	14.7364(6)	15.7524(6)	14.5258(3)
c (Å)	36.6510(19)	16.7744(8)	32.7959(7)
α (º)	90	100.088(3)	90
β (º)	95.557(4)	97.914(3)	90
γ (º)	90	90.165(3)	90
Volume (Å^3)	5988.8(5)	2755.9(2)	5817.8(2)
Z	8	4	4
ρ_{calcd} (g cm^{-3})	1.558	1.841	2.083
μ (mm^{-1})	0.141	0.780	5.065
F(000)	2840	1496	3480
Crystal size (mm^3)	0.31×0.15×0.03	0.18×0.15×0.05	0.20×0.10×0.07
Theta range	2.945 to 27.449	1.922 to 27.485	2.179 to 27.485
Reflections collected	42310	34912	45097
Independent reflections	13697 [R(int) = 0.0568]	12641 [R(int) = 0.0367]	12165 [R(int) = 0.0424]
Completeness	99.71	99.90	99.90
Goodness-of-fit on F^2	1.035	1.082	1.026
Final R indices [R > 2σ (I)]	R1[a] = 0.0634 *w*R$_2$[b] = 0.1699	R1[a] = 0.0530 *w*R$_2$[b] = 0.1491	R1[a] = 0.0365 *w*R$_2$[b] = 0.0956
R indices (all data)	R1[a] = 0.1242 *w*R$_2$[b] = 0.1403	R1[a] = 0.0671 *w*R$_2$[b] = 0.1419	R1[a] = 0.0525 *w*R$_2$[b] = 0.0885
Largest diff. peak and hole (e Å^{-3})	0.322 and -0.305	2.348 and -1.517	2.430 and -0.873

Table S2. Photophysical data of **1-5**, **Pd-1~3** and **Pt-1**. [a]

Comp.	Absorption (λ_{max} [nm], lg ε [M^{-1} cm^{-1}])	Emission		
		λ_{max} [nm]	τ [ns] [b]	Φ_F [%] [c]
1	324 (4.71), 513 (4.40), 541 (4.41)	613, 661	1.10	5.23
2	324 (4.75), 511 (4.42), 541 (4.38)	618, 650	0.82 (71%), 2.38 (29%)	0.11
3	324 (4.58), 513 (4.41), 541 (4.34)	602, 646	0.75	4.91
4	325 (4.68), 514 (4.37), 538 (4.41)	674	0.16 (31%), 1.82 (69%)	0.15
5	331 (4.46), 541 (4.51)	600, 644	0.75 (94%), 2.47 (6%)	3.94
Pd-1	372 (4.72), 638 (4.34), 693 (4.44)	732, 792	1.06	6.00
Pd-2	368 (4.52), 646 (4.10), 697 (4.15)	767	0.26 (9%), 2.05 (91%)	<0.01
Pd-3	370 (4.51), 621 (4.10), 674 (4.30)	700, 758	2.40	14.0
Pt-1	372 (4.57), 641 (4.15), 693 (4.23)	729	0.17 (20%), 3.34 (80%)	<0.01

[a]All photophysical measurements were carried out in anhydrous CH_2Cl_2 at room temperature. [b]Lifetime measurements were performed by LifeSpec II ultra-fast picosecond time-resolved fluorescence spectrometer (260-1100 nm laser /77-500 K variable temperature). [c]Quantum yields were measured using an Edinburgh Analytical Instrument FLS-980 equipped with an integrating sphere. Fluorescence data were collected upon the excitation at 500 nm for ligands and 600 nm for complexes.

Table S3. Electrochemical redox potentials of **1**, **Pd-1** and **Pt-1**.[a]

Compound	E_{OX} /V	E_{RED} /V
1	1.25	-0.85, -1.03
Pd-1	1.45	-0.75, -1.18
Pt-1	1.25	-0.67, -1.11

[a]Cyclic voltammetry (CV) in nitrogen-saturated CH_2Cl_2 containing a 0.10 M tBu4N[PF6] supporting electrolyte. A Pt counter electrode, a 3 mm diameter glassy carbon working electrode, and an Ag/AgCl reference electrode were used. Scan rate: 100 mV s−1. T = 20 °C.

Table S4. Calculated absorption peak at S_0 optimized structures by TDDFT.

`	UV		
	Exp. /nm	**Comp. /nm (*f*)**	**Contribution**[a]
1	541	511 (0.3037)	H -> L (97%)
2	541	589 (0.0030)	H-1 -> L (100%)
3	541	566 (0.2218)	H -> L (98%)
4	538	589 (0.1474)	H -> L (93%) H-1 -> L (7%)
5	541	582 (0.1751)	H -> L (97%) H-1 -> L (3%)
Pd-1	693	655 (0.1457)	H -> L (97%) H-2 -> L (2%)
Pt-1	693	664 (0.1174)	H -> L (93%) H-2 -> L (7%)

[a] H and L indicate HOMO and LUMO respectively.

Table S5. Calculated vertical excitations in S_0 state optimized structures of **Pd-1** by TDDFT.[a]

No.	E (cm^{-1})	λ (nm)	Major Contribution	Minor Contribution
T_1	8622.1	1159.82	H -> L (99%)	
S_1	15262	655.21	H -> L (97%)	H-2 -> L (2%)
T_2	17397	574.81	H -> L+1 (67%) H-4 -> L (22%)	H-8 -> L (5%) H-11 -> L (3%)

[a] H and L indicate HOMO and LUMO respectively.

Table S6. Calculated vertical excitations in S_0 state optimized structures of **Pt-1** by TDDFT.[a]

No.	E (cm^{-1})	λ (nm)	Major Contribution	Minor Contribution
T_1	8797.6	1136.68	H -> L (99%)	
S_1	1505.5	664.24	H -> L (93%)	H-2 -> L (7%)
T_2	1564.4	639.24	H-2 -> L (95%)	

[a] H and L indicate HOMO and LUMO respectively.

Table S7. Adiabatic energy difference, d-orbital splittings, reorganiztion energy spin-orbit coupling matrix elements and photophysical rate constants of Pd-1 and Pt-1 obtained from DFT and TDDFT calculations.

Compound	Pd-1	Pt-1
ΔE_{ST} /eV [a]	0.82	0.60
Δdd^* /eV [b]	5.78	6.70
λ /cm^{-1} [c]	1770.94 1485.37	1677.05 1566.27
$\langle S_1 \lvert \hat{H}_{SOC} \rvert T_1 \rangle$ /cm^{-1} [d]	0.61	0.17
k_r /s^{-1} (S_1 -> S_0) [e]	8.11×10^6	5.13×10^6
k_{nr} /s^{-1} (S_1 -> S_0) [f]	4.04×10^7	7.46×10^7
k_{ISC} /s^{-1} (S_1 -> T_1) [g]	3.66×10^5	1.87×10^5

[a]Adiabatic energy difference between S_1 and T_1 state. [b]Splitting between the occupied and unoccupied d orbitals in the S_1 optimized structure. [c]Total reorganiztion energy of S_0 and S_1 state respectively. [d]Spin-orbit coupling matrix element between S_1 and T_1 state. [e]Fluorescent rate constant from S_1 state. [f]Non-radiative rate constant. [g]Intersystem crossing rate constant from S_1 to T_1 state.

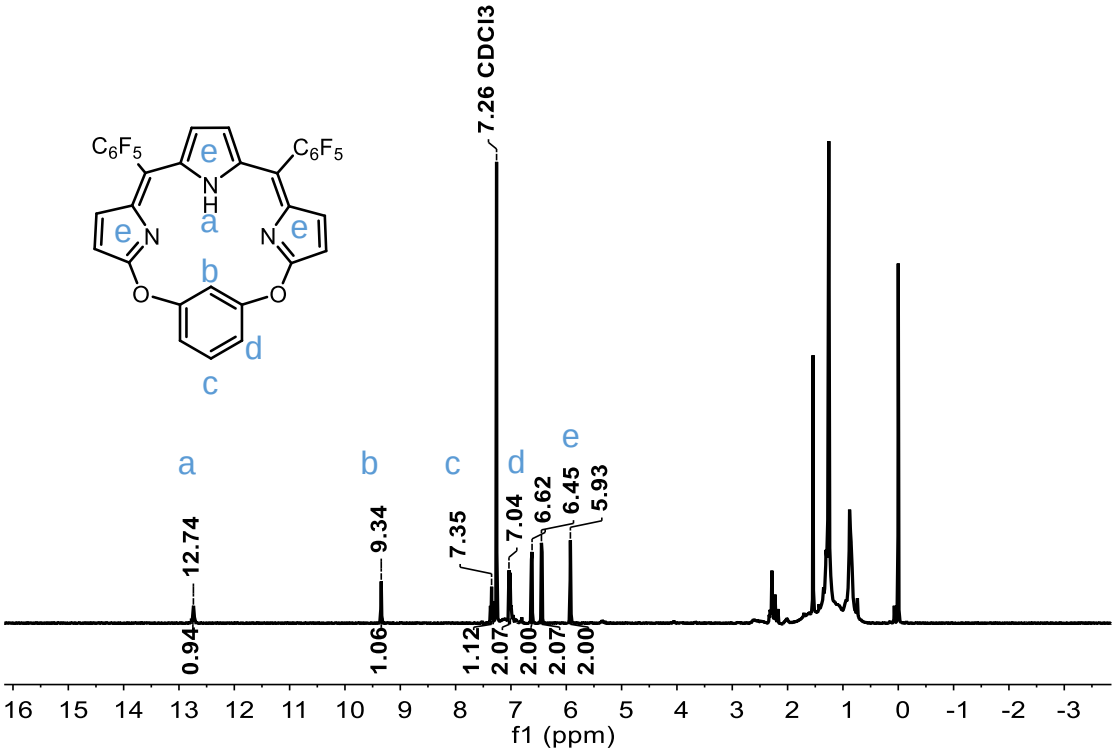

Figure S1. ^{1}H-NMR spectrum of **1** in $CDCl_3$.

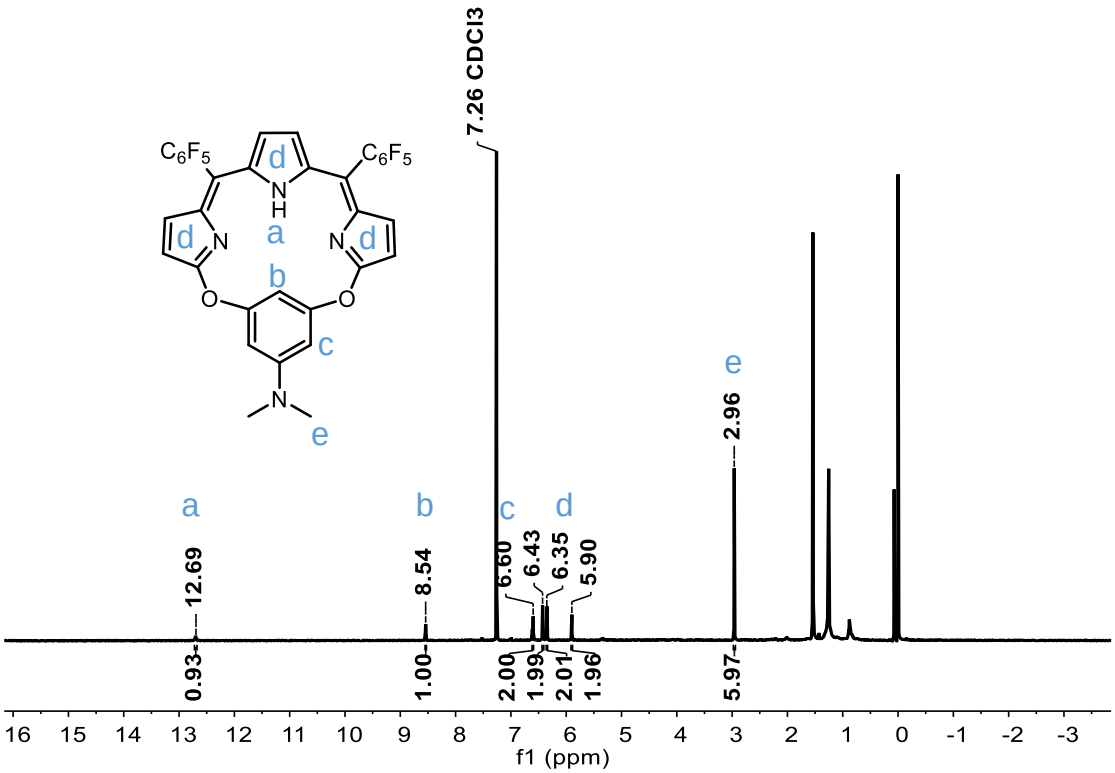

Figure S2. ^{1}H-NMR spectrum of **2** in $CDCl_3$.

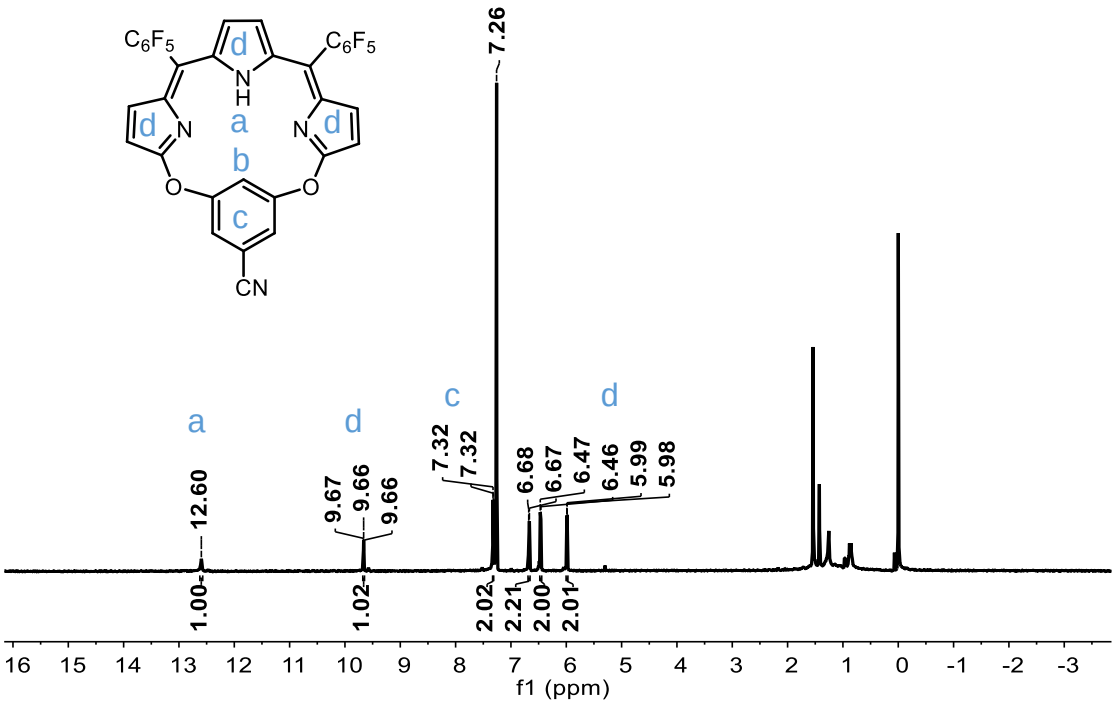

Figure S3. ^{1}H-NMR spectrum of **3** in $CDCl_3$.

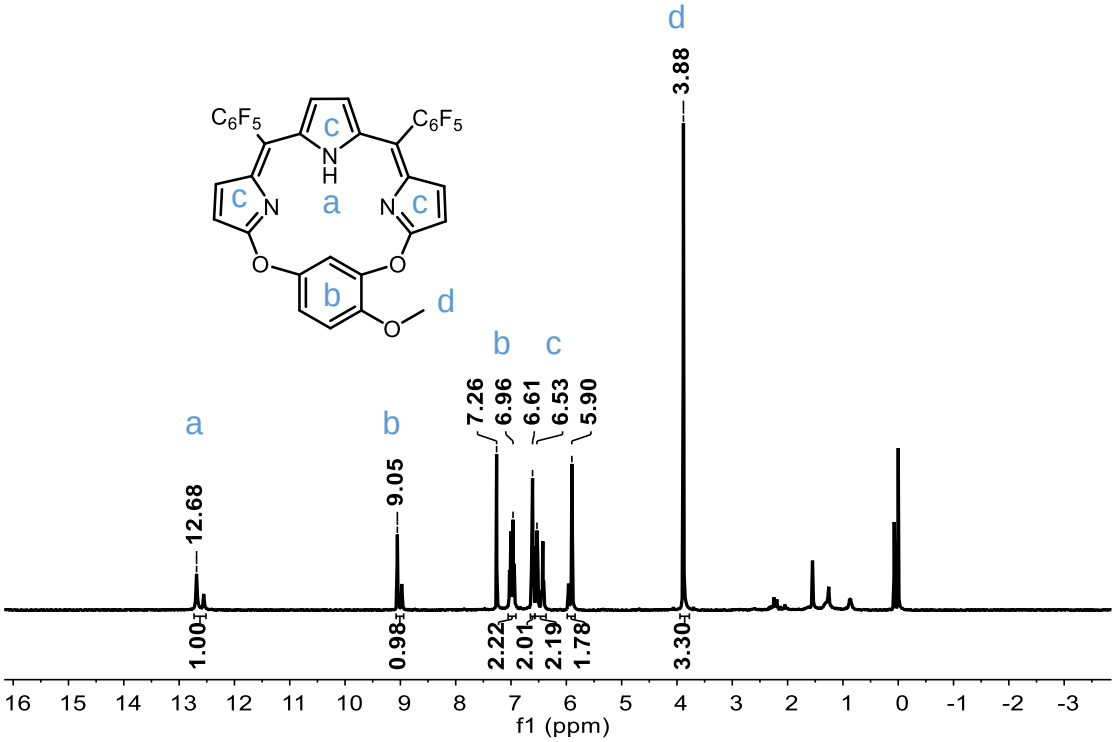

Figure S4. ^{1}H-NMR spectrum of **4** in $CDCl_3$.

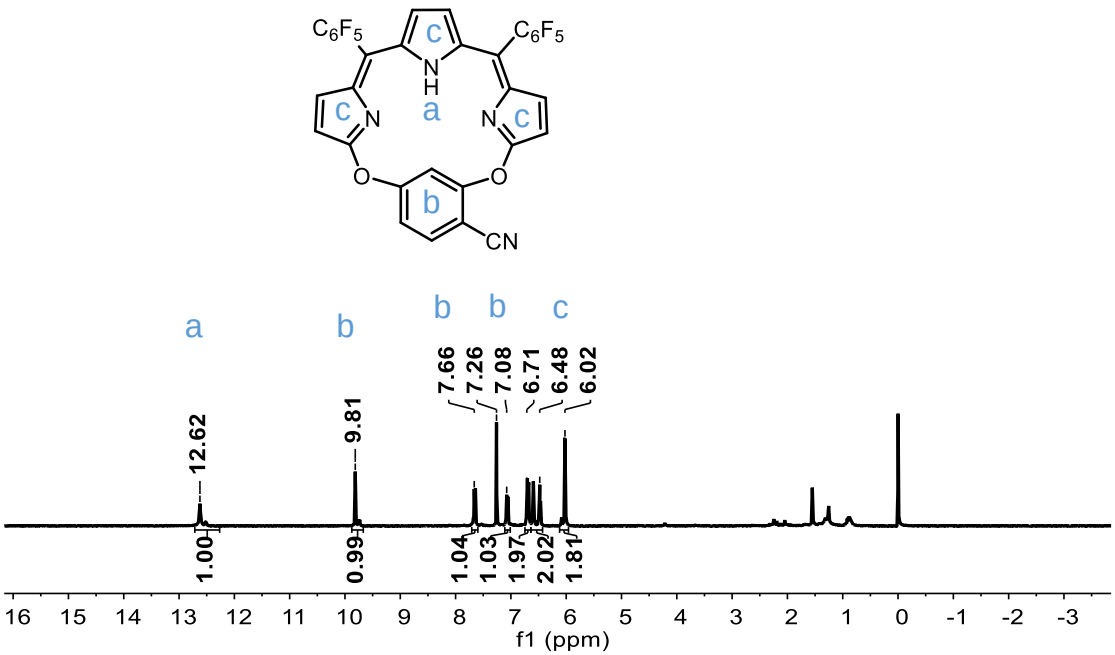

Figure S5. ^{1}H-NMR spectrum of **5** in $CDCl_3$.

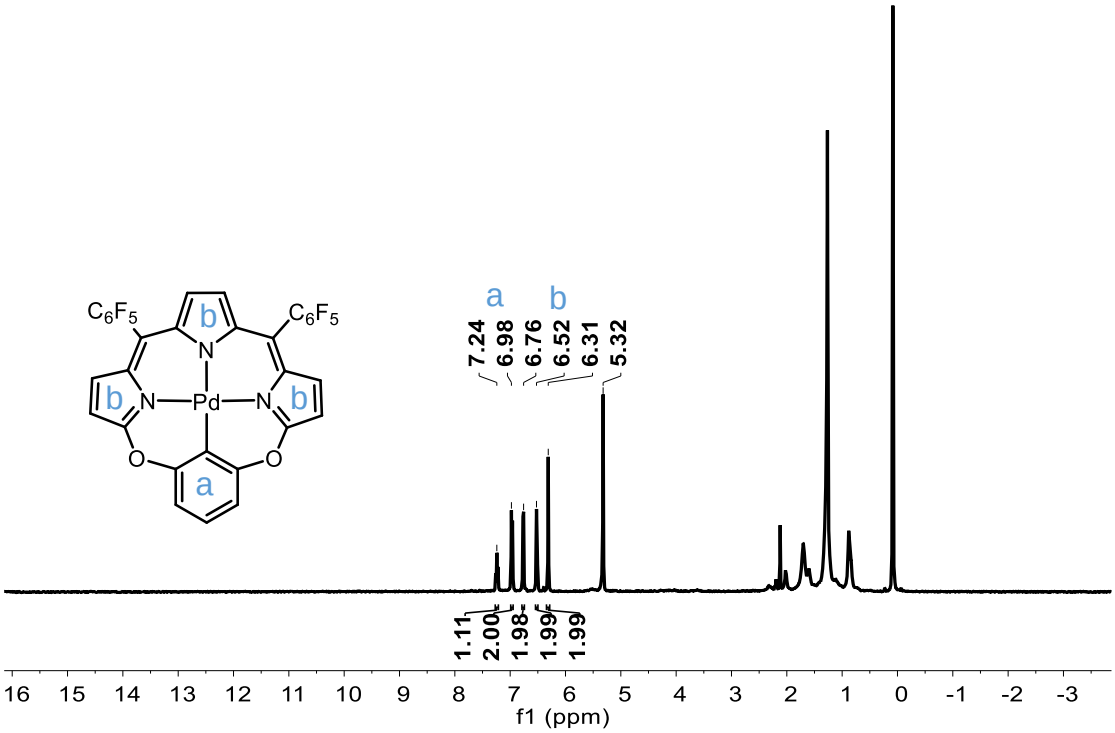

Figure S6. ^{1}H-NMR spectrum of **Pd-1** in CD_2Cl_2.

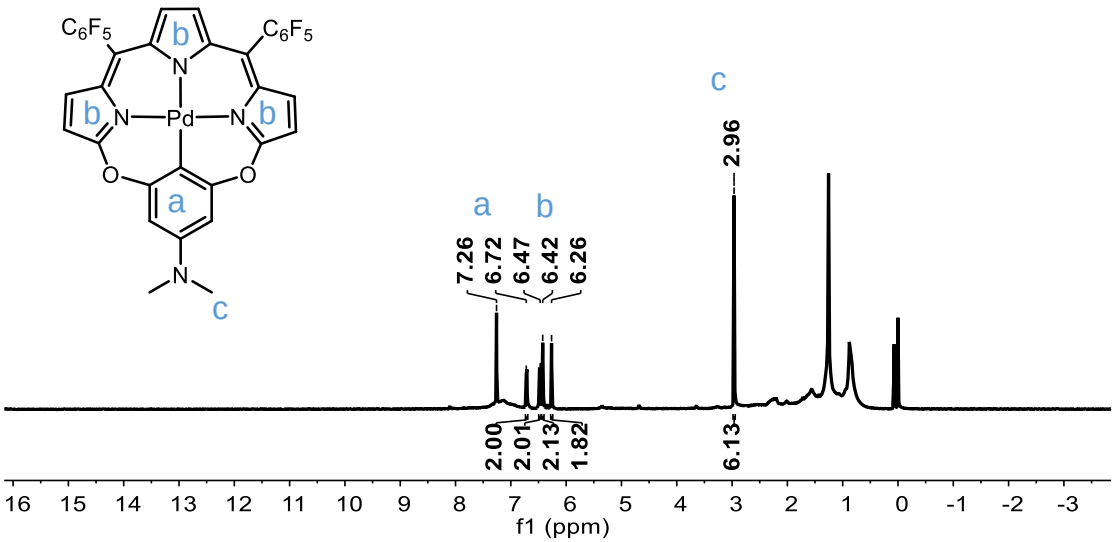

Figure S7. ^{1}H-NMR spectrum of **Pd-2** in $CDCl_3$.

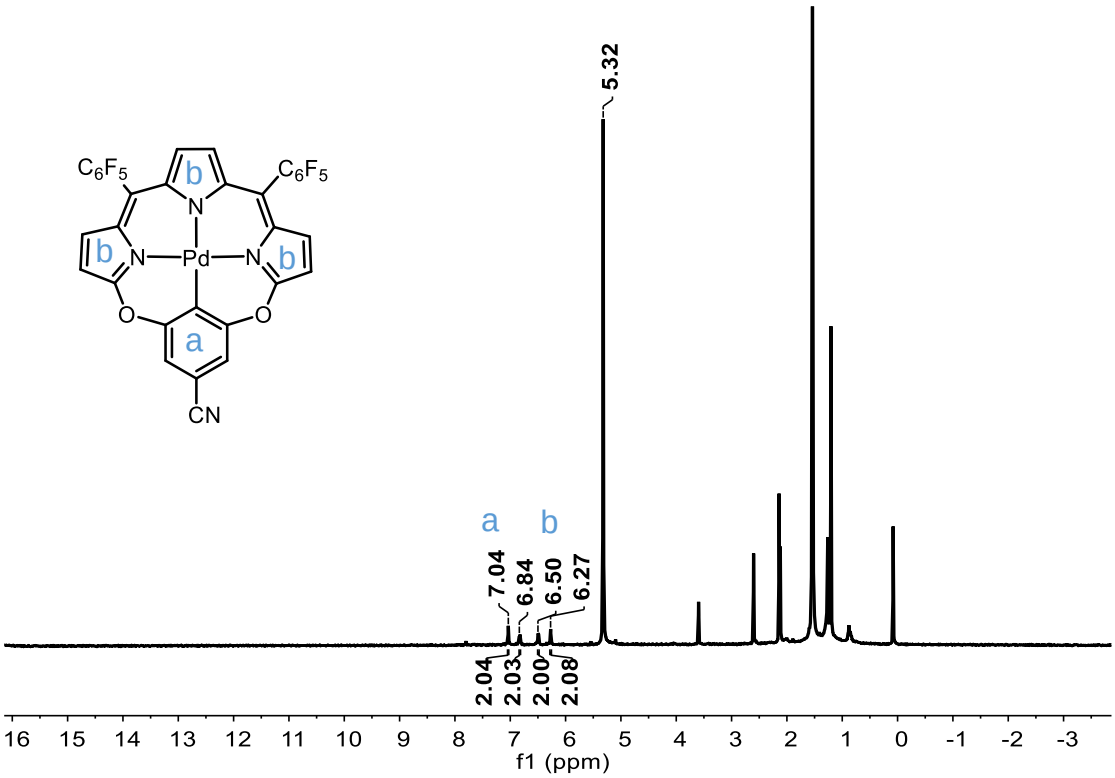

Figure S8. ^{1}H-NMR spectrum of **Pd-3** in CD_2Cl_2.

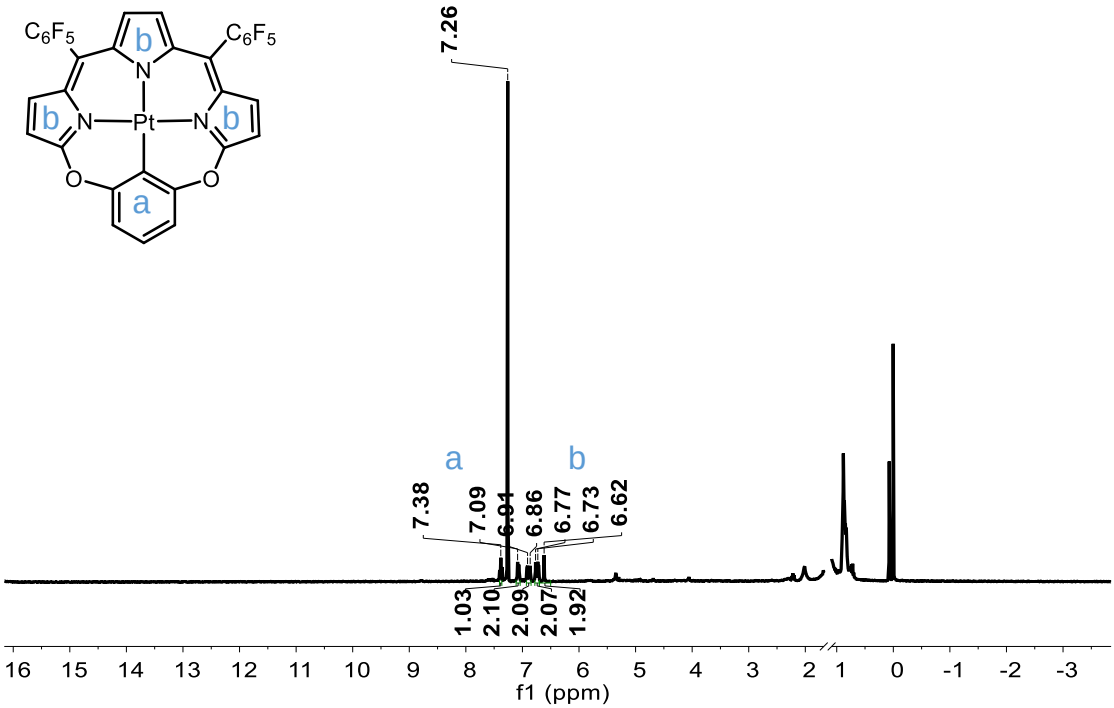

Figure S9. ^{1}H-NMR spectrum of **Pt-1** in $CDCl_3$.

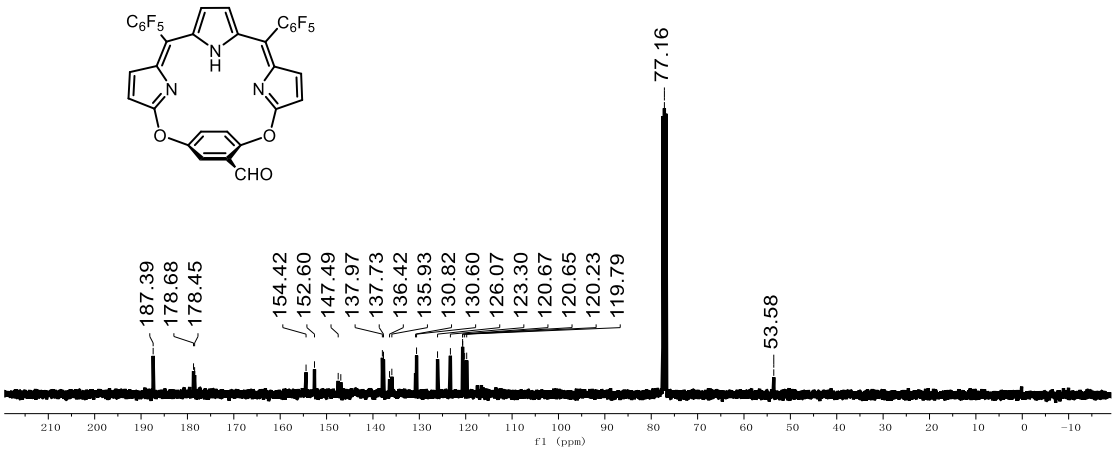

Figure S10. ^{13}C-NMR spectrum of **1** in $CDCl_3$.

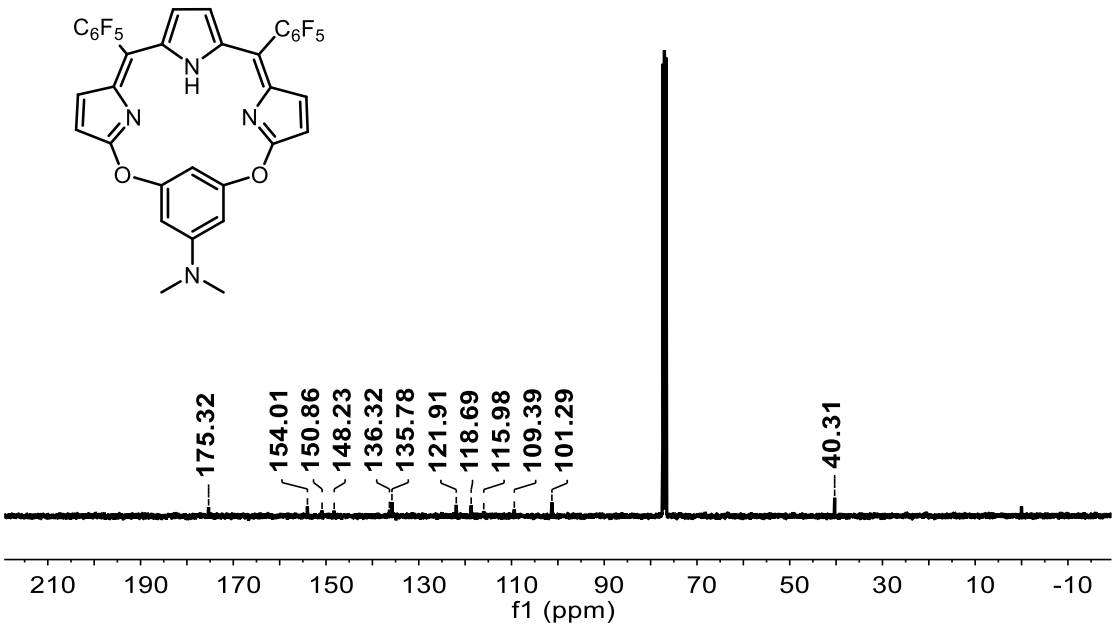

Figure S11. ^{13}C-NMR spectrum of **2** in $CDCl_3$.

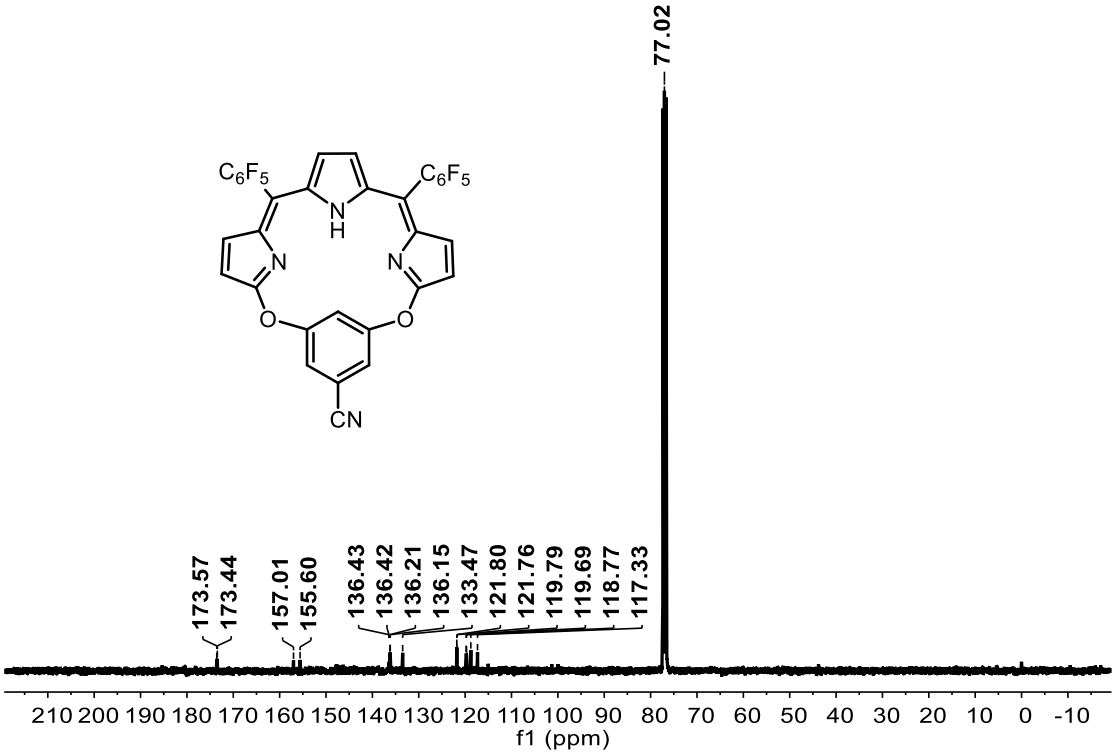

Figure S12. ^{13}C-NMR spectrum of **3** in $CDCl_3$.

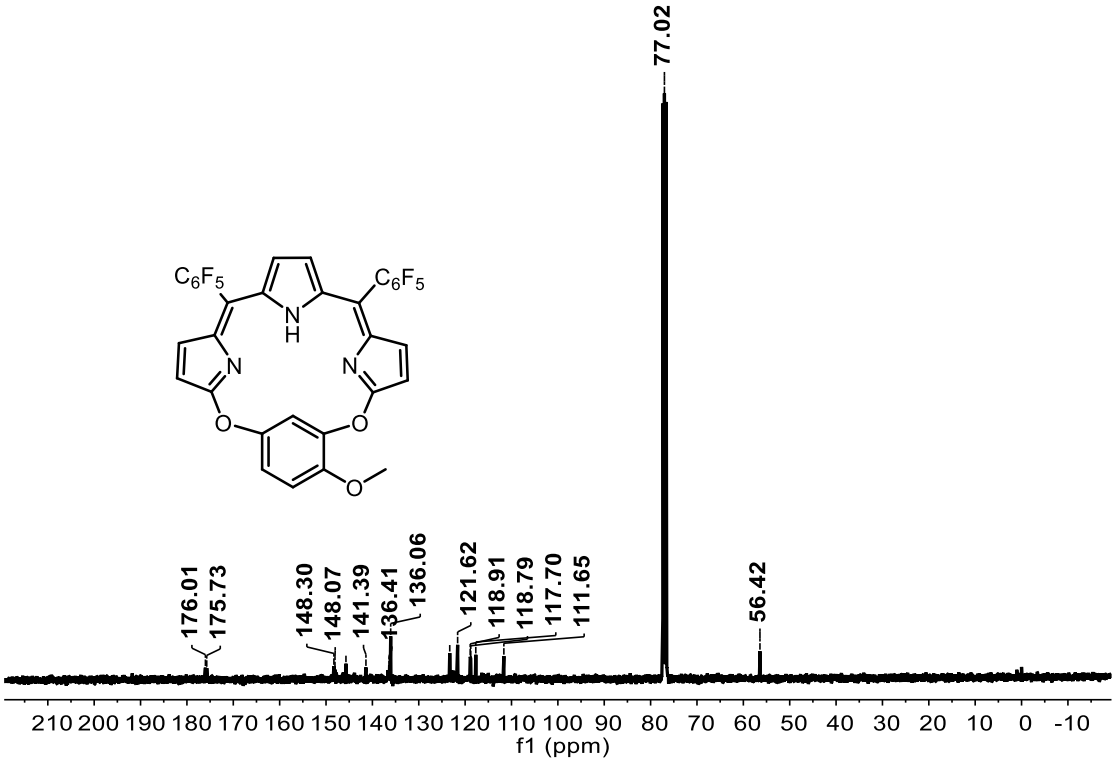

Figure S13. ^{13}C-NMR spectrum of **4** in $CDCl_3$.

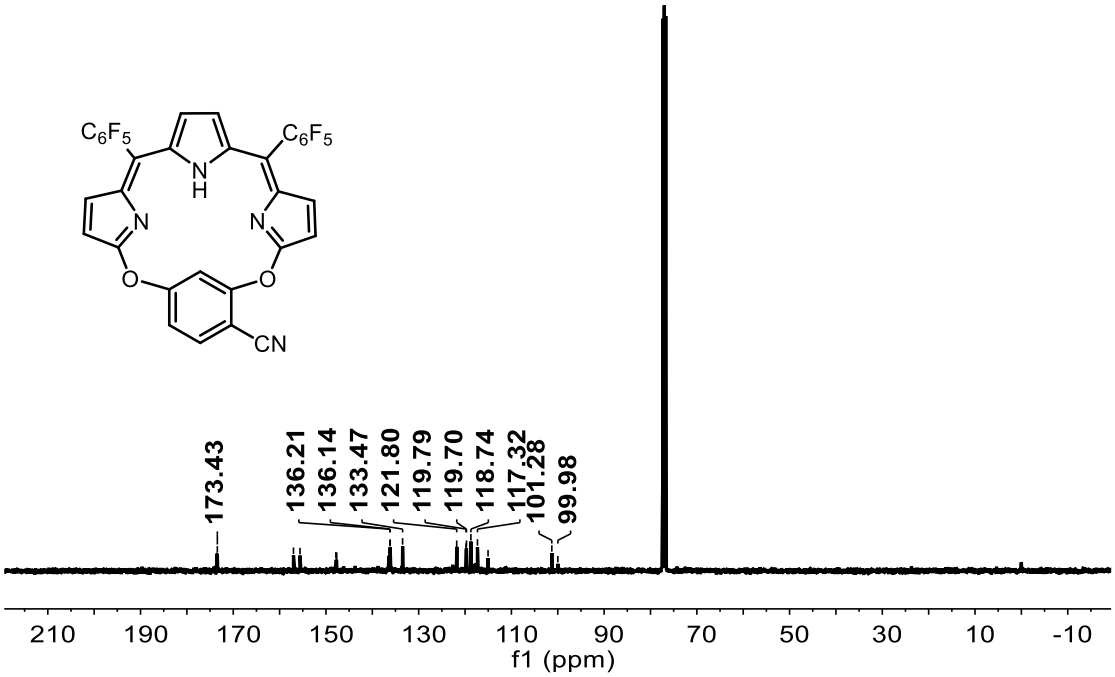

Figure S14. ^{13}C-NMR spectrum of **5** in $CDCl_3$.

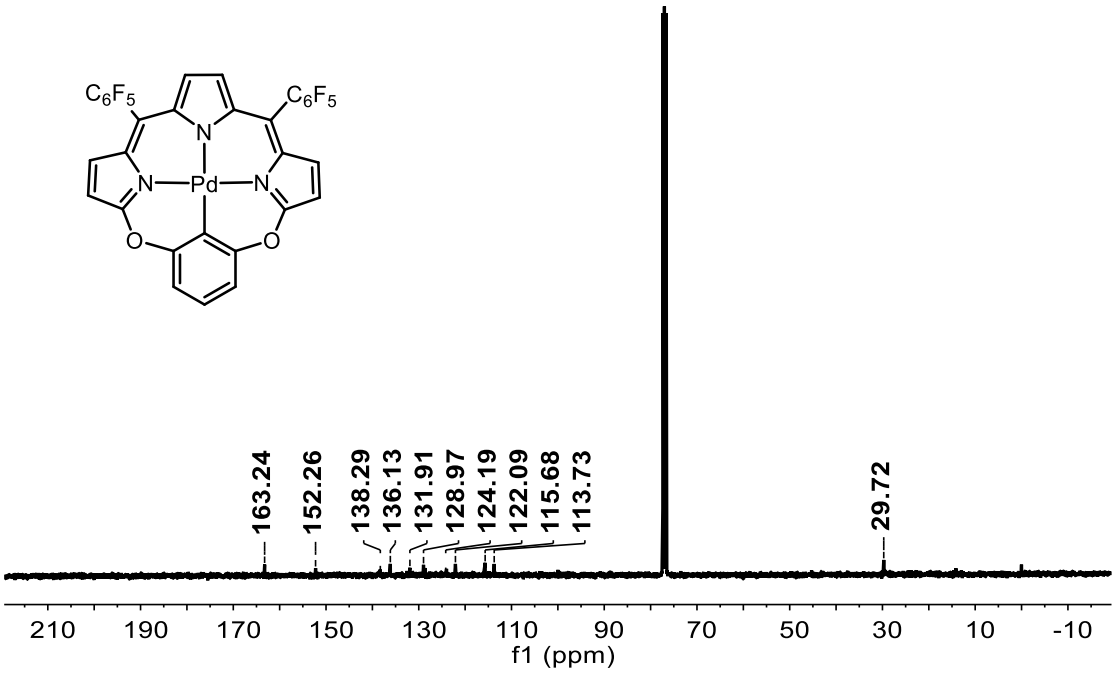

Figure S15. ^{13}C-NMR spectrum of **Pd-1** in CD_2Cl_2.

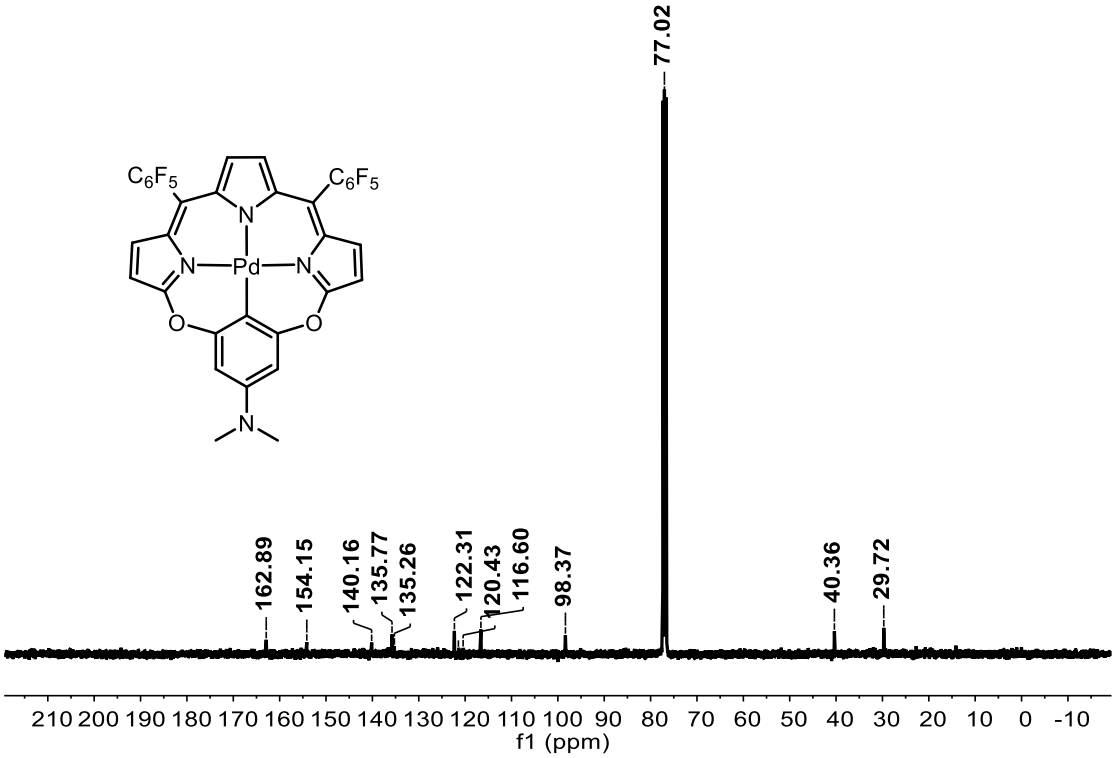

Figure S16. ^{13}C-NMR spectrum of **Pd-2** in $CDCl_3$.

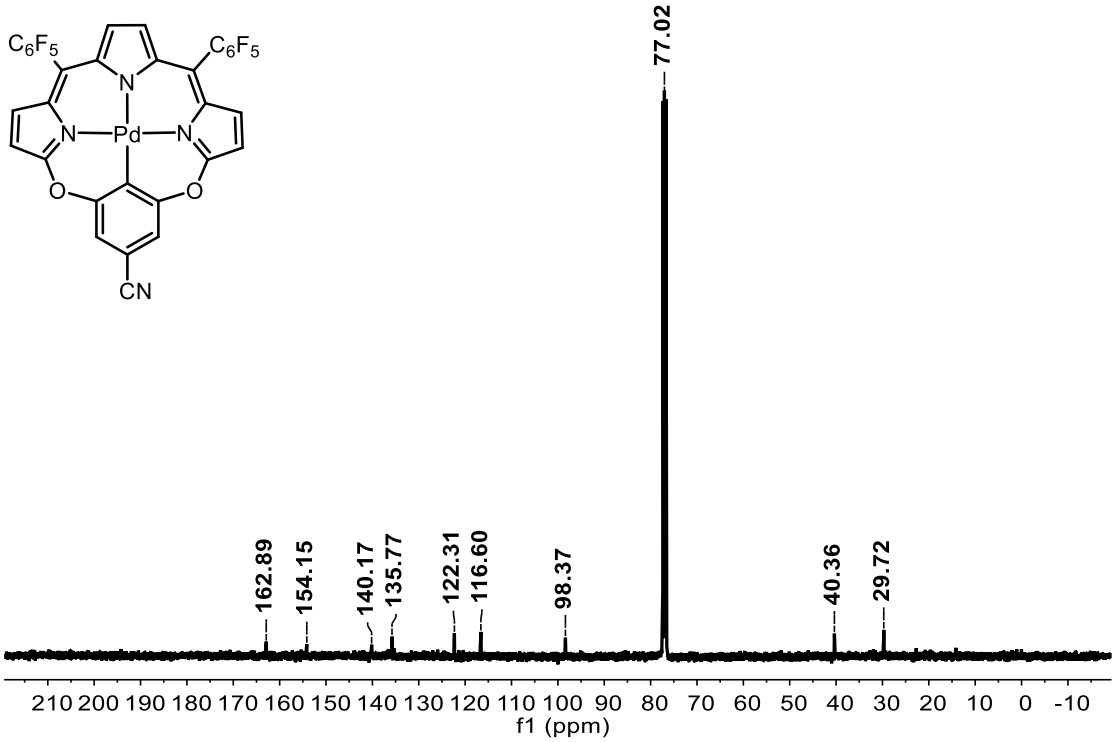

Figure S17. ^{13}C-NMR spectrum of **Pd-3** in CD_2Cl_2.

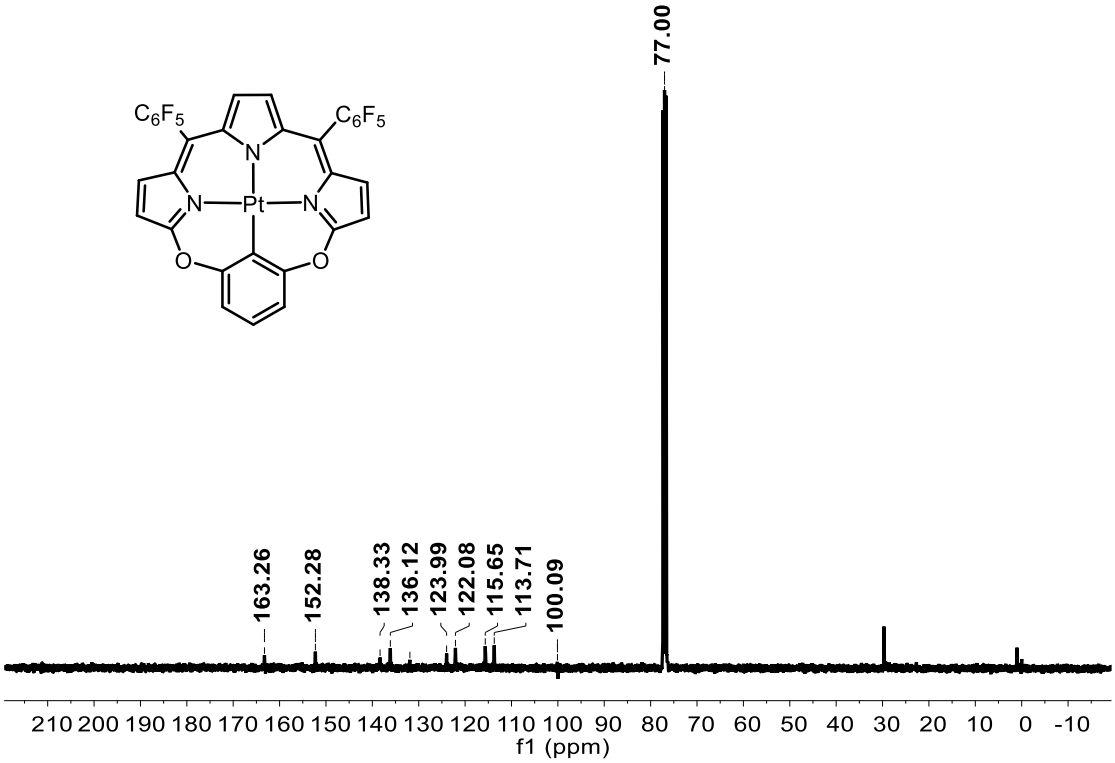

Figure S18. ^{13}C-NMR spectrum of **Pt-1** in $CDCl_3$.

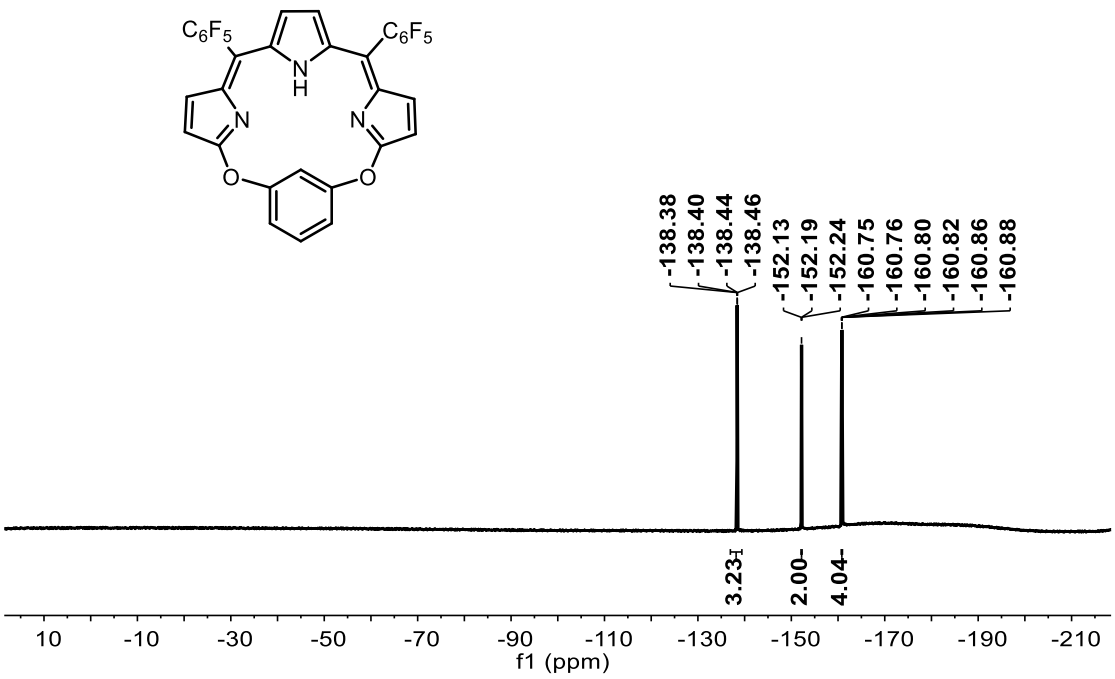

Figure S19. ^{19}F-NMR spectrum of **1** in $CDCl_3$.

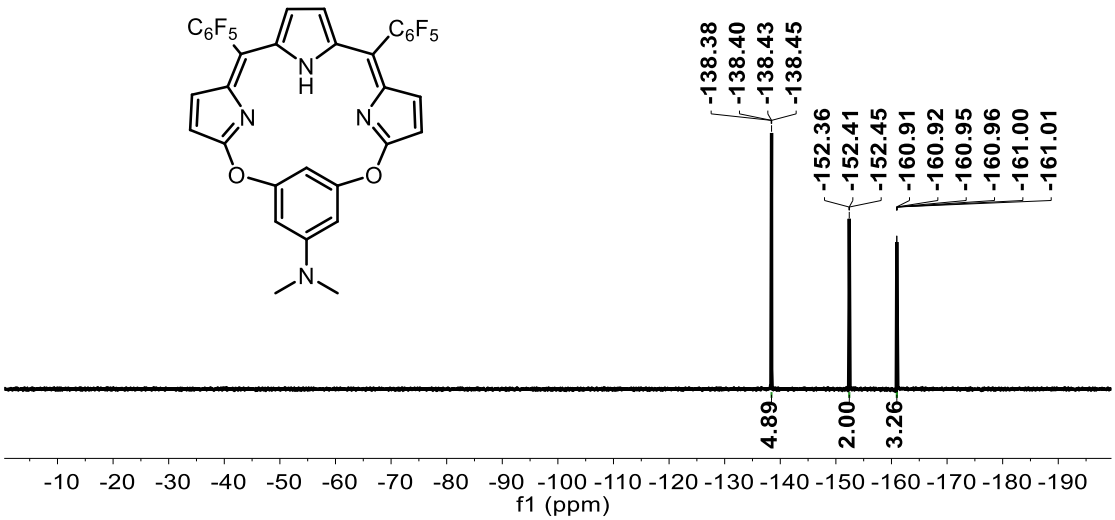

Figure S20. ^{19}F-NMR spectrum of **2** in $CDCl_3$.

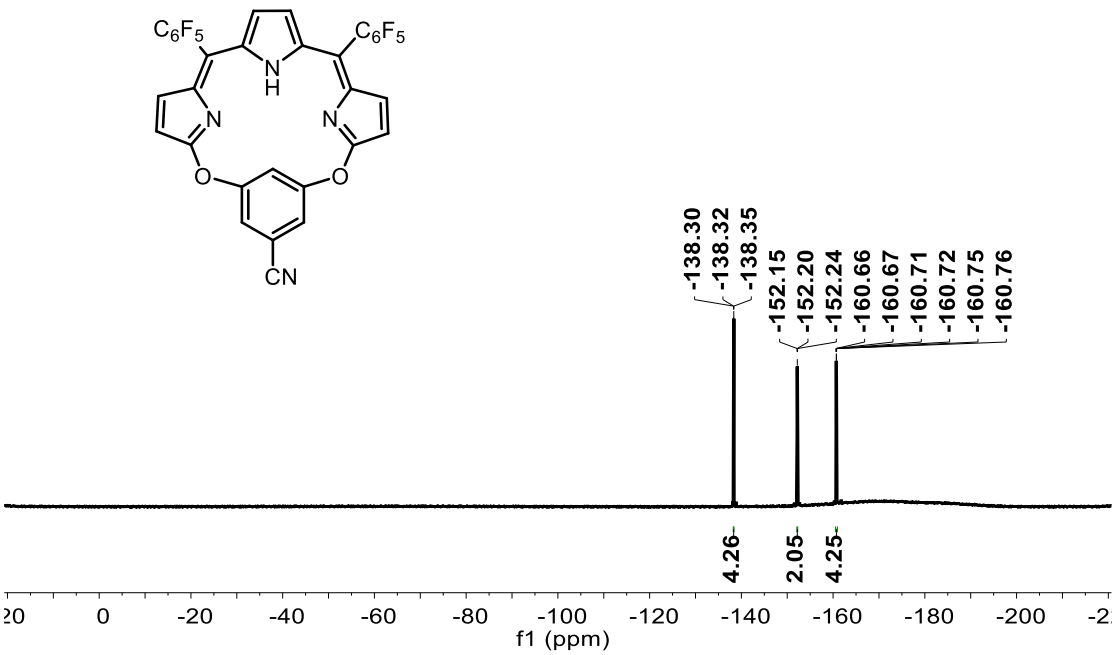

Figure S21. ^{19}F-NMR spectrum of **3** in $CDCl_3$.

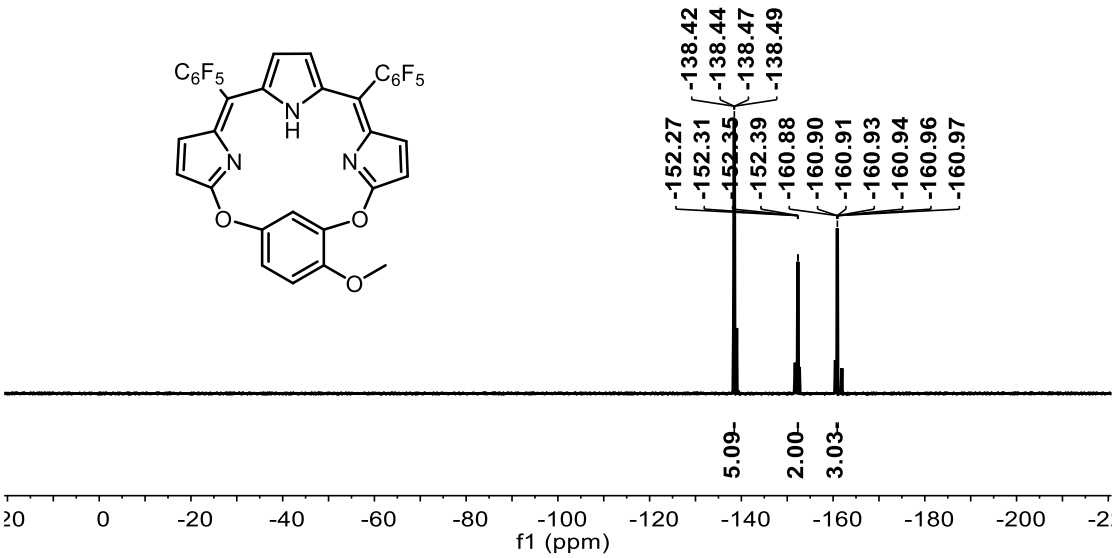

Figure S22. ^{19}F-NMR spectrum of **4** in $CDCl_3$.

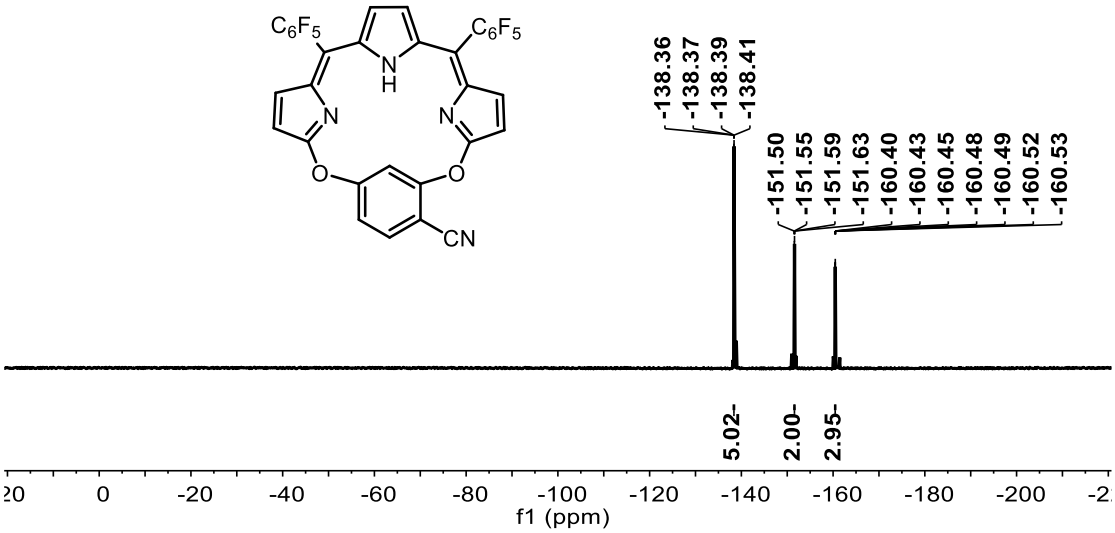

Figure S23. ^{19}F-NMR spectrum of **5** in $CDCl_3$.

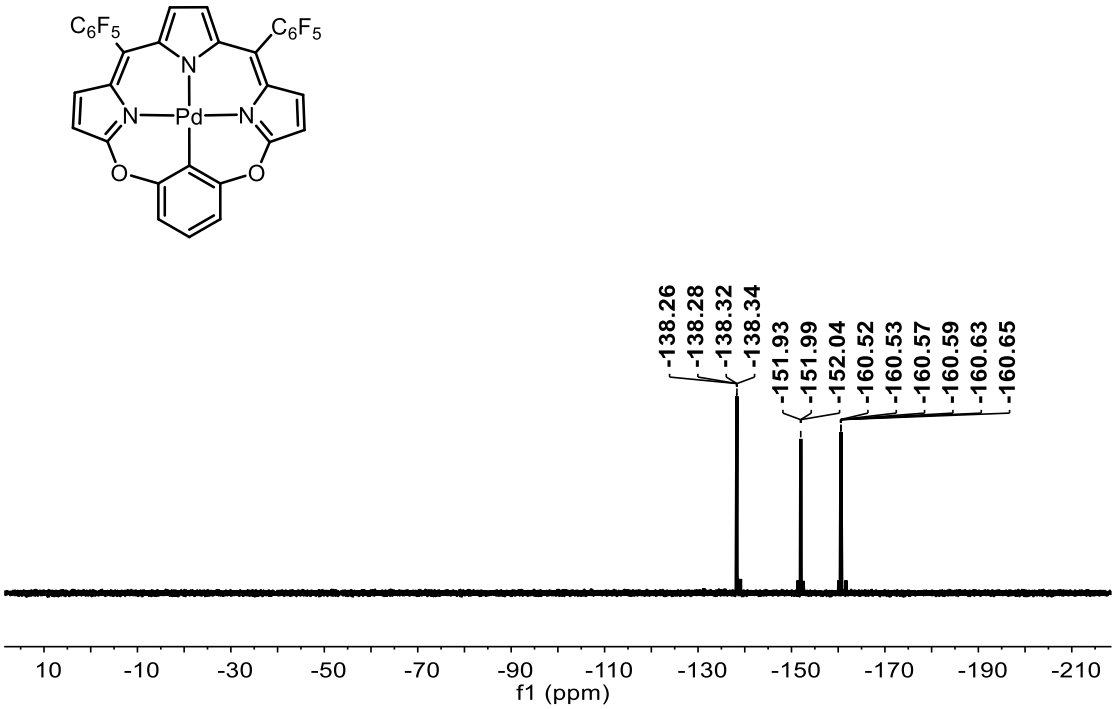

Figure S24. ^{19}F-NMR spectrum of **Pd-1** in CD_2Cl_2.

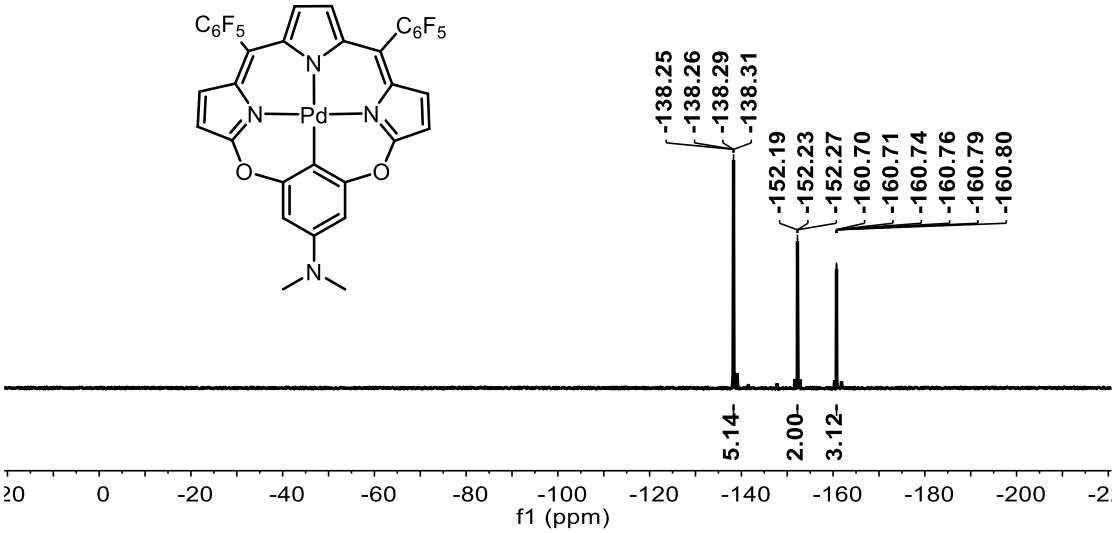

Figure S25. ^{19}F-NMR spectrum of **Pd-2** in $CDCl_3$.

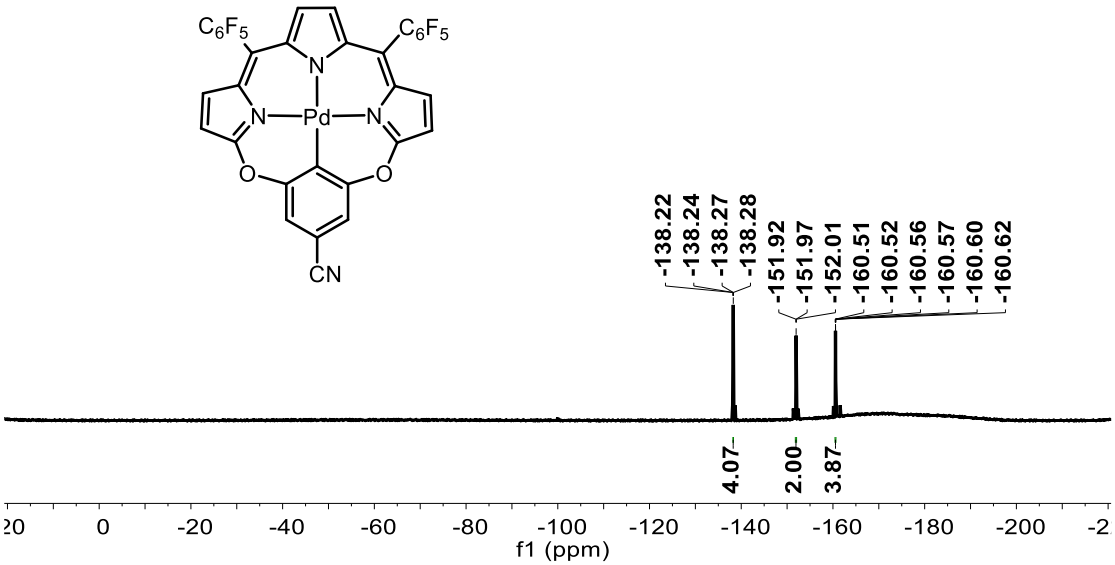

Figure S26. ^{19}F-NMR spectrum of **Pd-3** in CD_2Cl_2.

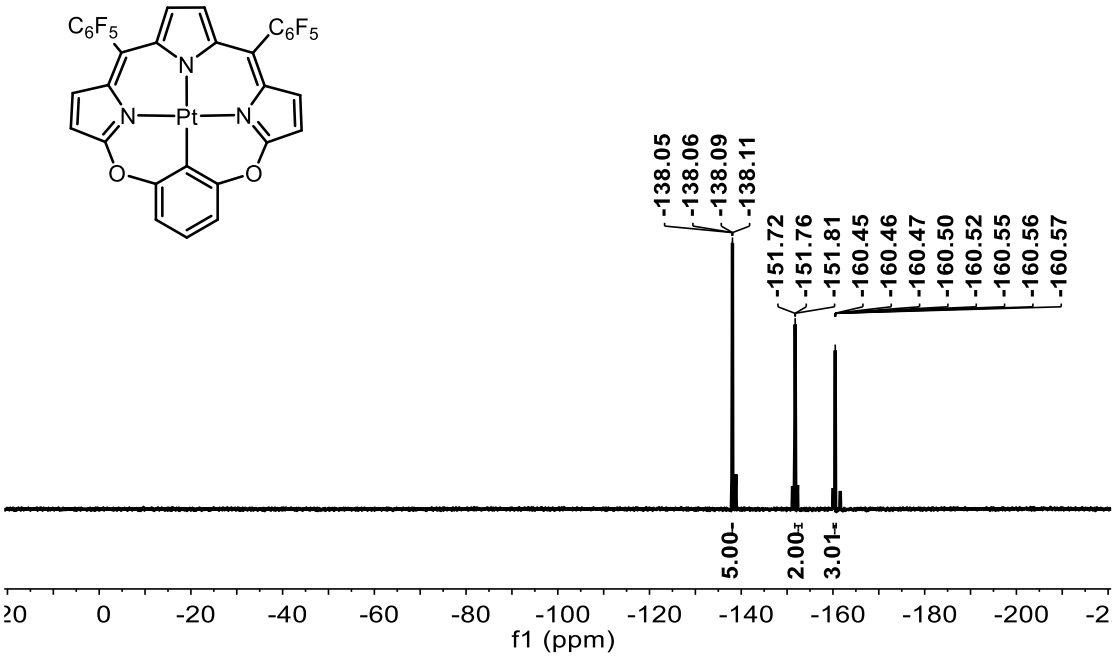

Figure S27. ^{19}F-NMR spectrum of **Pt-1** in $CDCl_3$.

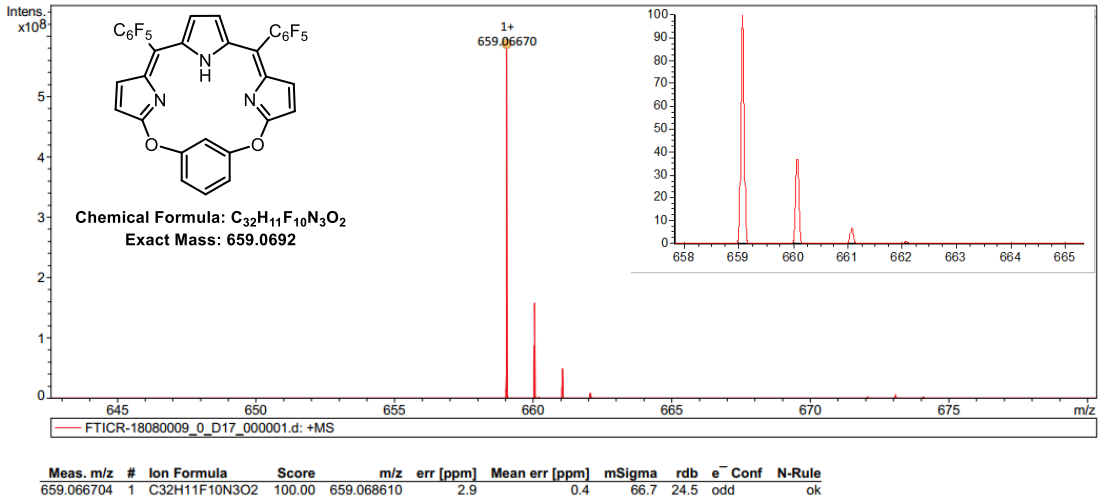

Figure S28. HR-MS (MALDI-TOF) of **1**, inset shows the isotopic pattern of the signal 659.0692 (m/z = 659.0667).

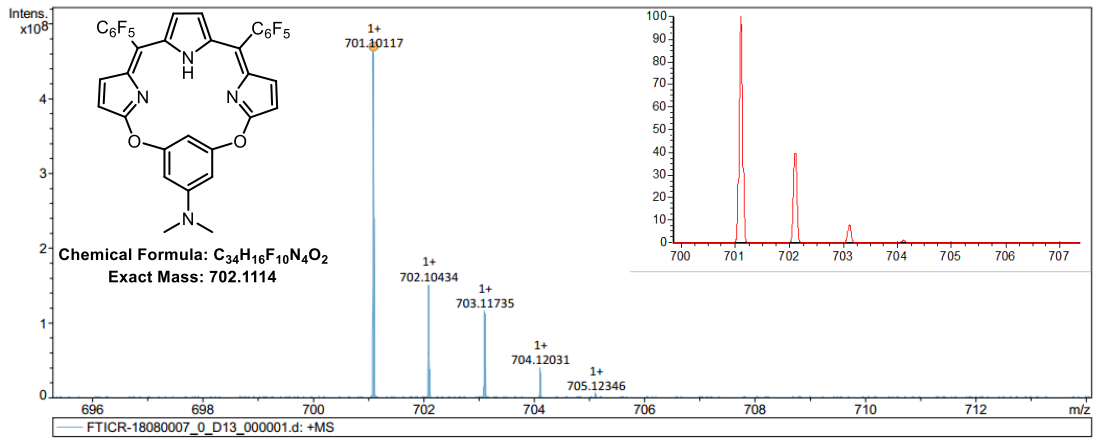

Meas. m/z	#	Ion Formula	Score	m/z	err [ppm]	Mean err [ppm]	mSigma	rdb	e⁻ Conf	N-Rule
701.101175	1	C34H15F10N4O2	100.00	701.102984	2.6	1.7	48.0	25.0	even	ok

Figure S29. HR-MS (MALDI-TOF) of **2,** inset shows the isotopic pattern of the signal 702.1114 (m/z = 702.1043).

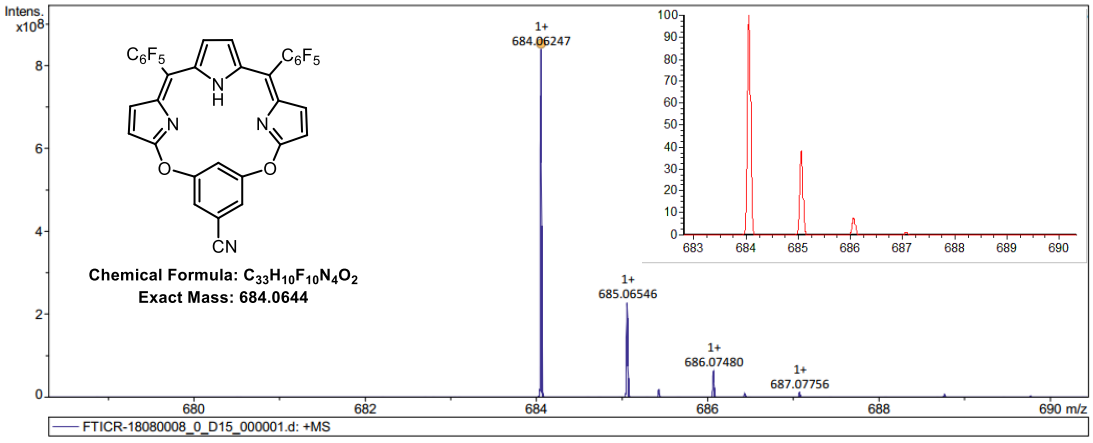

Meas. m/z	#	Ion Formula	Score	m/z	err [ppm]	Mean err [ppm]	mSigma	rdb	e⁻ Conf	N-Rule
684.062473	1	C33H10F10N4O2	100.00	684.063859	2.0	-0.9	50.4	26.5	odd	ok

Figure S30. HR-MS (MALDI-TOF) of **3**, inset shows the isotopic pattern of the signal 684.0644 (m/z = 684.0625).

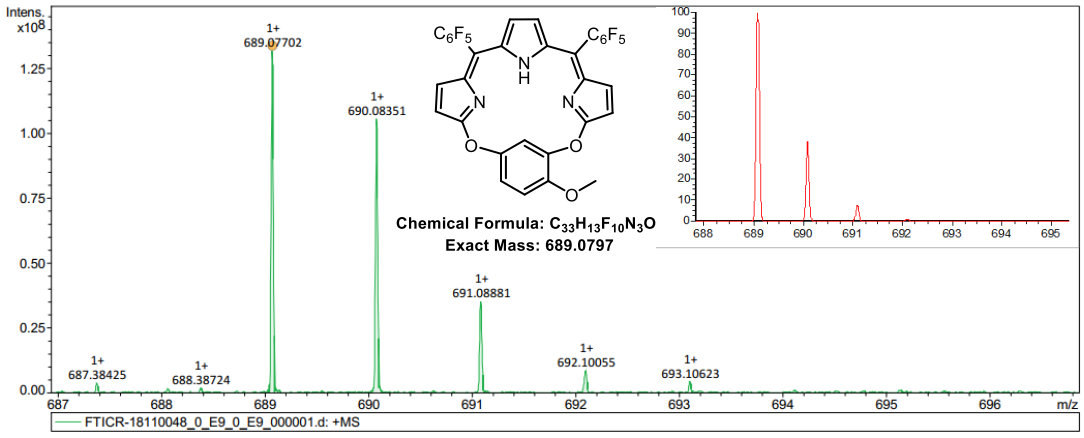

Meas. m/z	#	Ion Formula	Score	m/z	err [ppm]	Mean err [ppm]	mSigma	rdb	e⁻ Conf	N-Rule
689.077024	1	C33H13F10N3O3	100.00	689.079174	3.1	0.1	237.2	24.5	odd	ok

Figure S31. HR-MS (MALDI-TOF) of **4**, inset shows the isotopic pattern of the signal 689.0797 (m/z = 689.0770).

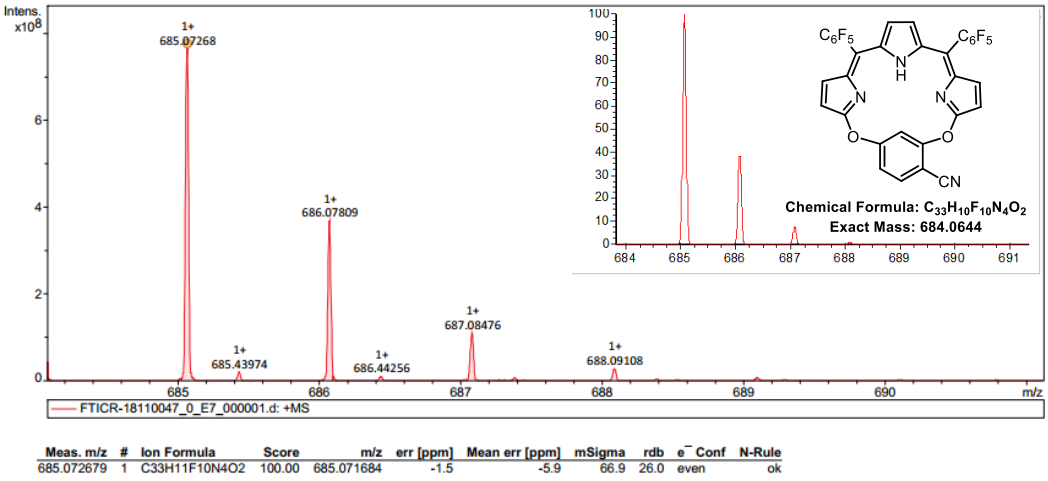

Meas. m/z	#	Ion Formula	Score	m/z	err [ppm]	Mean err [ppm]	mSigma	rdb	e⁻ Conf	N-Rule
685.072679	1	C33H11F10N4O2	100.00	685.071684	-1.5	-5.9	66.9	26.0	even	ok

Figure S32. HR-MS (MALDI-TOF) of **5**, inset shows the isotopic pattern of the signal 684.0644 (m/z = 685.0727).

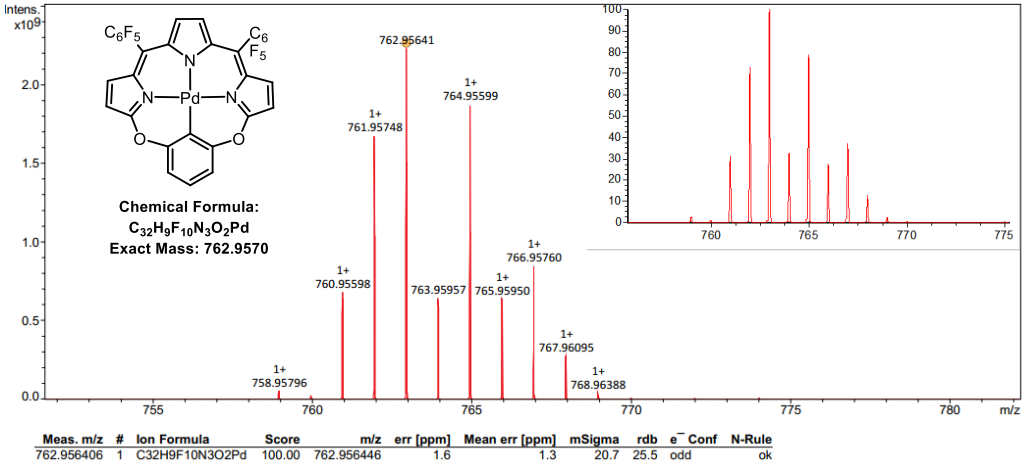

Meas. m/z	#	Ion Formula	Score	m/z	err [ppm]	Mean err [ppm]	mSigma	rdb	e⁻ Conf	N-Rule
762.956406	1	C32H9F10N3O2Pd	100.00	762.956446	1.6	1.3	20.7	25.5	odd	ok

Figure S33. HR-MS (MALDI-TOF) of **Pd-1**, inset shows the isotopic pattern of the signal 762.9670 (m/z = 762.9564).

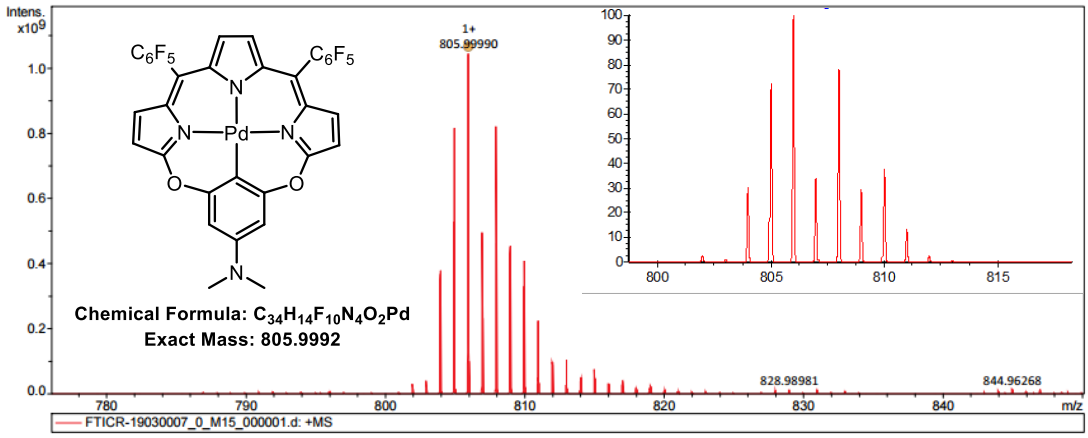

Meas. m/z	#	Ion Formula	Score	m/z	err [ppm]	Mean err [ppm]	mSigma	rdb	e⁻ Conf	N-Rule
805.999898	1	C34H14F10N4O2Pd	100.00	805.998639	0.0	-0.5	77.6	26.5	odd	ok

Figure S34. HR-MS (MALDI-TOF) of **Pd-2**, inset shows the isotopic pattern of the signal 805.9992 (m/z = 805.9999).

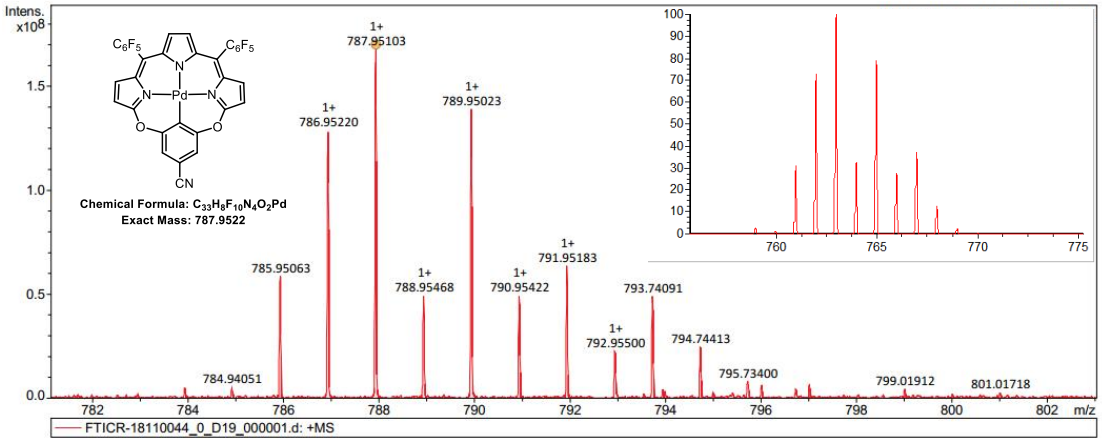

Meas. m/z	#	Ion Formula	Score	m/z	err [ppm]	Mean err [ppm]	mSigma	rdb	e⁻ Conf	N-Rule
787.951028	1	C33H8F10N4O2Pd	100.00	787.951689	2.4	2.0	26.5	28.5	odd	ok

Figure S35. HR-MS (MALDI-TOF) of **Pd-3**, inset shows the isotopic pattern of the signal 787.9522 (m/z = 787.9510).

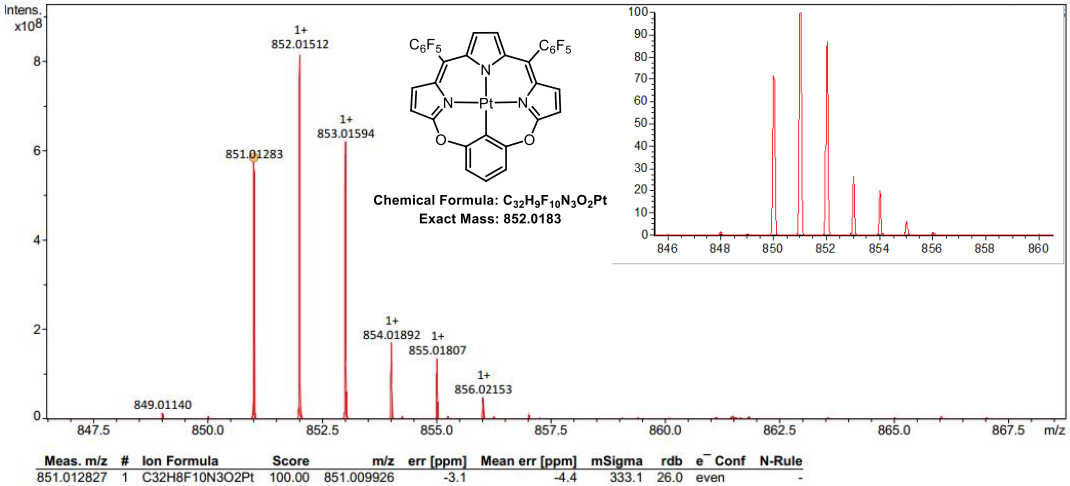

Meas. m/z	#	Ion Formula	Score	m/z	err [ppm]	Mean err [ppm]	mSigma	rdb	e⁻ Conf	N-Rule
851.012827	1	C32H8F10N3O2Pt	100.00	851.009926	-3.1	-4.4	333.1	26.0	even	-

Figure S36. HR-MS (MALDI-TOF) of **Pt-1**, inset shows the isotopic pattern of the signal 852.0183 (m/z = 852.0151).

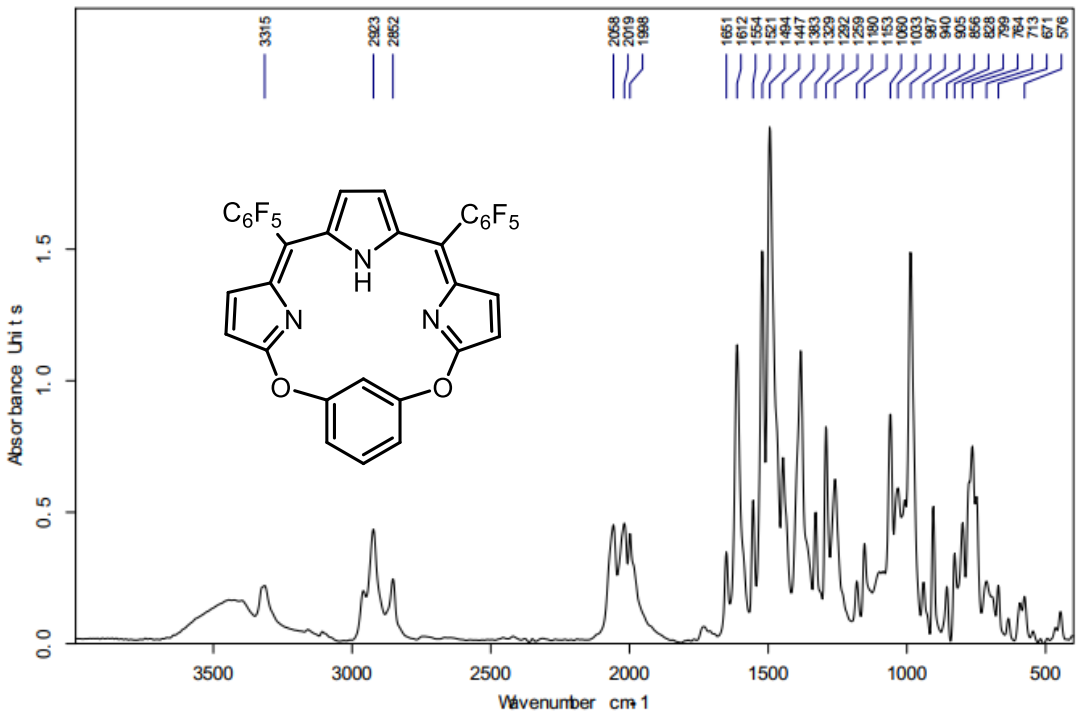

Figure S37. FT-IR spectrum of **1**.

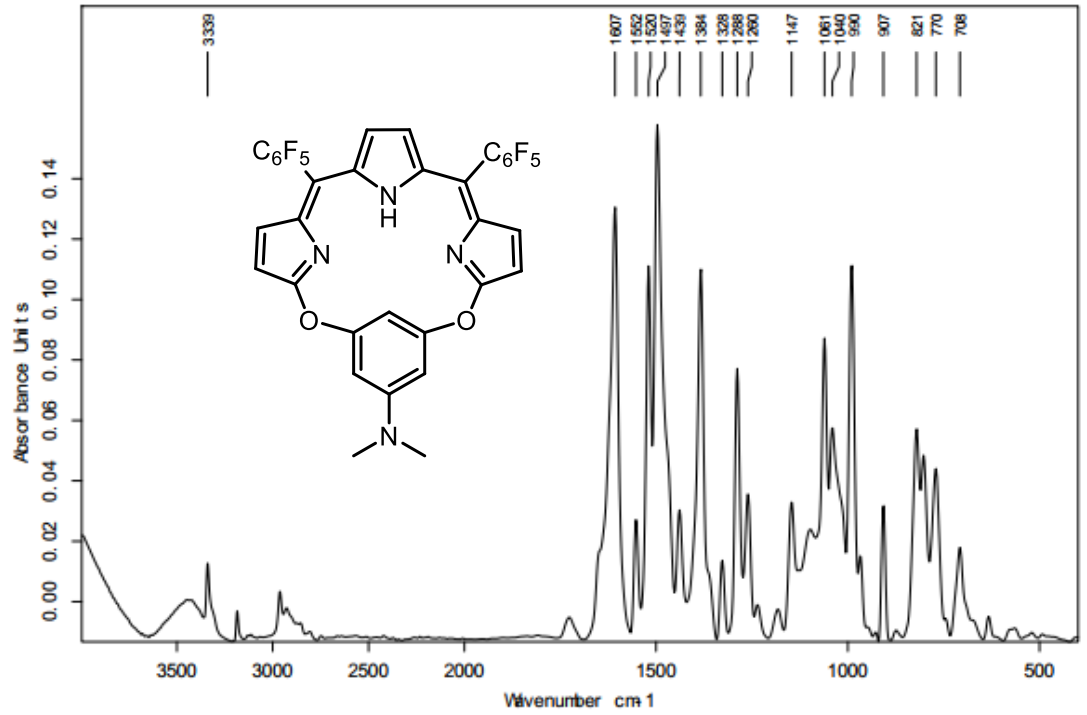

Figure S38. FT-IR spectrum of **2.**

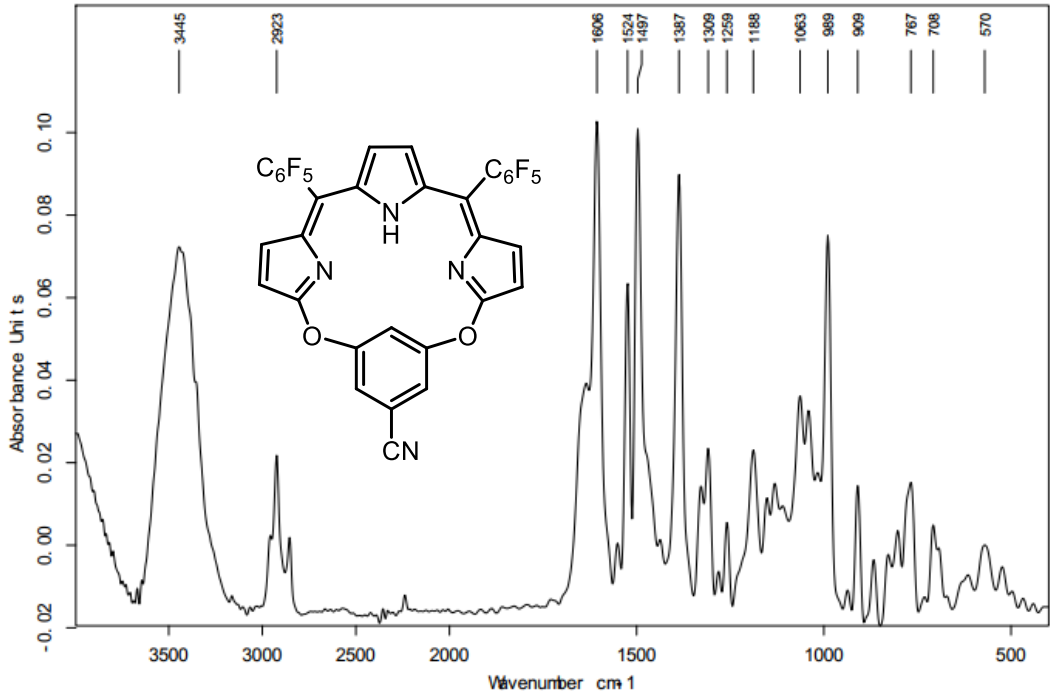

Figure S39. FT-IR spectrum of **3.**

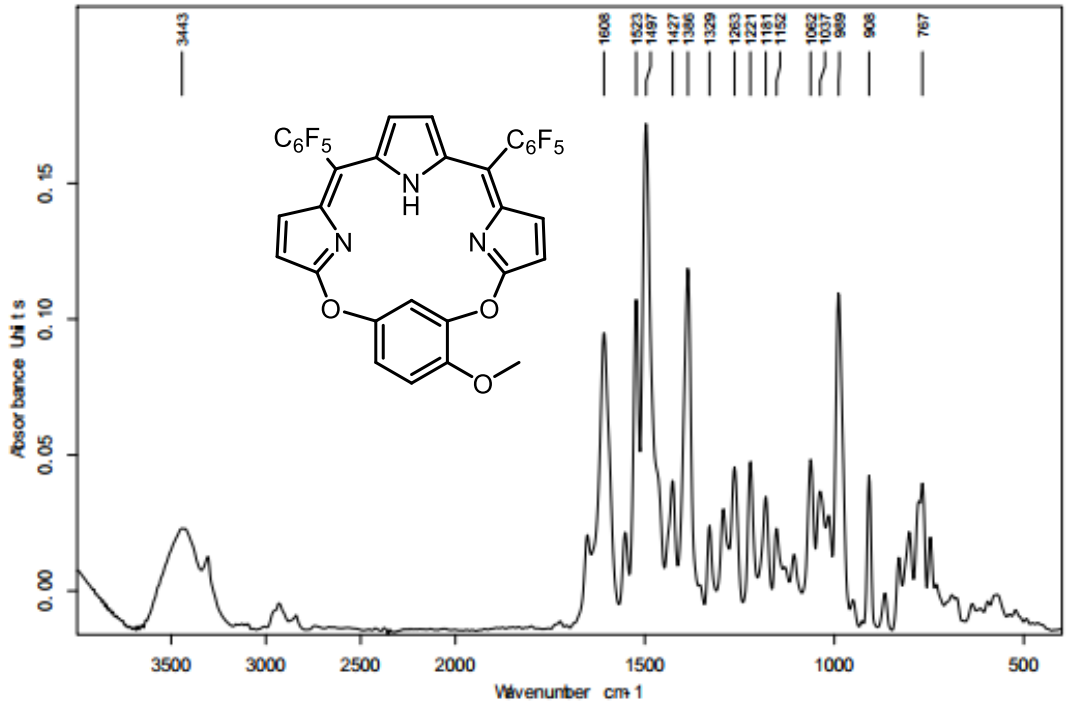

Figure S40. FT-IR spectrum of **4.**

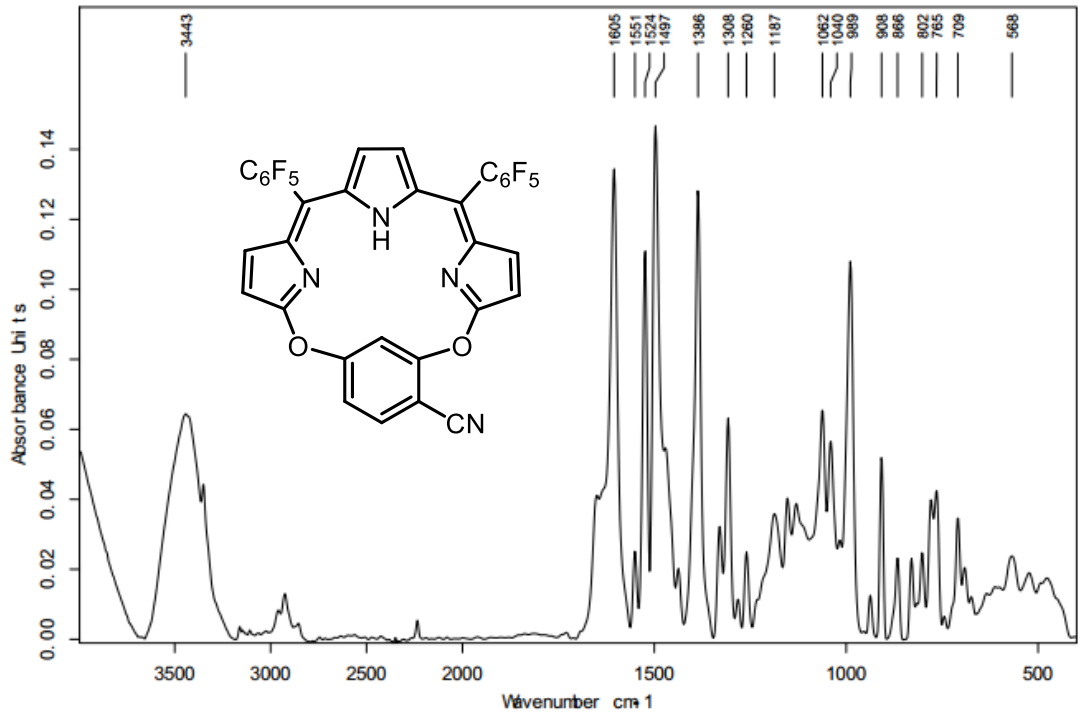

Figure S41. FT-IR spectrum of **5.**

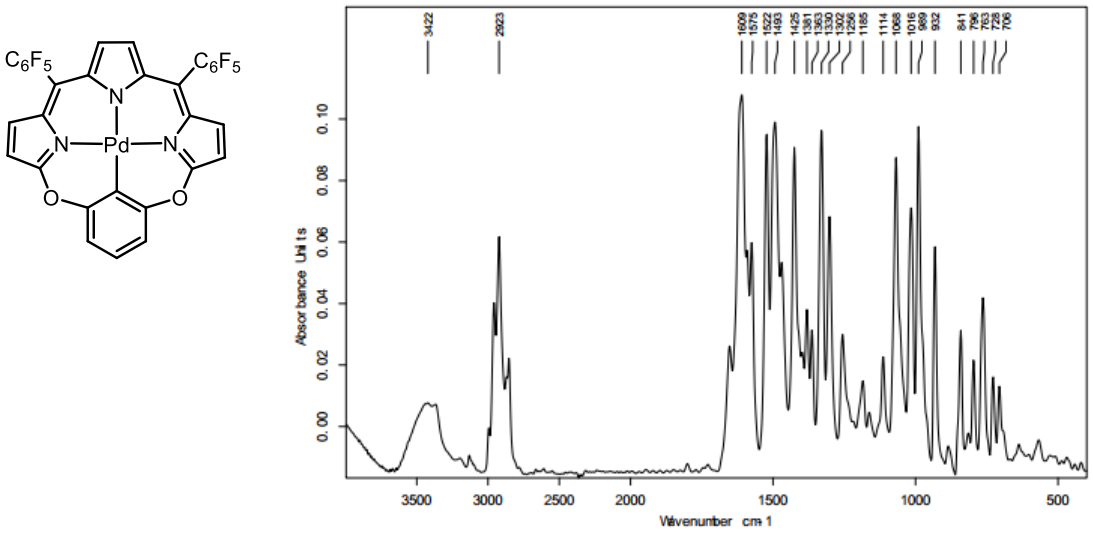

Figure S42. FT-IR spectrum of **Pd-1.**

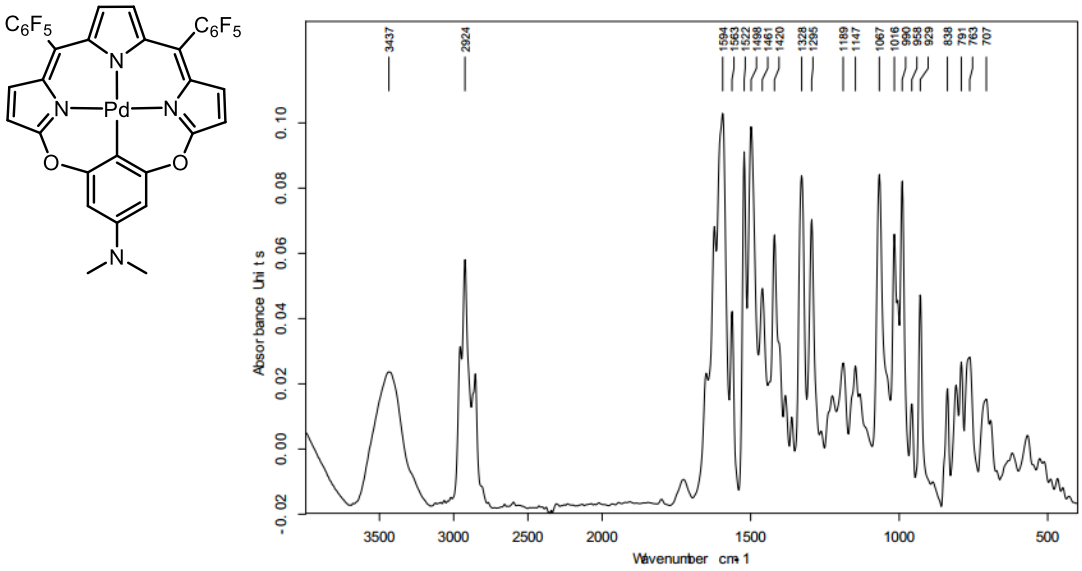

Figure S43. FT-IR spectrum of **Pd-2.**

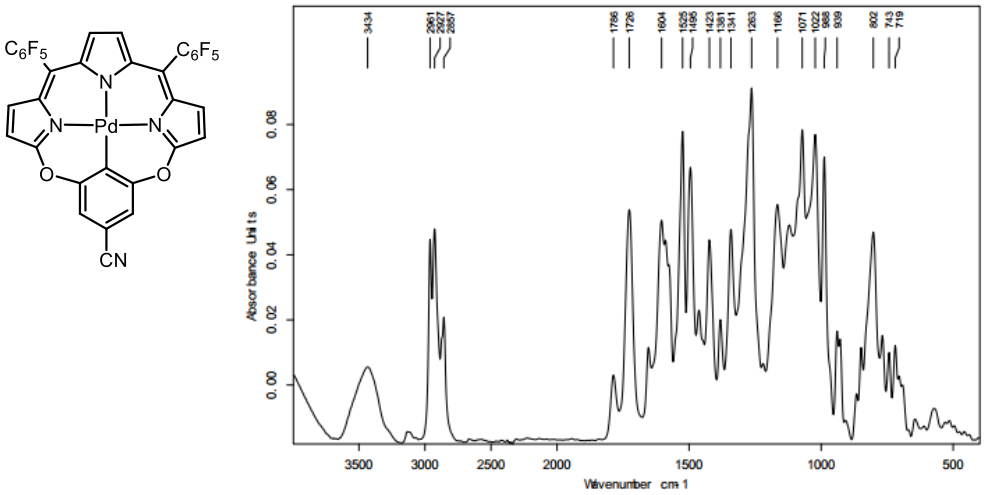

Figure S44. FT-IR spectrum of **Pd-3.**

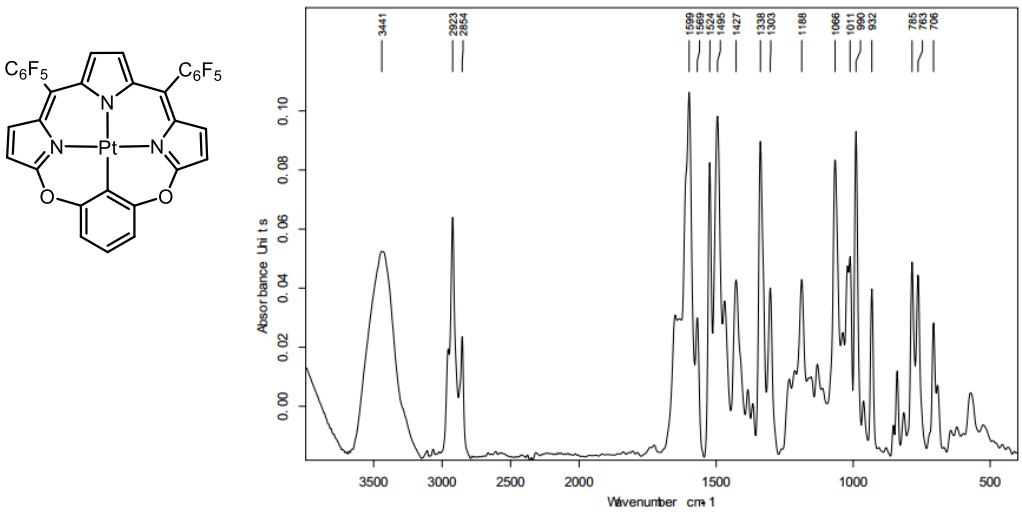

Figure S45. FT-IR spectrum of **Pt-1.**

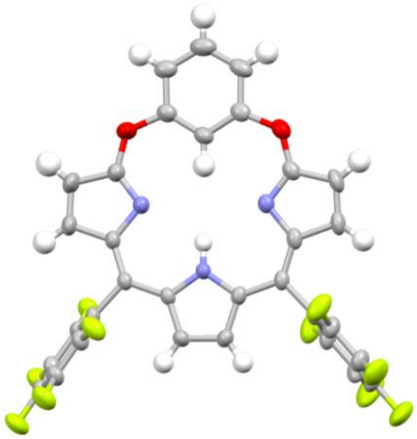

Figure S46. Single crystal structure of **1**. The thermal ellipsoids are scaled to the 50% probability level and solvent molecules are omitted for clarity.

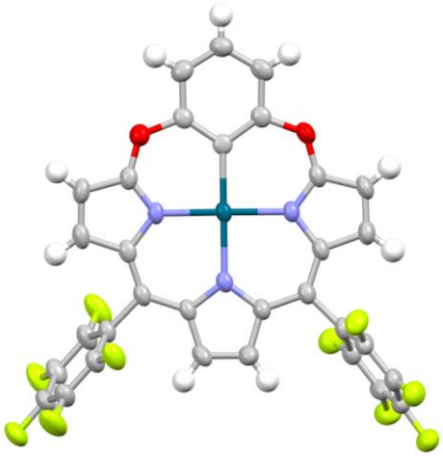

Figure S47. Single crystal structure of **Pd-1**. The thermal ellipsoids are scaled to the 50% probability level and solvent molecules are omitted for clarity.

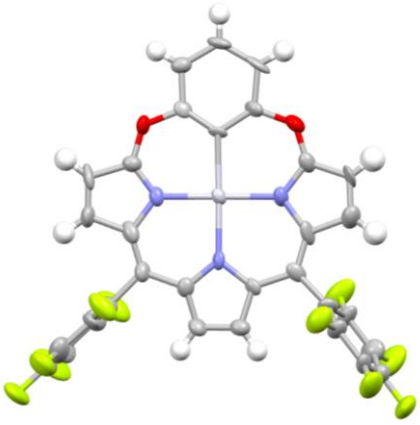

Figure S48. Single crystal structure of **Pt-1**. The thermal ellipsoids are scaled to the 50% probability level and solvent molecules are omitted for clarity.

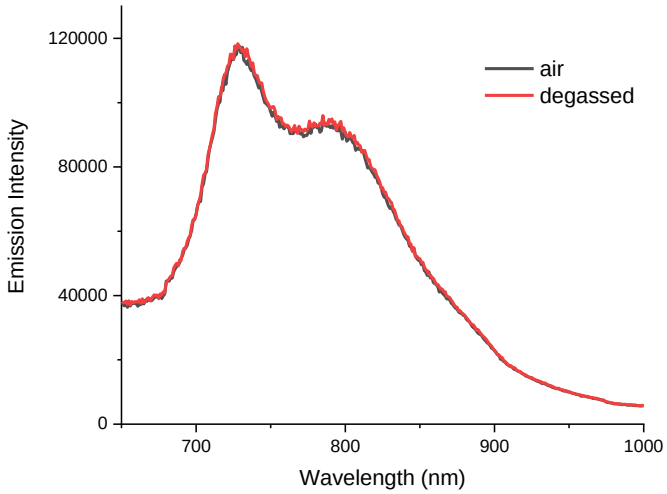

Figure S49. Emission spectra of **Pd-1** excited at 600 nm in degassed and air saturated CH_2Cl_2.

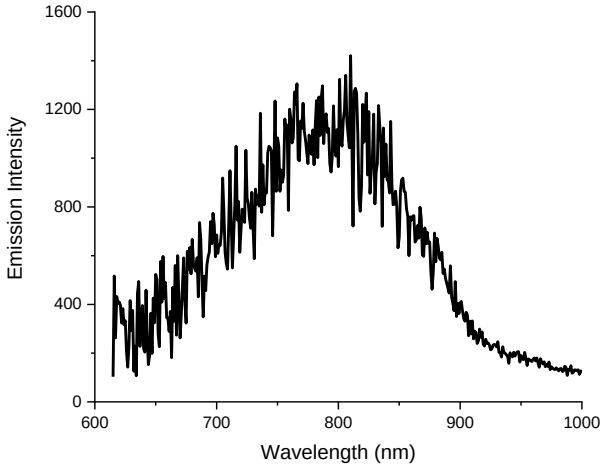

Figure S50. Emission spectra of **Pd-2** excited at 600 nm in CH_2Cl_2.

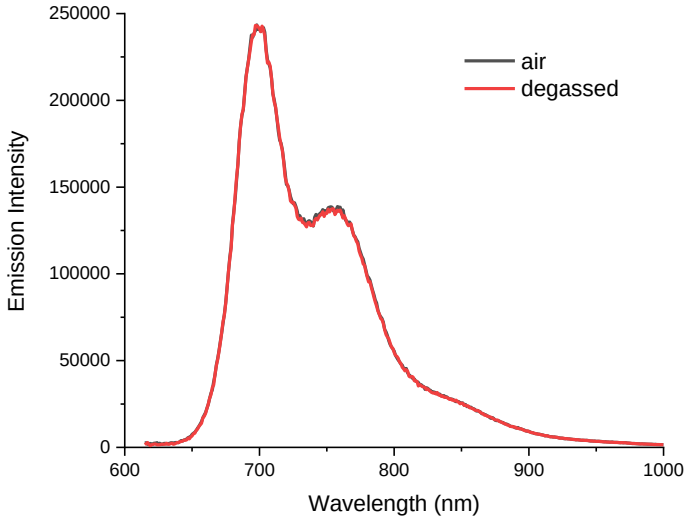

Figure S51. Emission spectra of **Pd-3** excited at 600 nm in degassed and air saturated CH_2Cl_2.

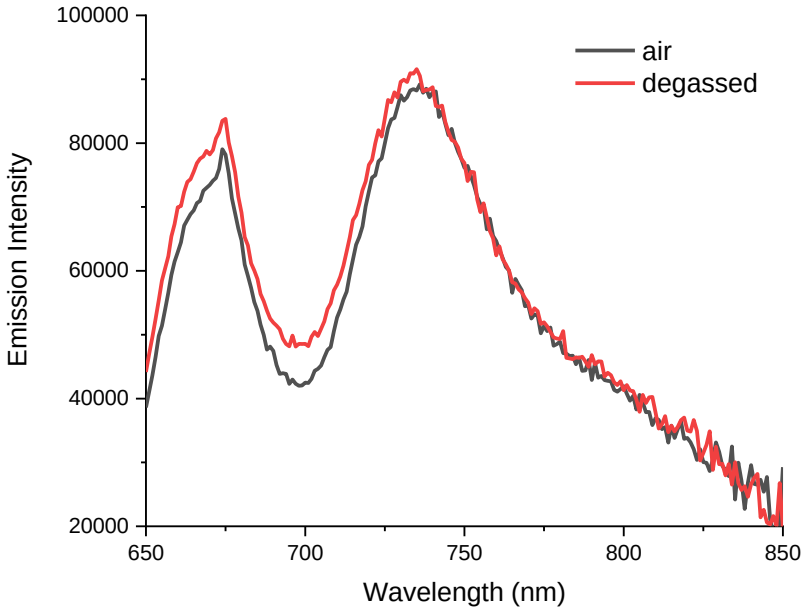

Figure S52. Emission spectra of **Pt-1** excited at 600 nm in degassed and air saturated CH_2Cl_2.

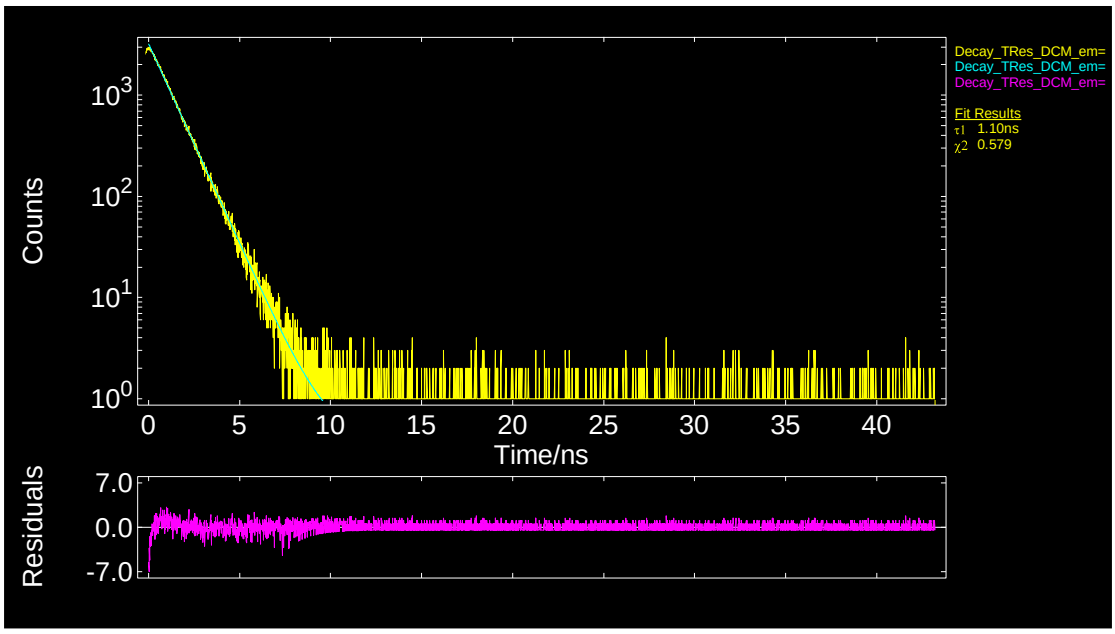

Figure S53. Lifetime decay profile of fluorescence band of **1** at 613 nm in CH_2Cl_2.

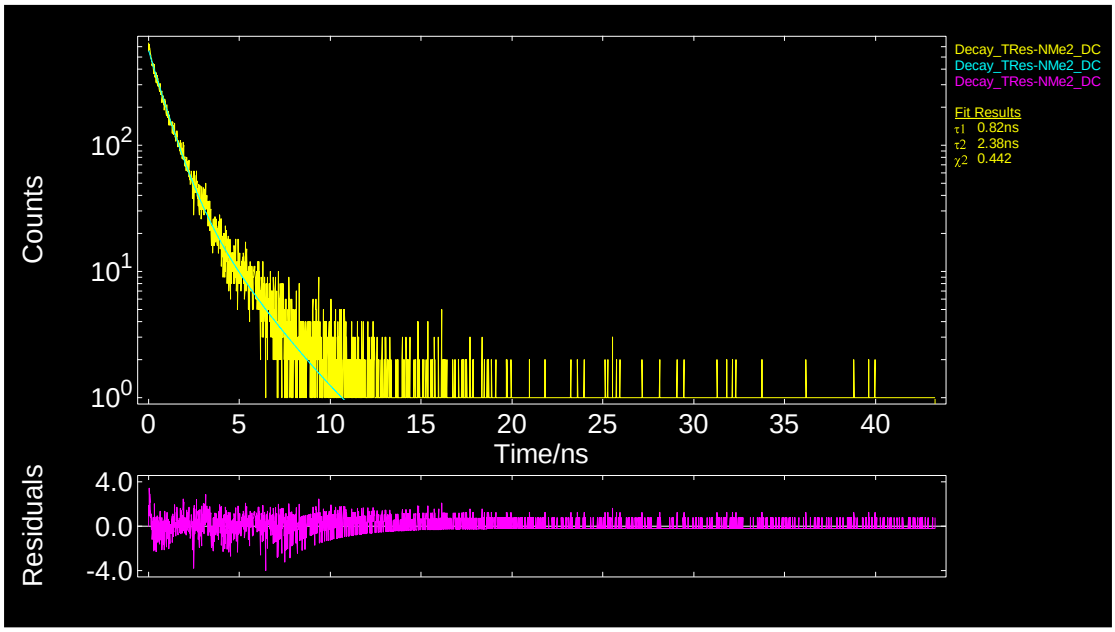

Figure S54. Lifetime decay profile of fluorescence band of **2** at 618 nm in CH_2Cl_2.

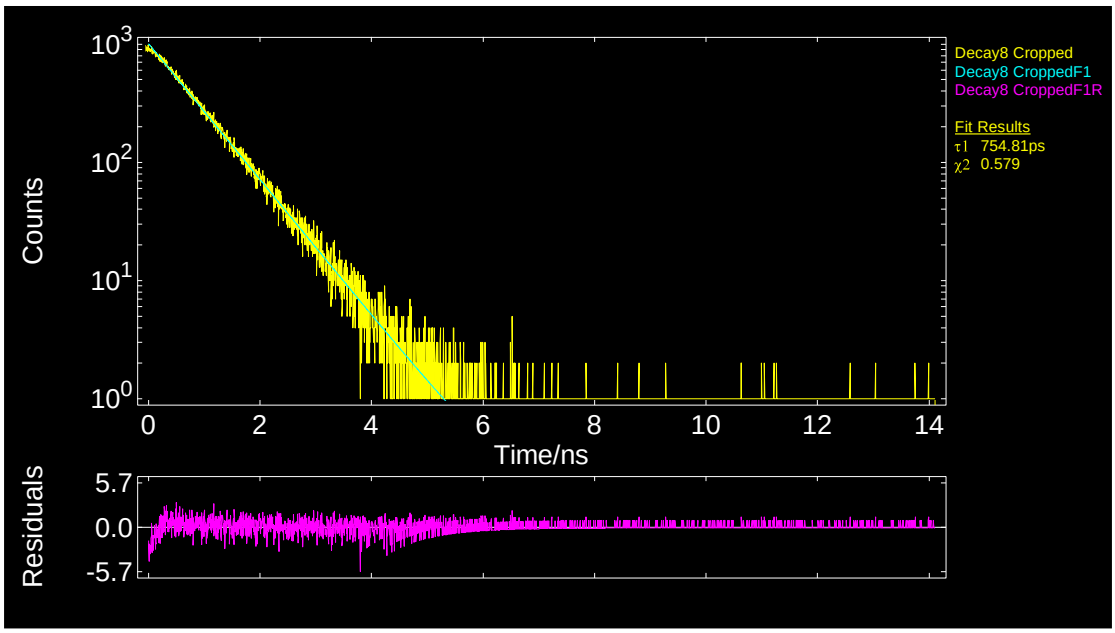

Figure S55. Lifetime decay profile of fluorescence band of **3** at 602 nm in CH_2Cl_2.

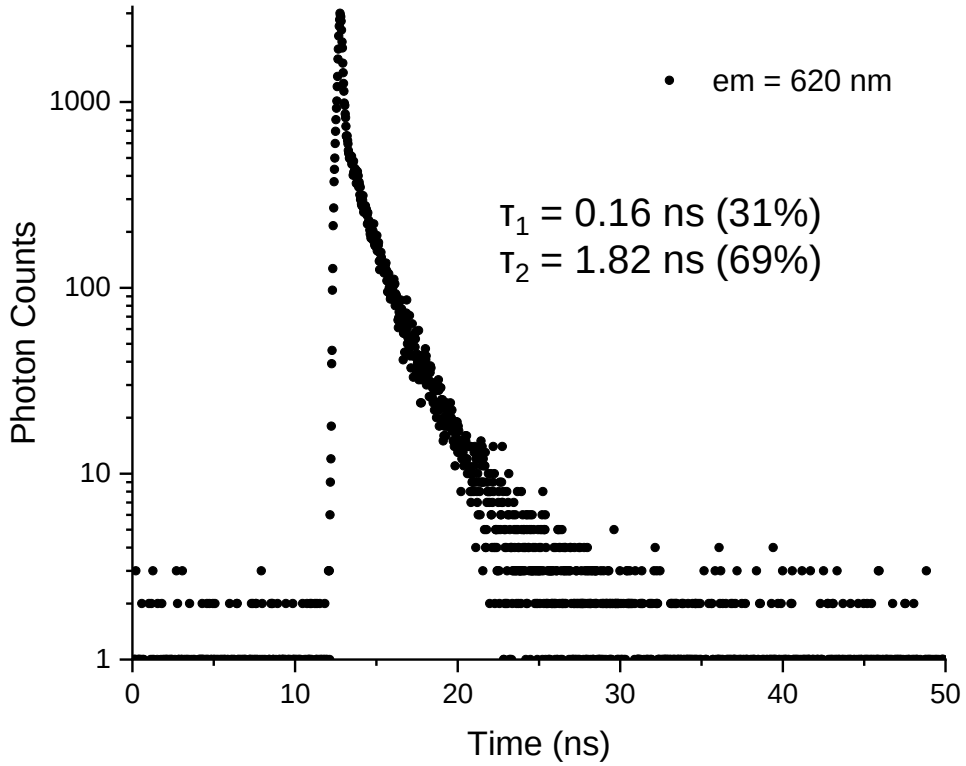

Figure S56. Lifetime decay profile of fluorescence band of **4** at 674 nm in CH_2Cl_2.

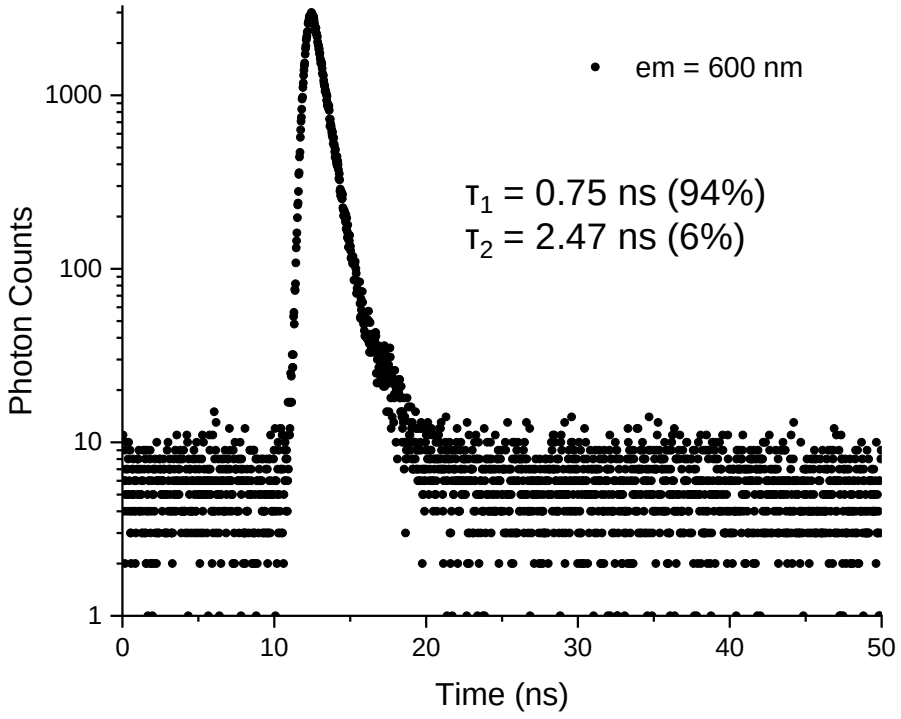

Figure S57. Lifetime decay profile of fluorescence band of **5** at 600 nm in CH_2Cl_2.

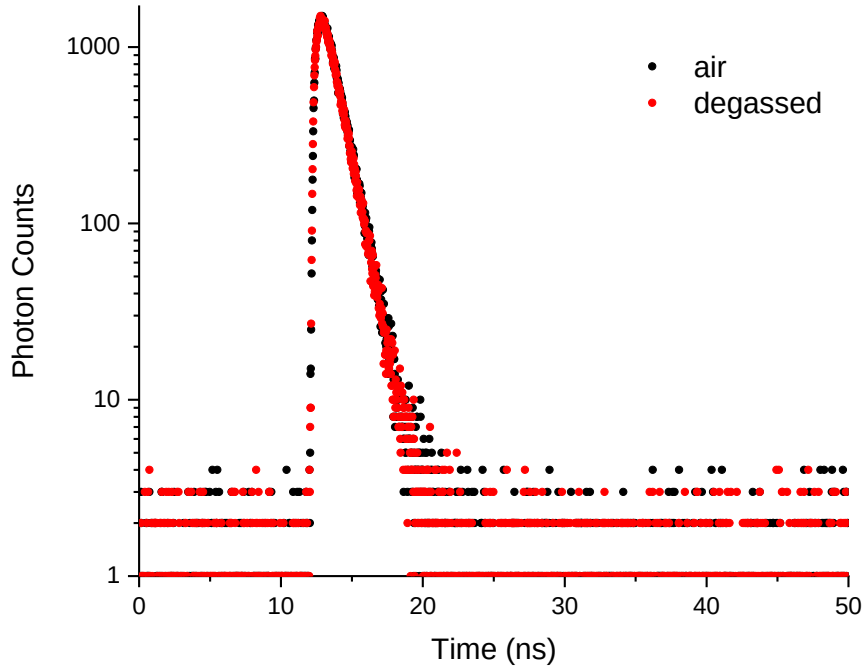

Figure S58. Lifetime decay profile of fluorescence band of **Pd-1** at 732 nm in degassed and air saturated CH_2Cl_2.

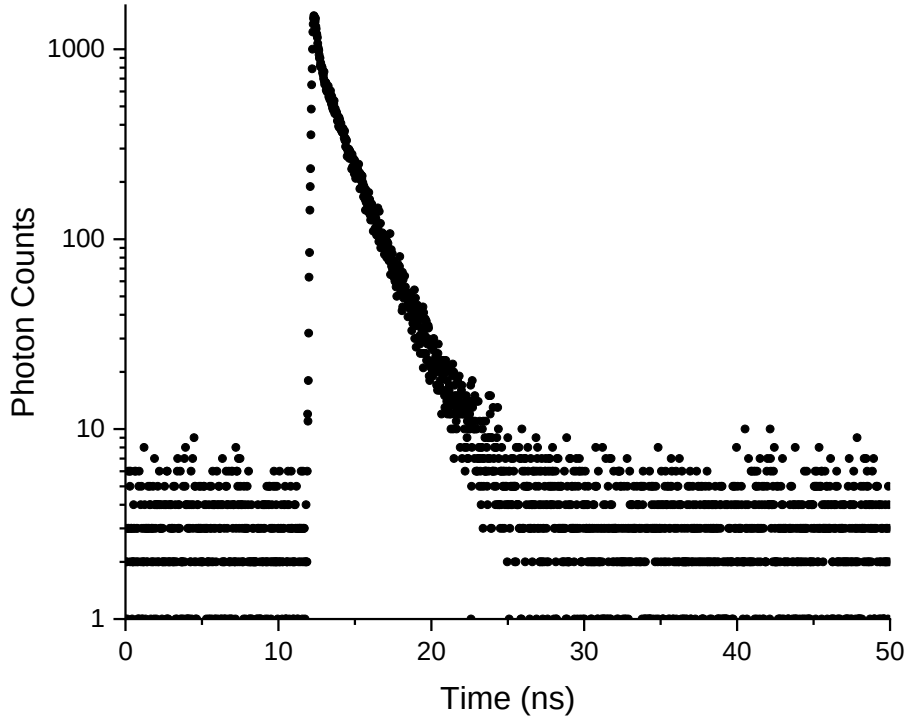

Figure S59. Lifetime decay profile of fluorescence band of **Pd-2** at 762 nm in CH_2Cl_2.

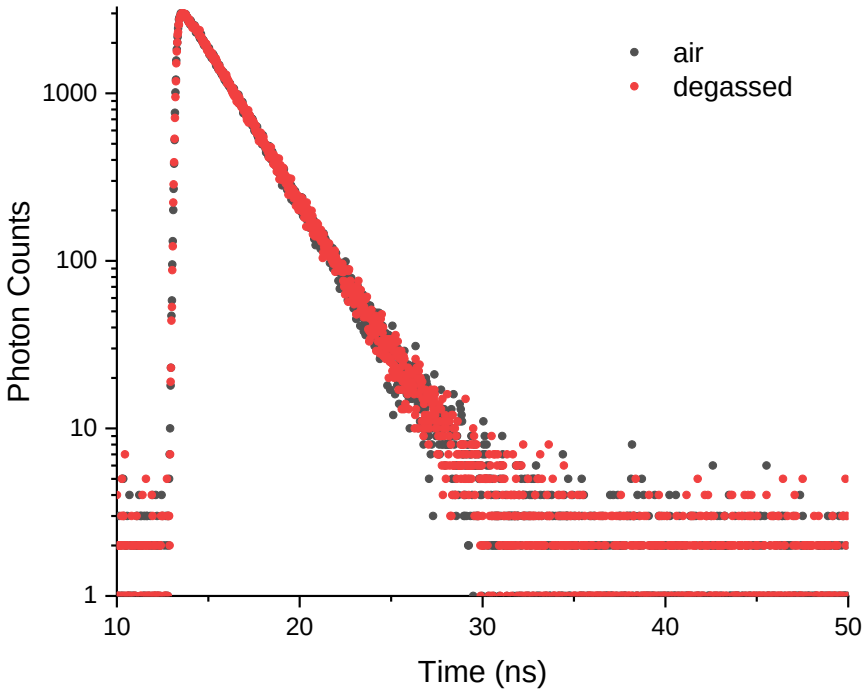

Figure S60. Lifetime decay profile of fluorescence band of **Pd-3** at 700 nm in degassed and air saturated CH_2Cl_2.

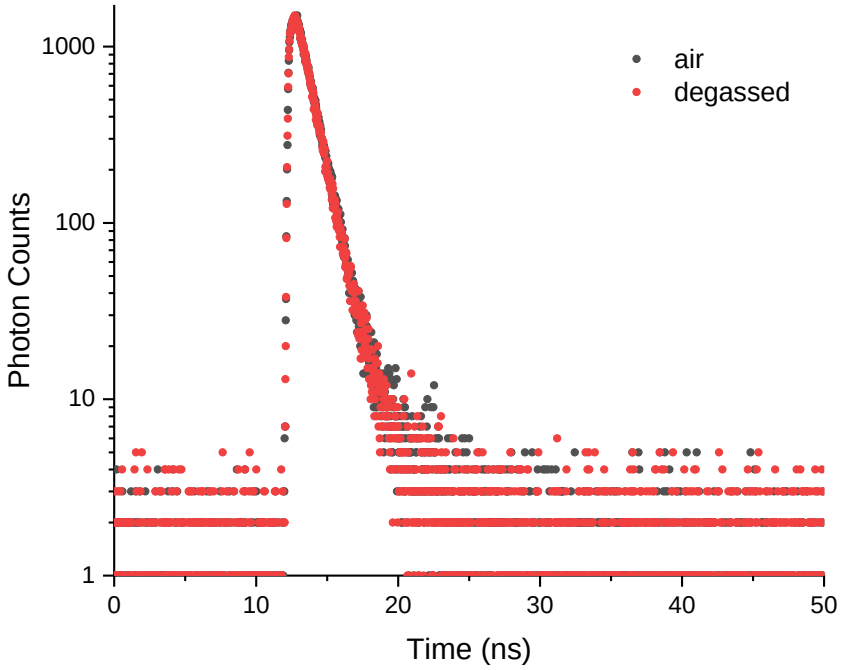

Figure S61. Lifetime decay profile of fluorescence band of **Pt-1** at 729 nm in degassed and air saturated CH_2Cl_2.

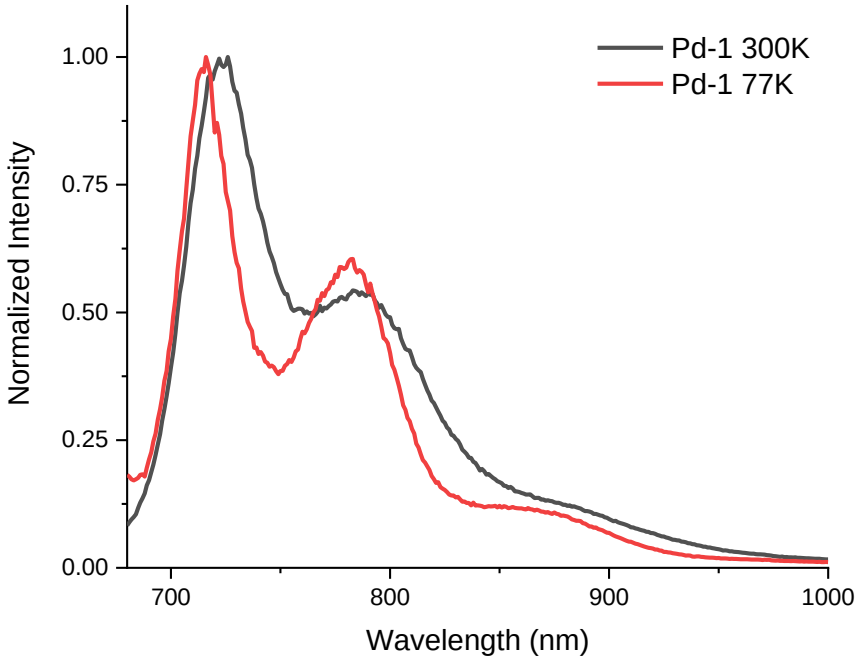

Figure S62. Emission spectra of **Pd-1** excited at 600 nm at 77 and 300 K in 2-methyltetrahydrofuran.

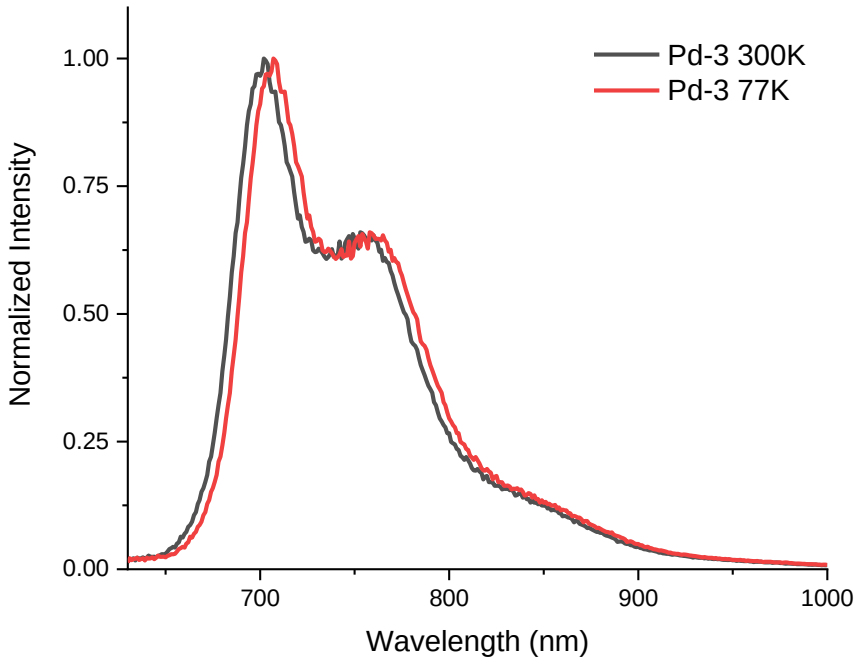

Figure S63. Emission spectra of **Pd-3** excited at 600 nm at 77 and 300 K in 2-methyltetrahydrofuran.

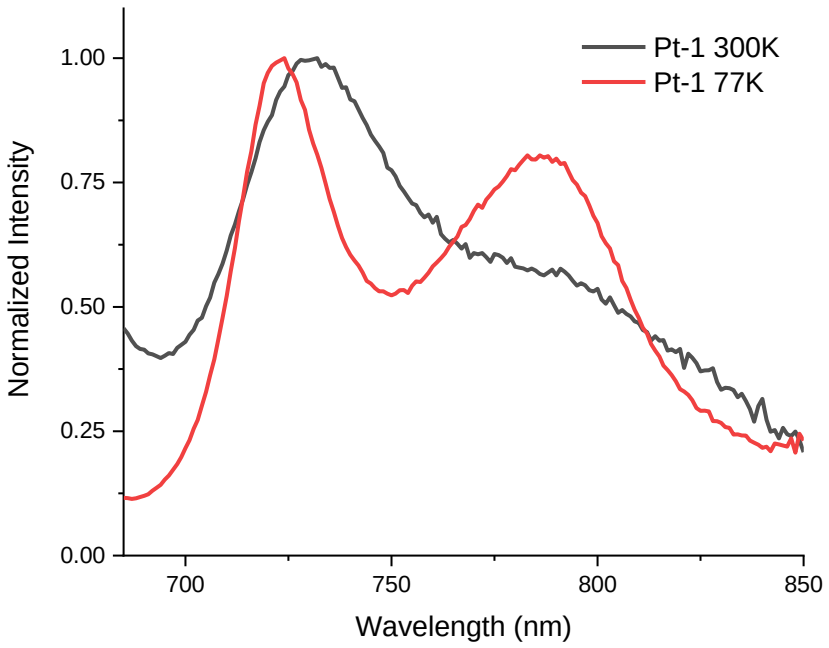

Figure S64. Emission spectra of **Pt-1** excited at 600 nm at 77 and 300 K in 2-methyltetrahydrofuran.

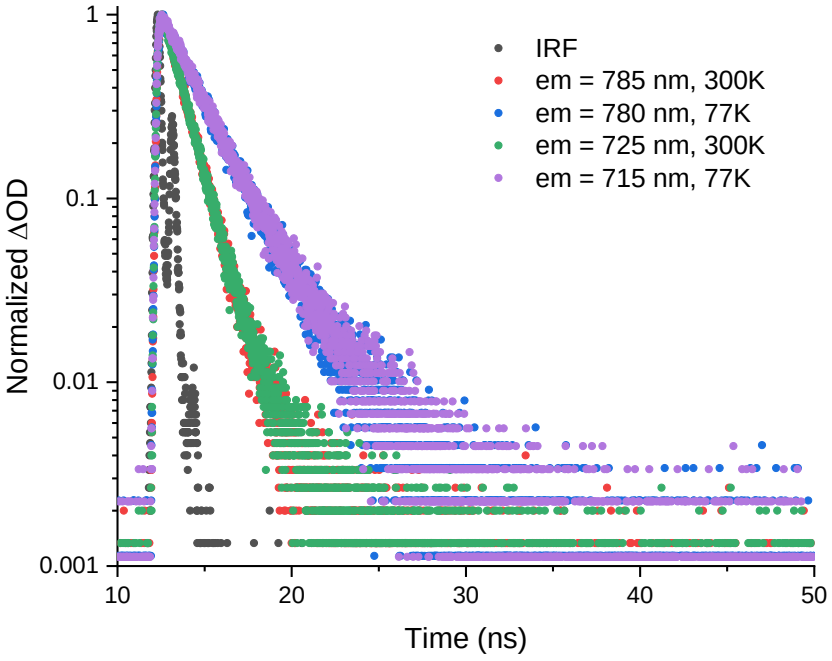

Figure S65. Lifetime decay profile of fluorescence band of **Pd-1** excited at 600 nm at 77 and 300 K in 2-methyltetrahydrofuran.

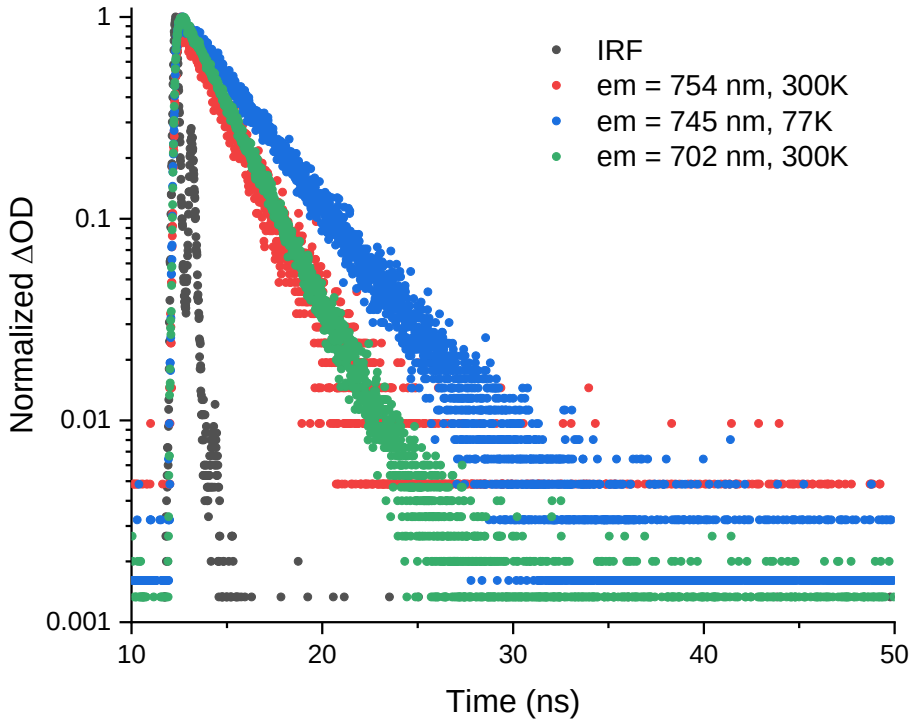

Figure S66. Lifetime decay profile of fluorescence band of **Pd-3** excited at 600 nm at 77 and 300 K in 2-methyltetrahydrofuran.

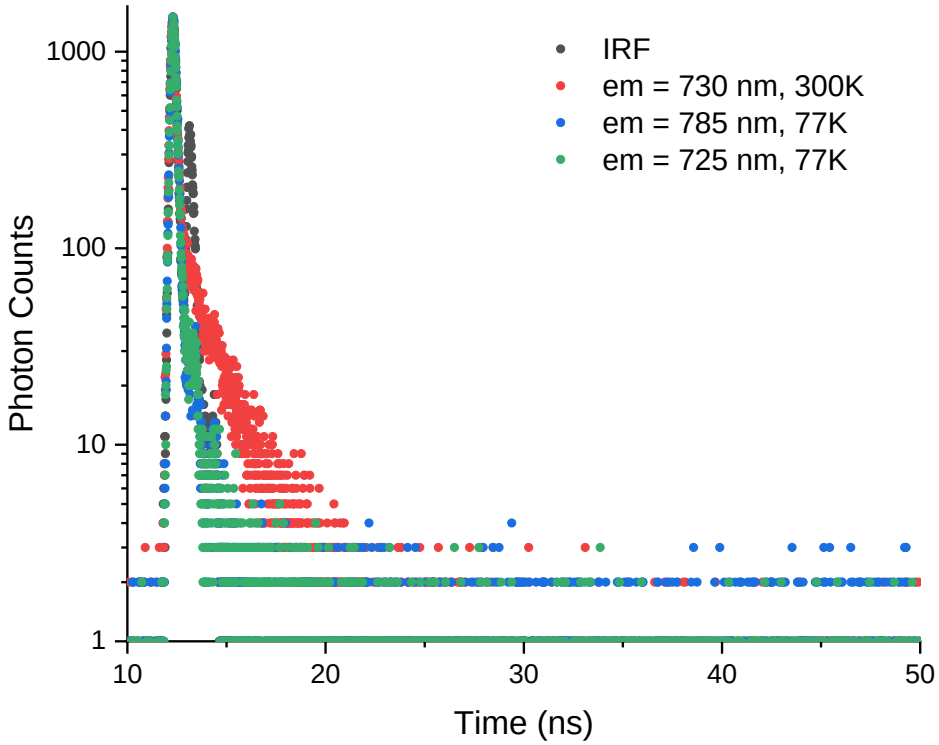

Figure S67. Lifetime decay profile of fluorescence band of **Pt-1** excited at 600 nm at 77 and 300 K in 2-methyltetrahydrofuran.

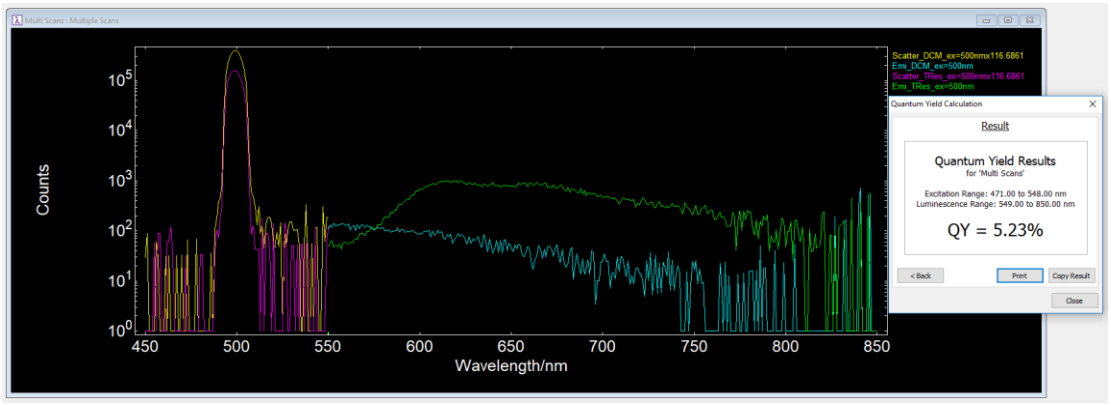

Figure S68. Absolute quantum yield of **1** in CH_2Cl_2.

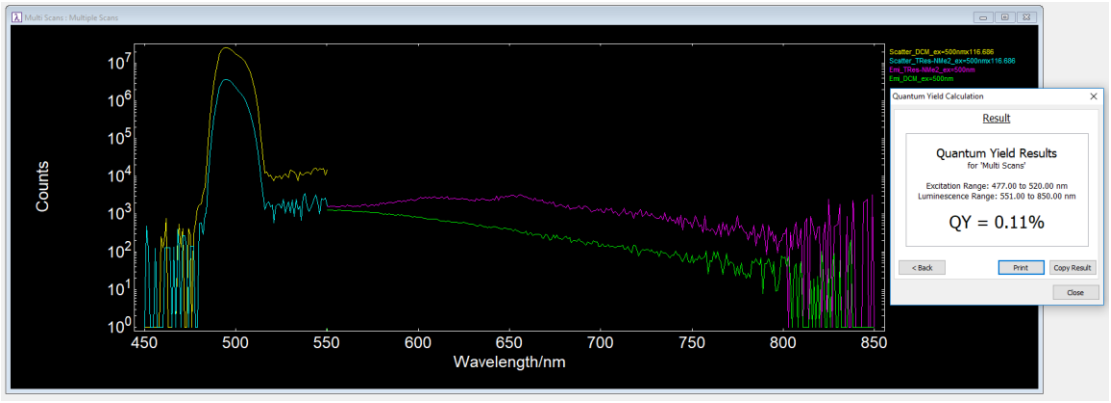

Figure S69. Absolute quantum yield of **2** in CH_2Cl_2.

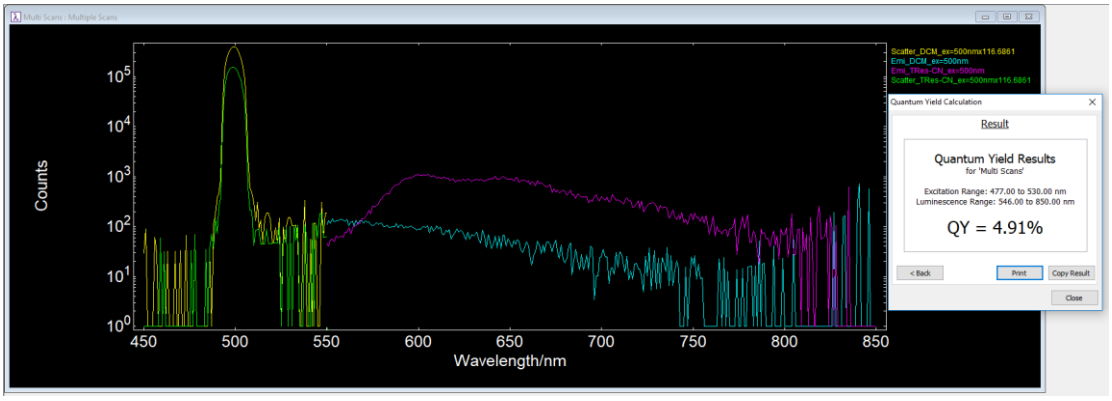

Figure S70. Absolute quantum yield of **3** in CH_2Cl_2.

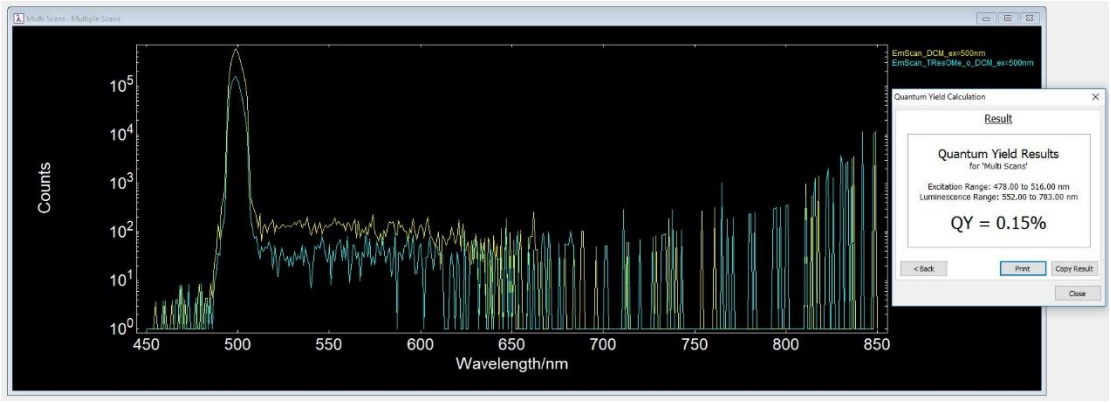

Figure S71. Absolute quantum yield of **4** in CH_2Cl_2.

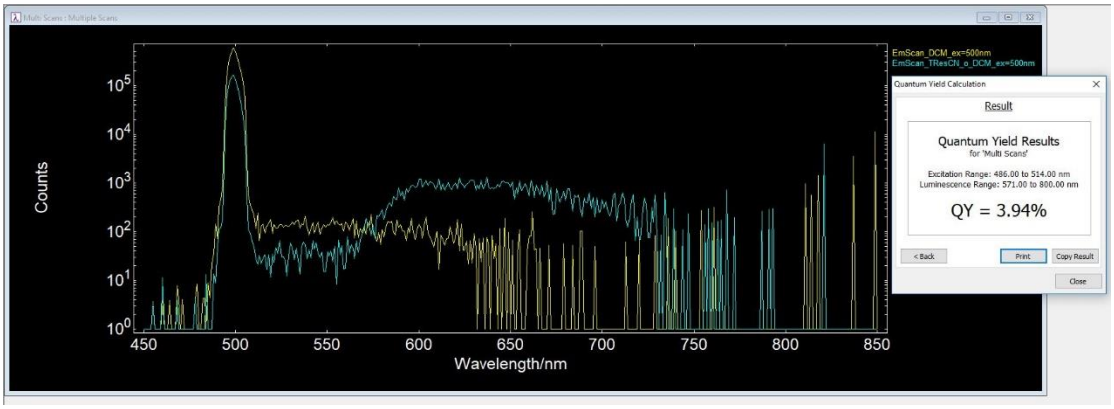

Figure S72. Absolute quantum yield of **5** in CH_2Cl_2.

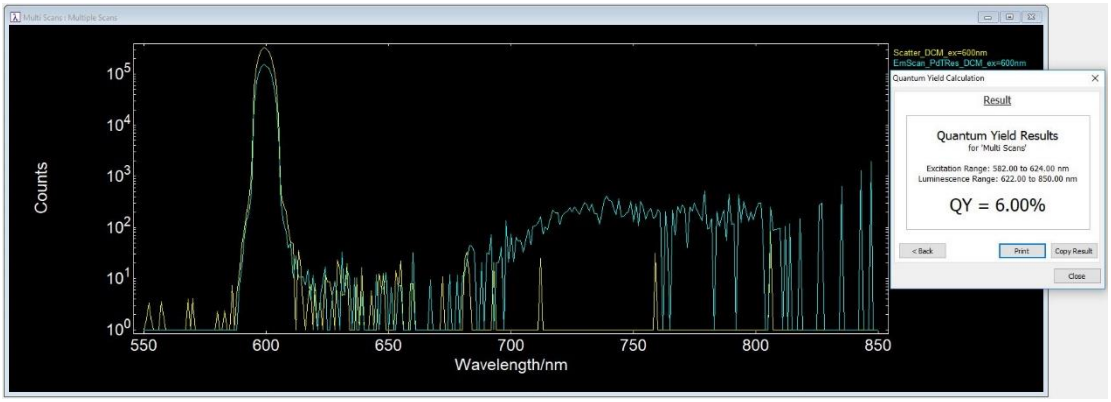

Figure S73. Absolute quantum yield of **Pd-1** in CH_2Cl_2.

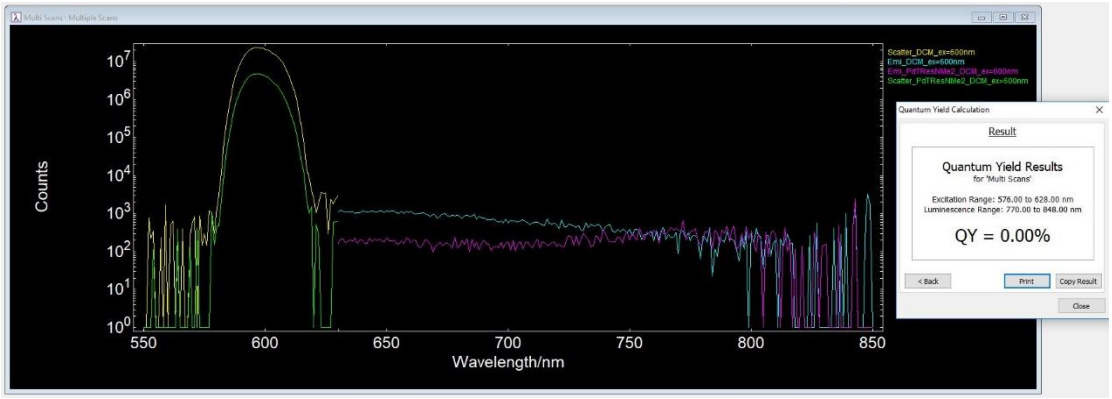

Figure S74. Absolute quantum yield of **Pd-2** in CH_2Cl_2.

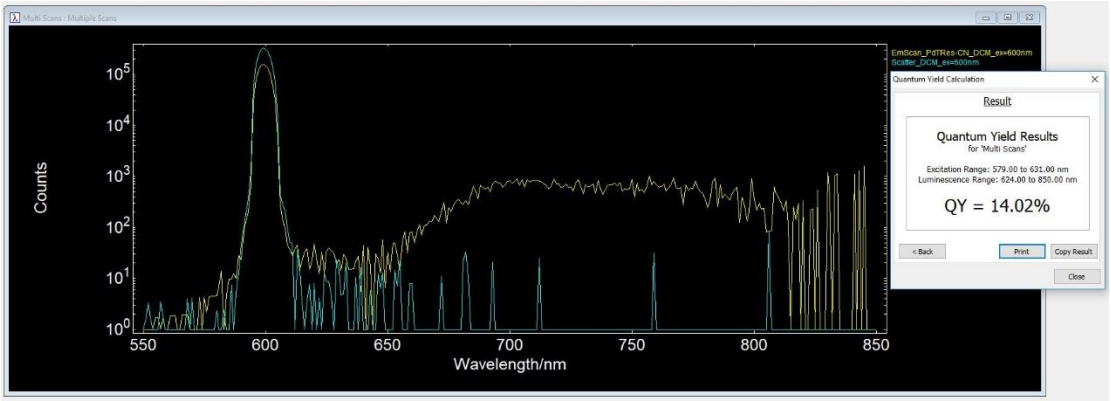

Figure S75. Absolute quantum yield of **Pd-3** in CH_2Cl_2.

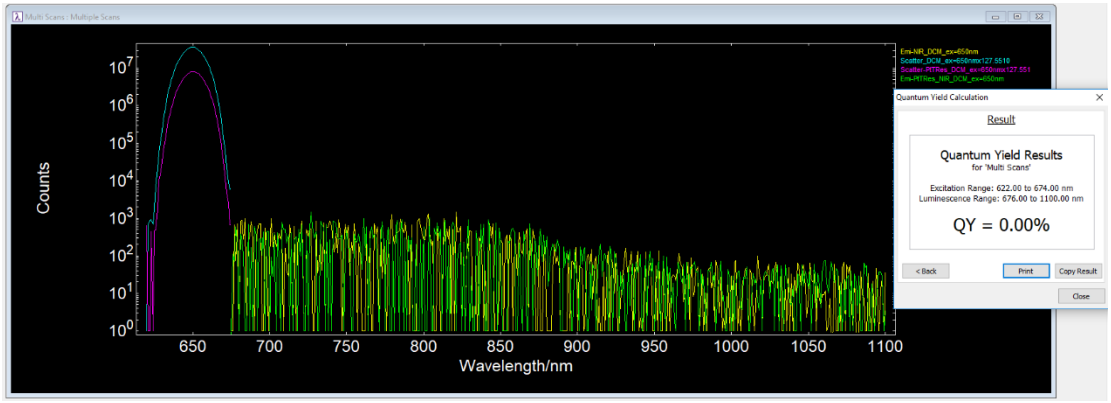

Figure S76. Absolute quantum yield of **Pt-1** in CH_2Cl_2.

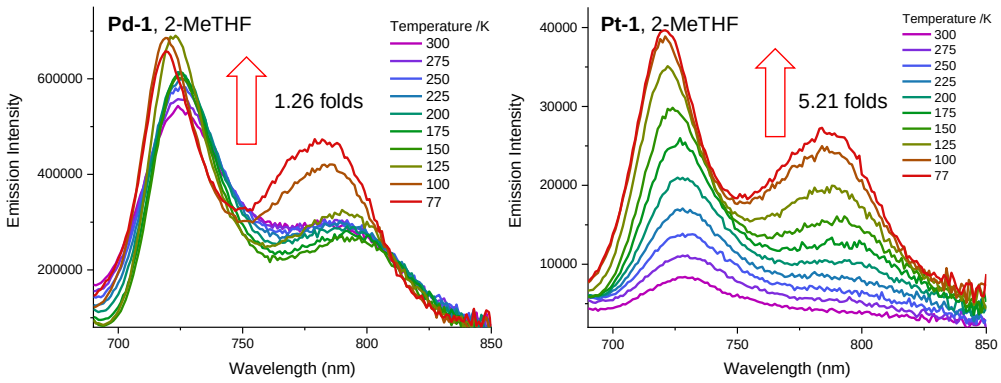

Figure S77. Temperature-dependent emission spectra of **Pd-1** and **Pt-1** in **2**-methyltetrahydrofuran collected from 77 to 300 K, excited at 600 nm.

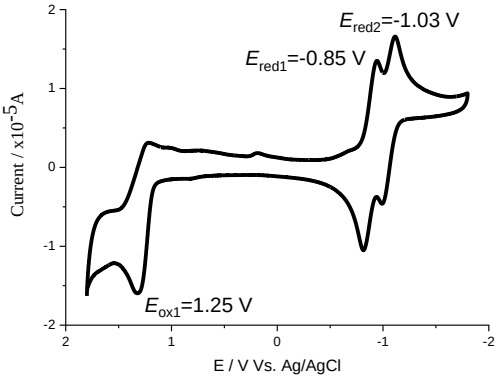

Figure S78. Cyclic voltammetry of **1** in CH_2Cl_2.

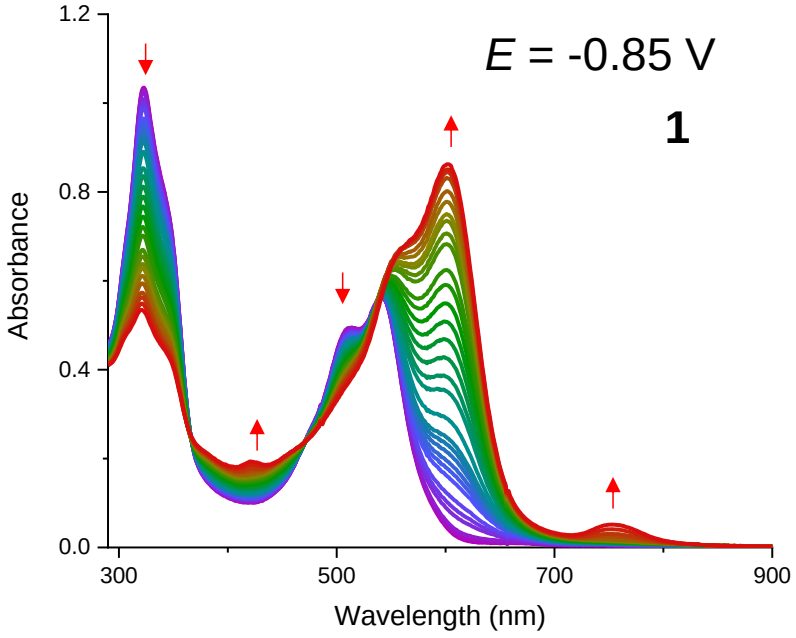

Figure S79. Spectroelectrochemistry in the first reduction potential of 1.0 mM **1** in CH_2Cl_2

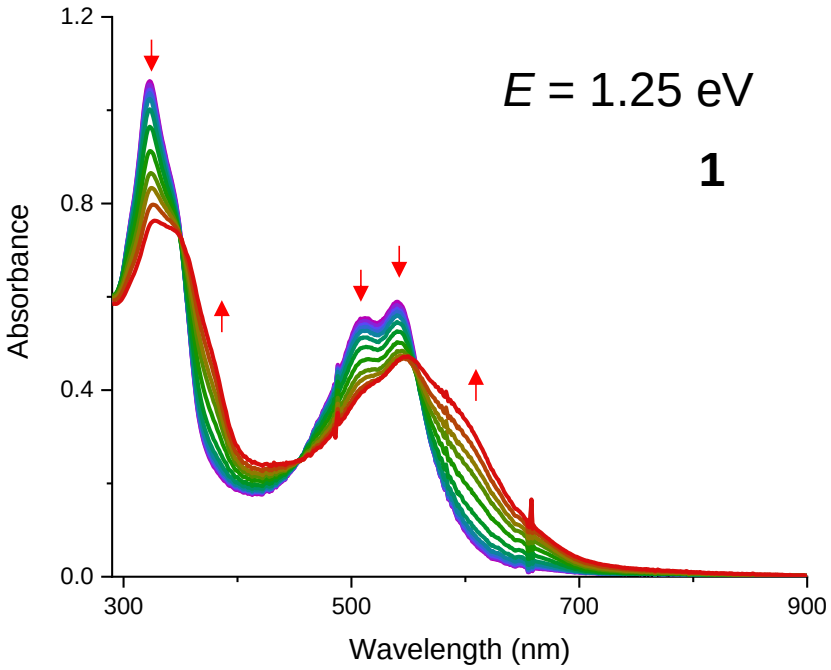

Figure S80. Spectroelectrochemistry in oxidation potential of 1.0 mM **1** in CH_2Cl_2.

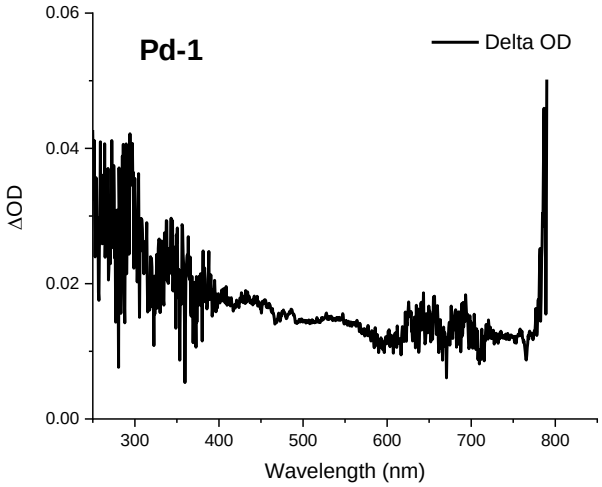

Figure S81. ns-TA spectra of **Pd-1** in degassed tetrahydrofuran upon excitation at 355 nm.

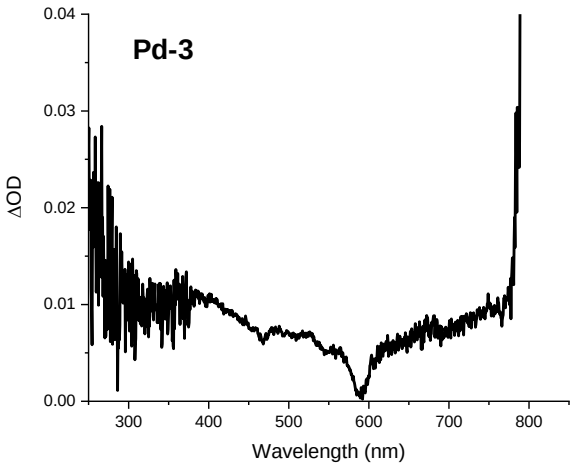

Figure S82. ns-TA spectra of **Pd-3** in degassed tetrahydrofuran upon excitation at 355 nm**.**

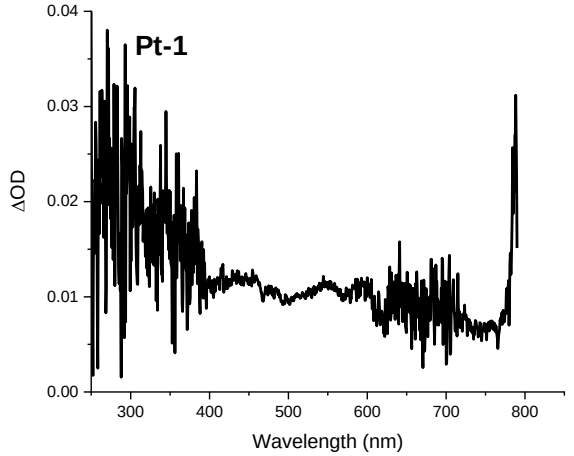

Figure S83. ns-TA spectra of **Pt-1** in degassed tetrahydrofuran upon excitation at 355 nm**.**

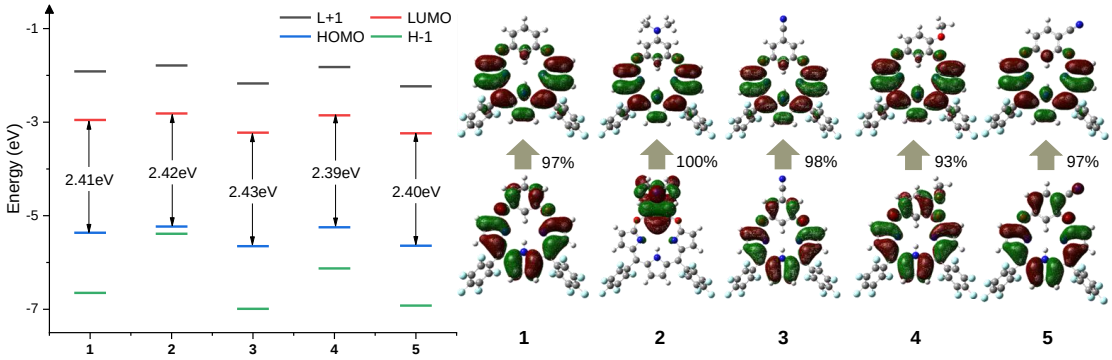

Figure S84. Energy diagrams and the corresponding nodal patterns of the frontier molecular orbitals (FMOs) of **1-5** calculated in the S_0 optimized sturctures at the B3LYP/6-311G(d) level.

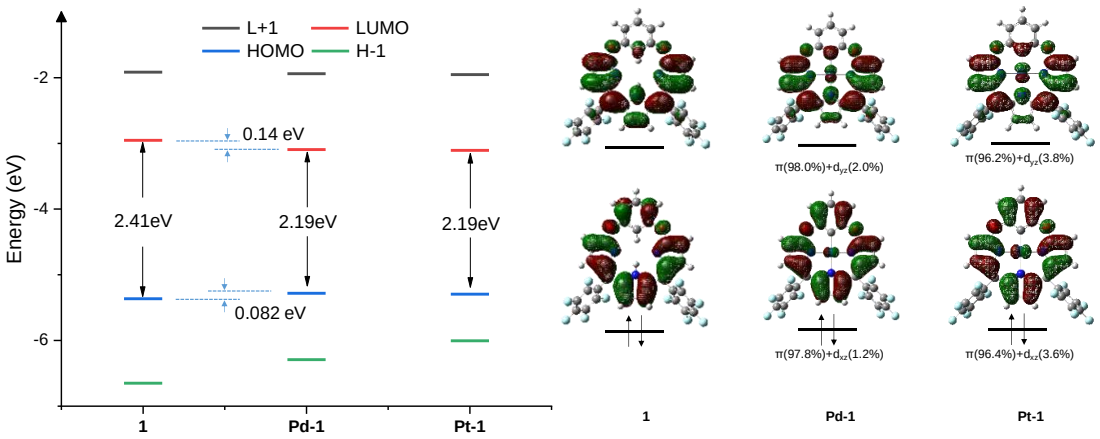

Figure S85. Energy diagrams and the corresponding nodal patterns of the frontier molecular orbitals (FMOs) of **1**, **Pd-1** and **Pt-1** calculated in the S_0 optimized sturctures at the B3LYP/6-311G(d)/Lanl2DZ/SDD level.

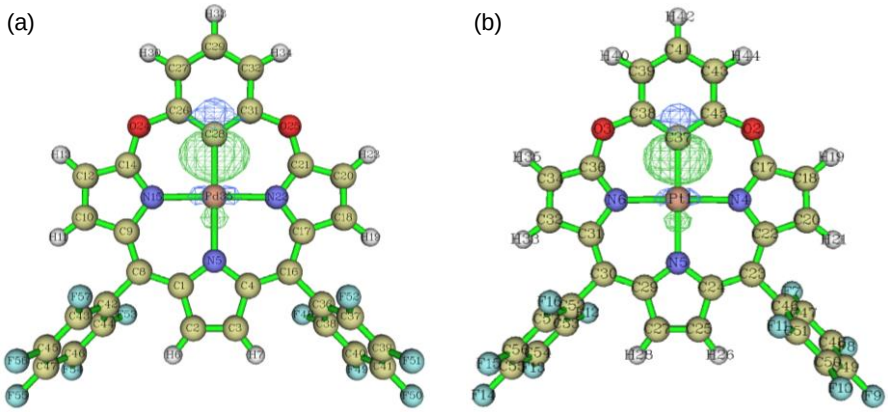

Figure S86. The natural localized molecular orbital (NLMO) analysis of (a) **Pd-1** and (b) **Pt-1** in the S_0 optimized sturctures at the B3LYP/6-311G(d)/Lanl2DZ/SDD level.

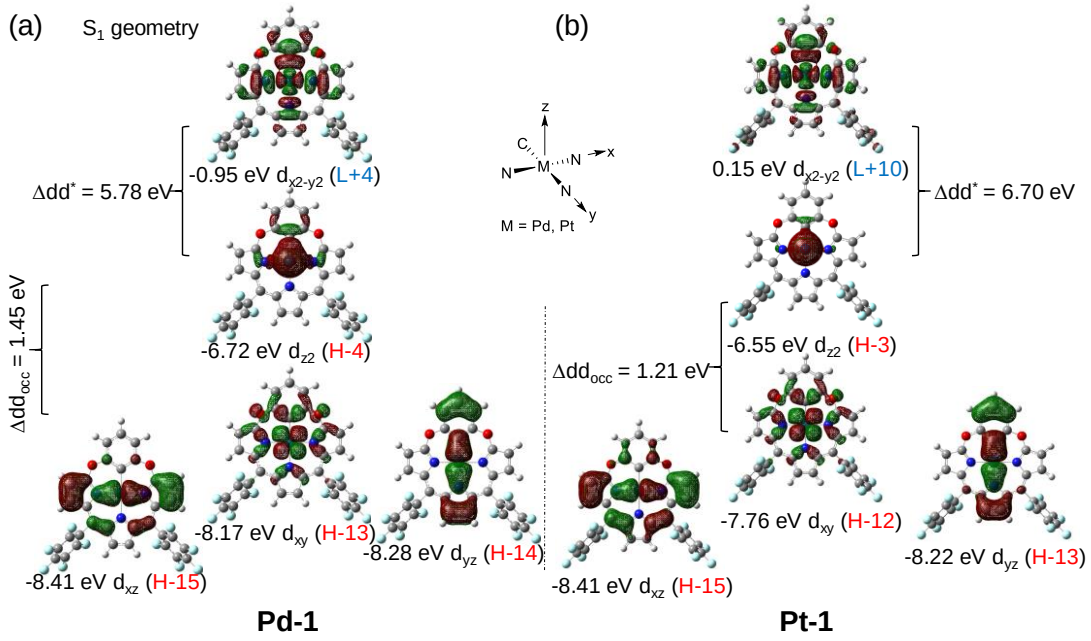

Figure S87. Nodal patterns of the metal-centered bonding orbitals of (a) **Pd-1** and (b) **Pt-1** calculated in the S_1 optimized sturctures at the TD-B3LYP/6-311G(d)/Lanl2DZ/SDD level.

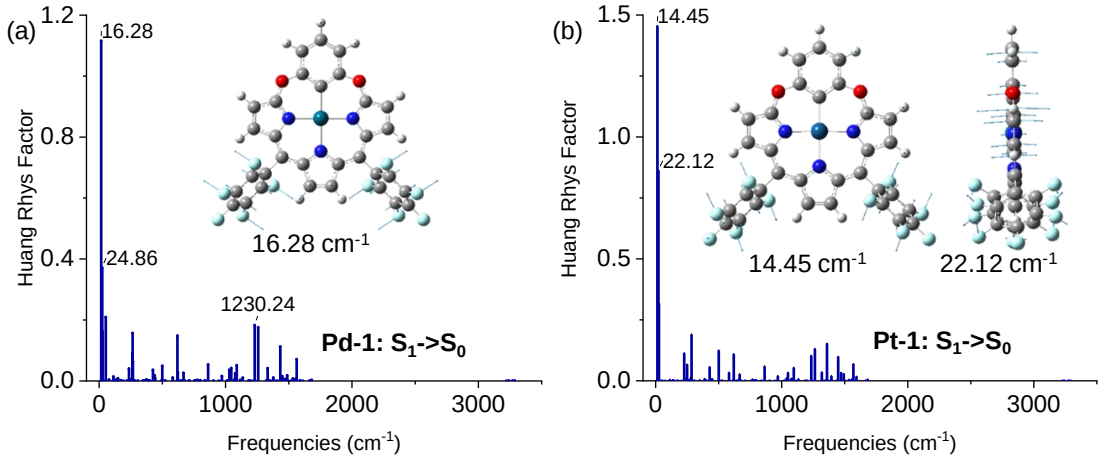

Figure S88. Huang-Rhys factors for energy conversion between S_1 and S_0 states of (a) **Pd-1** and (b) **Pt-1**, as well as the displacement vectors of important vibrational modes with the largest values of Huang-Rhys factor

To figure out the structure-property relationship during the energy conversion processes of $S_1 \rightarrow S_0$, we analyzed the Huang-Rhys factors as well as the displacement vectors of vibrational modes with the largest Huang-Rhys factors. For the conversion between S_1 and S_0 in **Pd-1**, many frequency vibrational modes in the range of 0~1700 cm^{-1} have significant Huang-Rhys factors which correspond to the torsional motion of pentafluorophenyl (11.4 and 25.6 cm^{-1}) and the in-plane ring stretch vibration (268.5-1368.2 cm^{-1}). Although the vibrational mode of largest Huang-Rhys factor correspond to the rotation motion of

pentafluorophenyl (11.4 cm^{-1}), the in-plane skeleton stretch vibration of tripyrrin and bridging phenyl ring also play important role in relaxing S_1 state of **Pd-1**. Herein, the nonradiative relaxation channels of S_1 state of Pd-1 are assigned to these two kind of molecular motions. Especially, the negligible barrier of free rotation motion of pentafluorophenyl is sure to accelerate the nonradiative decay to a large extent, thus contributes to the larger nonradiative transition rates than fluorescence. For **Pt-1**, the situation is almost same as **Pd-1** except for another non-negligible non-radiative channel, which corresponds for the out-plane vibration of tripyrrin plane (22.12 cm^{-1}). The larger number of non-radiative vibrational channels of **Pt-1** leads to the larger non-radiative rate constant (7.46×10^7 s^{-1}, in Table 2) compared with **Pd-1** (4.04×10^7 s^{-1}), which induces the almost quenched luminescence in **Pt-1**.

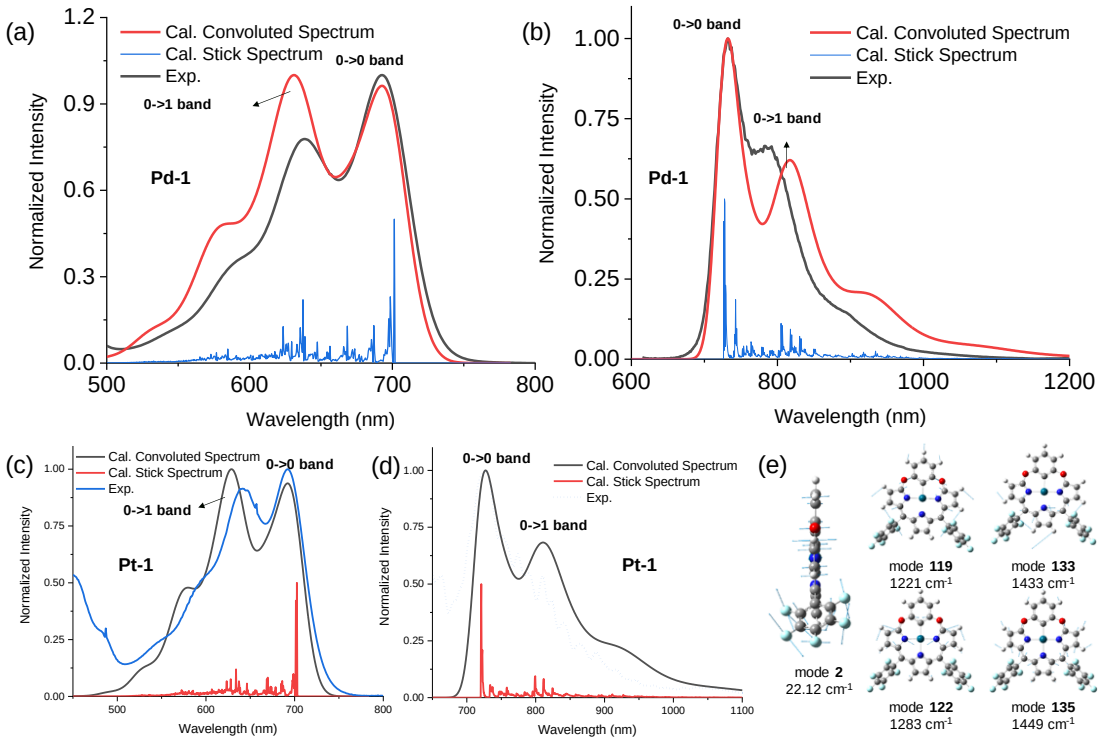

Figure S89. Reproduction of experimental (a, c) absorption and (b, d) emission spectra of S_1 excited state in **Pd-1** and **Pt-1** by the computation of vibrationally resolved spectra using FCclasses 2.1, in which the convoluted spectra were obtained by Gaussian broadening from the stick spectra with a full width at half maximum (FWHM) factor of 0.035 eV (~282 cm-1). And the (e) assignments of 0-> 1 transition vibronic band in the emission spectra of **Pt-1**. To compare the vibronic band, the 0->0 bands of computational spectra of were manually hypsochromic shifted 44 and 18 nm for absorption and emission spectra respectively due to the under-estimation of adiabatic energy difference between ground state and S1 excited state by TD-B3LYP

From the results of fs-TA spectra and non-radiative channel analysis, we knew that the non-radiative channel is highly related to structural relaxation and vibrational state in S_1 state. It's also known to all that photoluminescence is intrinsically involved in the effect of the nuclear motions of molecules. Thus the vertical excitation energies cannot reveal the detailed spectral information. Vibrationally resolved spectra are essential to straightforwardly compare with experimental data and find the mode-specific effect on the spectra. So we simulated the electronic absorption and emission spectra with fine structures including vibronic transitions in Figure S88. The experimental absorption and emission spectra of S_1 state of **Pd-1** and **Pt-1** can be well reproduced by vibrationally resolved computations, which intensively confirms the accuracy of displacement and torsion effects of all the normal vibration modes. This also reveal the rationality of harmonic approximation in these system and the credibility of calculated photophysical rate constants. We then assigned the vibronic band of emission spectra in **Pt-1** as the 0->1 band, which is mainly associated to the vibrational mode 2 (22.12 cm^{-1}), 119 (1221 cm^{-1}), 122 (1283 cm^{-1}), 133 (1433 cm^{-1}) and 135 (1449 cm^{-1}). Among them, the of vibrational mode 2 (22.12 cm^{-1}) is successfully correlated to the significant vibrational channel of **Pt-1** observed in fs-TA in Figure 3 and the theoretical analysis of non-radiative channel in Figure 5c and S87. Above all, all these experimental and theoretical results consistently and directly reveal the non-radiative vibrational channel in S_1 state of **Pt-1**, which significantly quenches the emission of **Pt-1**.

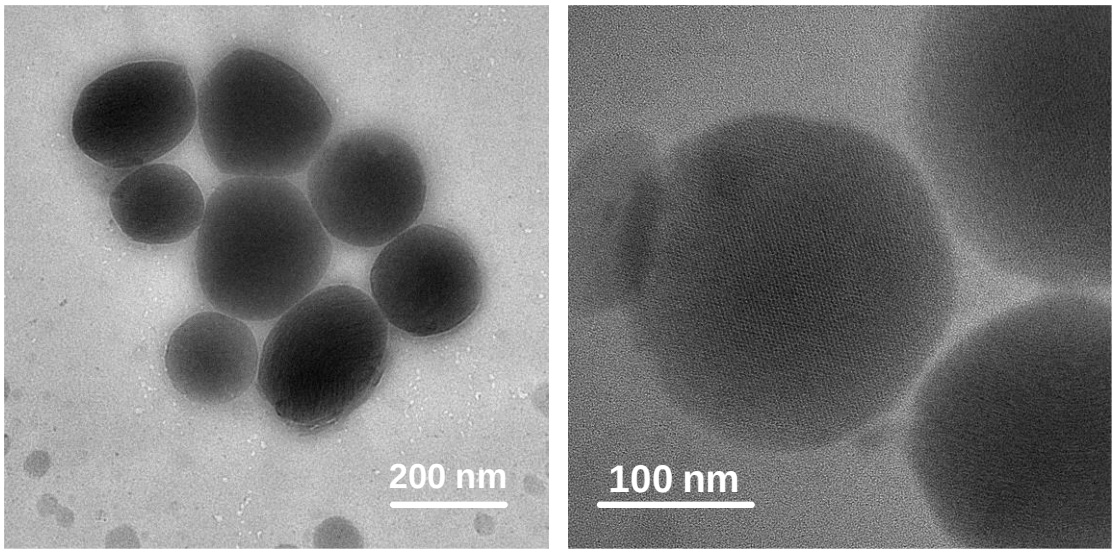

Figure S90. TEM imging of MSN-F127.

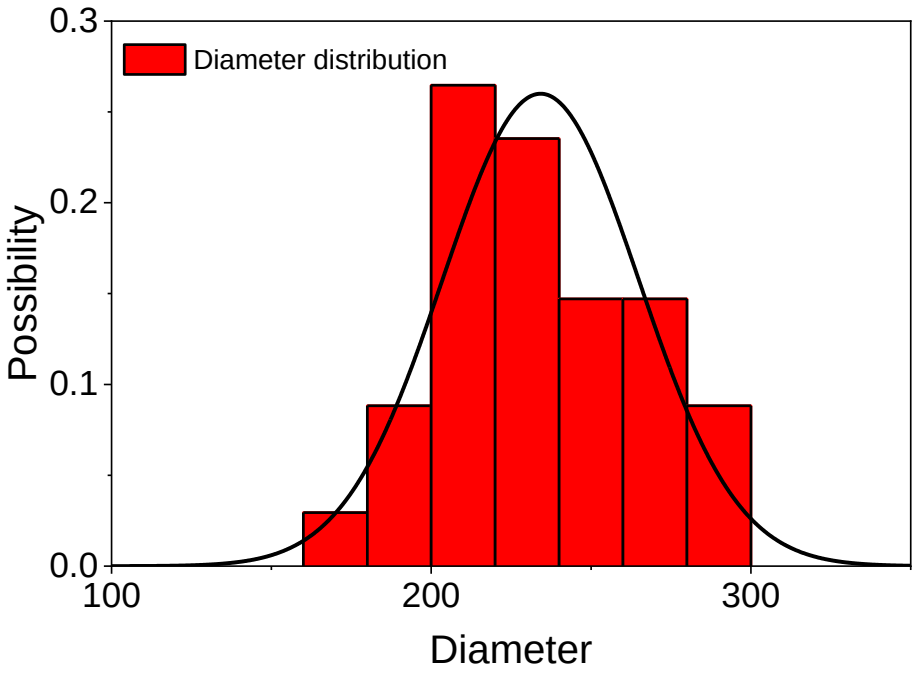

Figure S91. DLS spectra of MSN-F127.

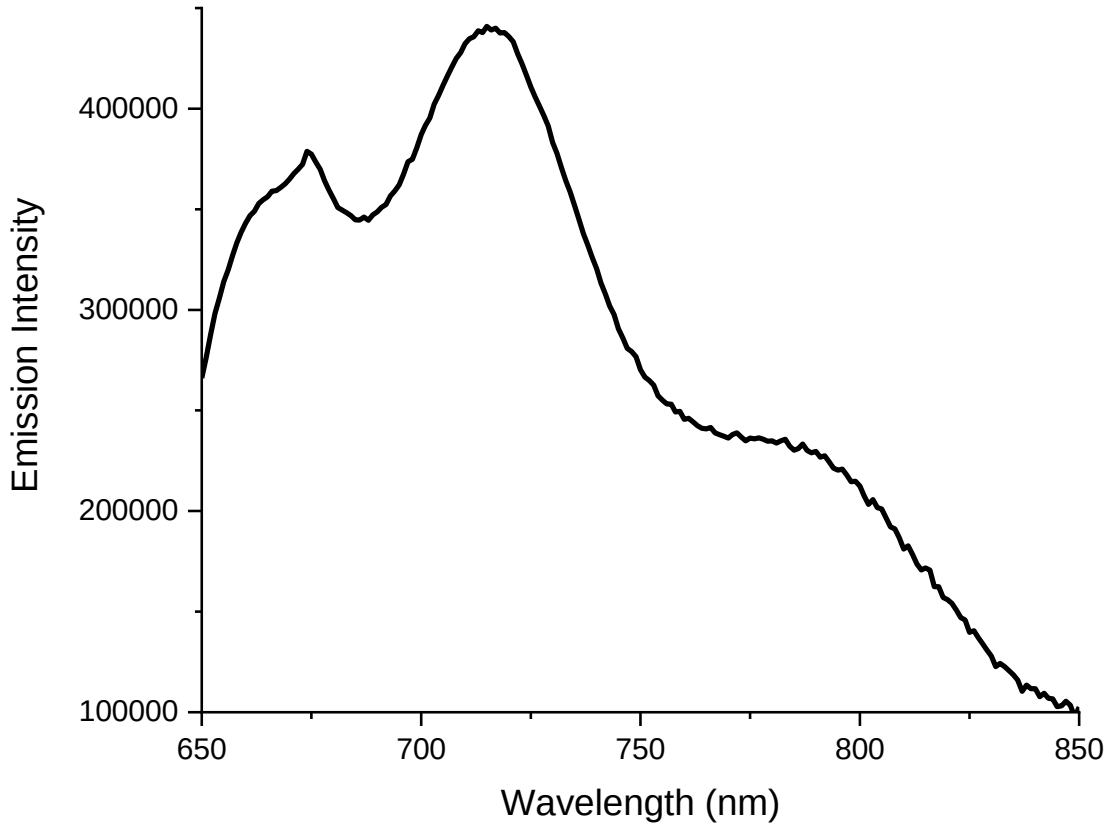

Figure S92. Emission spectra of **Pd-1-MSN-F127** excited at 600 nm in water.

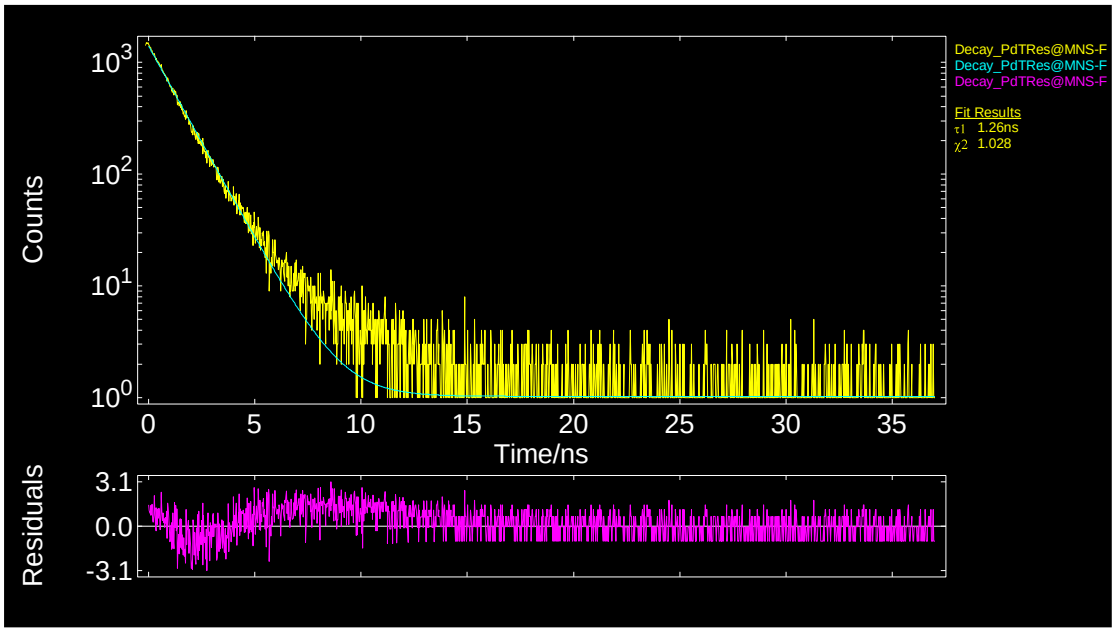

Figure S93. Lifetime measurement of **Pd-1-MSN-F127** excited at 600 nm in water.

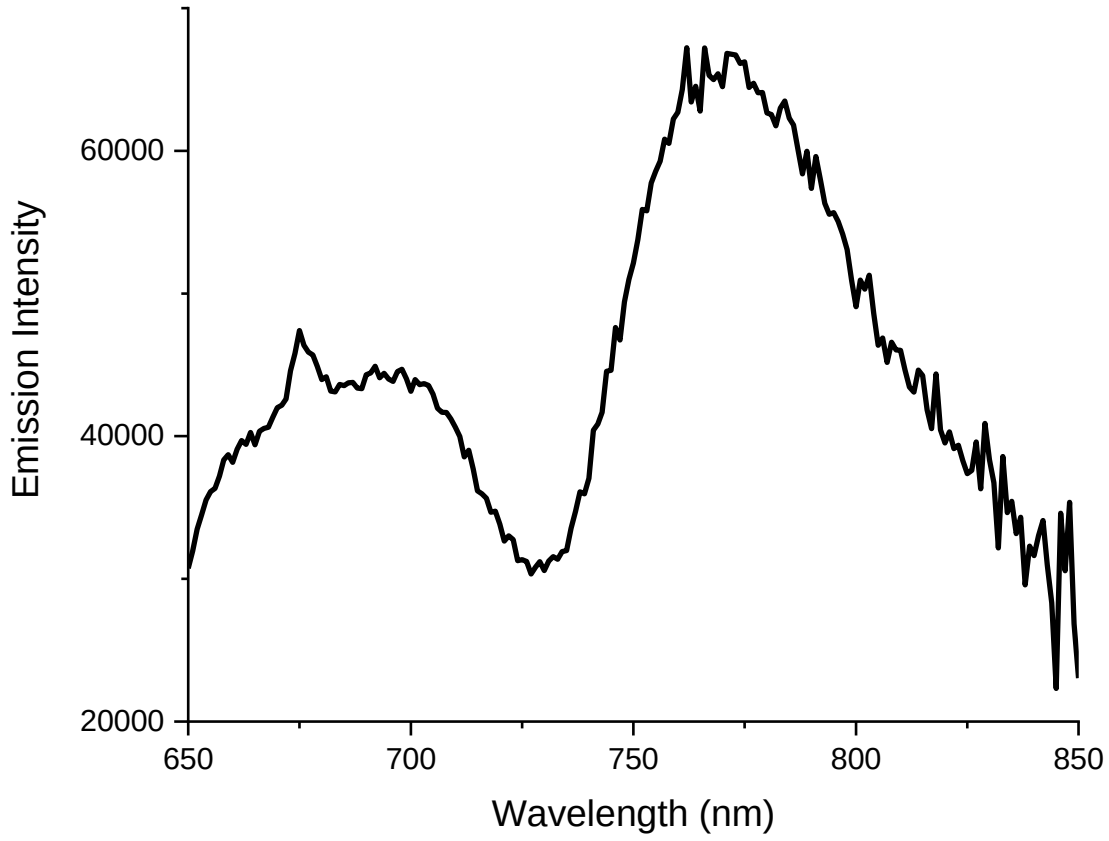

Figure S94. Lifetime measurement of **Pd-3-MSN-F127** excited at 600 nm in water.

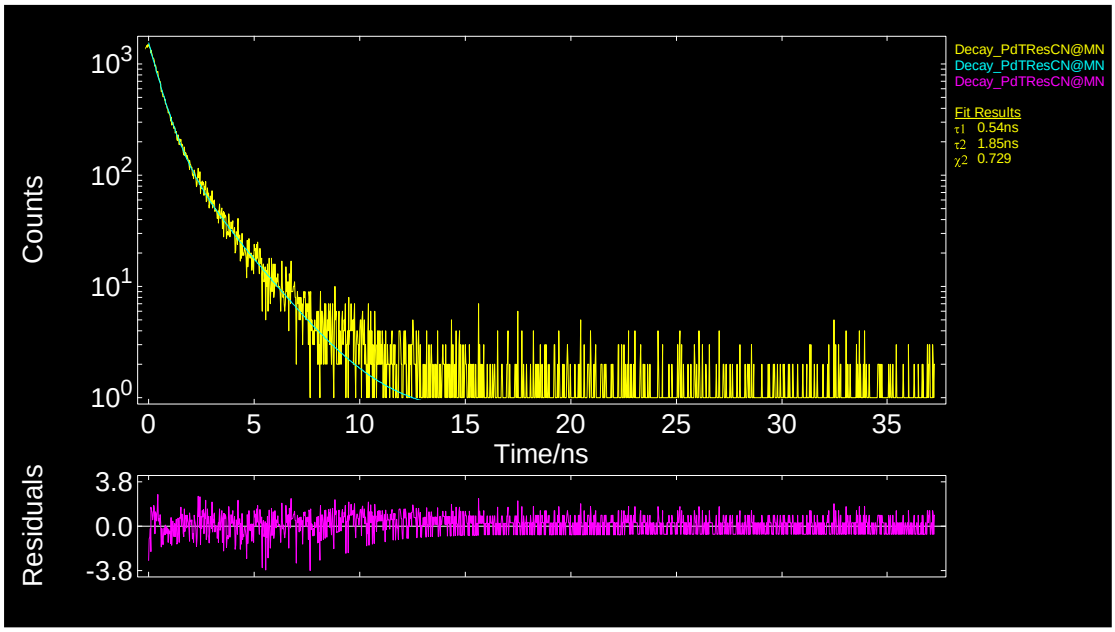

Figure S95. Emission spectra of **Pd-3-MSN-F127** excited at 600 nm in water.

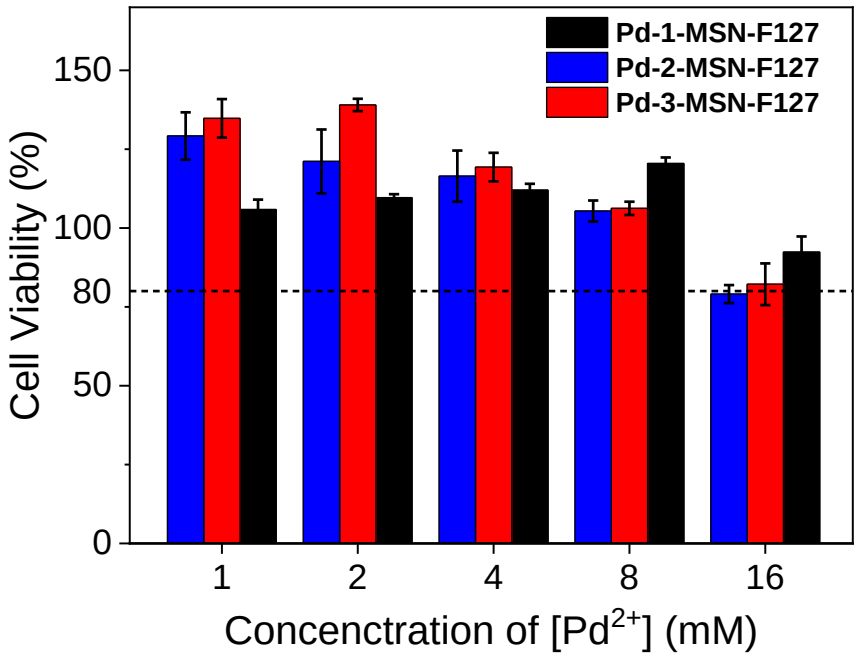

Figure S96. Cytotoxicity of **Pd-1**, **Pd-2** and **Pd-3-MSN-F127** assessed by a CCK-8 toolkit in HeLa cells.

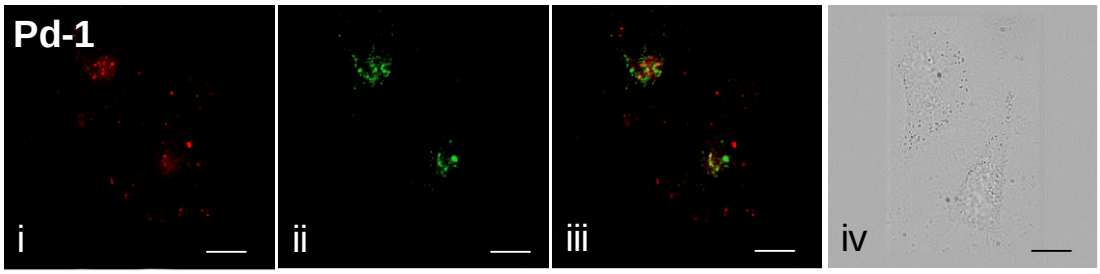

Figure S97. Confocal fluorescence image of (i) living HeLa cells with **Pd-1-MSN-F127** by em >776 nm channel under laser excitation at 700 nm; (ii) LysoTracker Green DND-26; (iii) merged confocal fluorescence images of (i) and (ii); (iv) differential interference contrast (DIC) images. Images of **Pd-1-MSN-F127** (incubated for 12h) were presented with fake color; scale bar presents 20 μm.

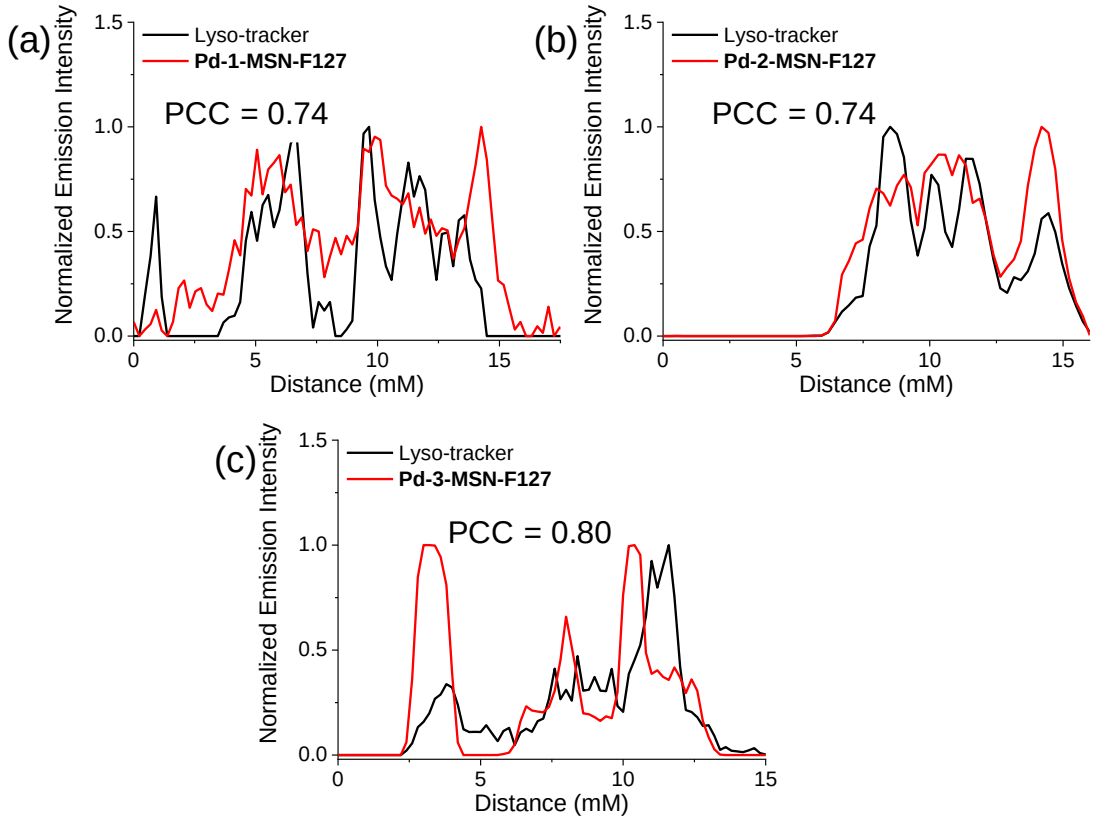

Figure S98. The Pearson coefficient of (a) **Pd-1**, (b) **Pd-2** and (c) **Pd-3-MSN-F127** with LysoTracker Green DND-26.

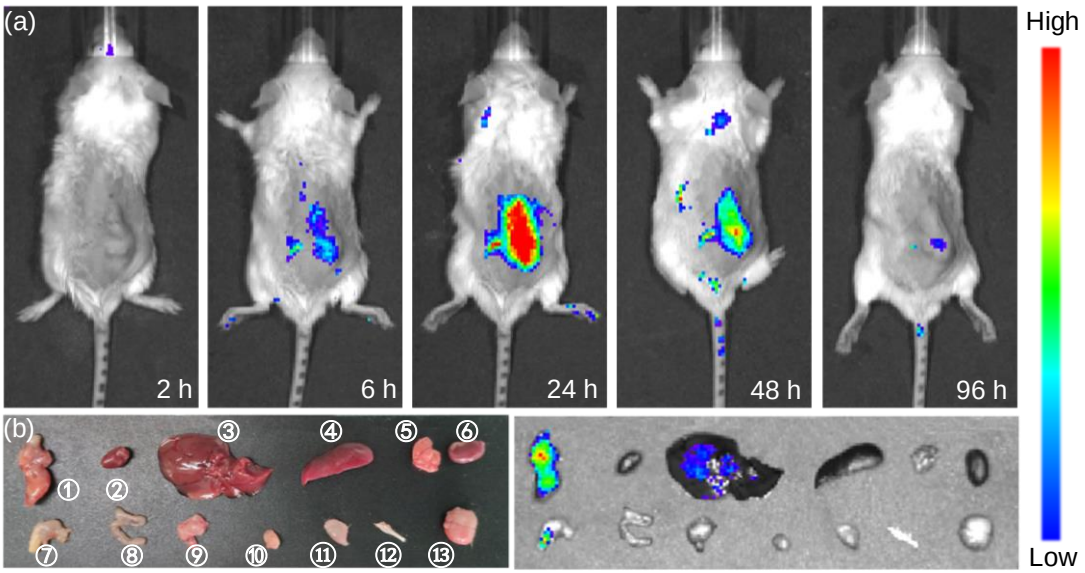

Figure S99. (a) Fluorescence imaging of 4T1 tumor-bearing mice after intravenous injection of **Pd-1-MSN-F127** at different time points. (b) Photograph (left) and fluorescence imaging (right) of main organs of 4T1 tumor-bearing mice at 96 h p.i. of **Pd-1-MSN-F127**. ① ~⑬ stand for tumor, heart, liver, spleen, lung, kidney, stomach, intestine, pancreas, bladder, muscle, bone, and brain, respectively. (λ_{ex} = 710 nm, λ_{em} = 776 nm).

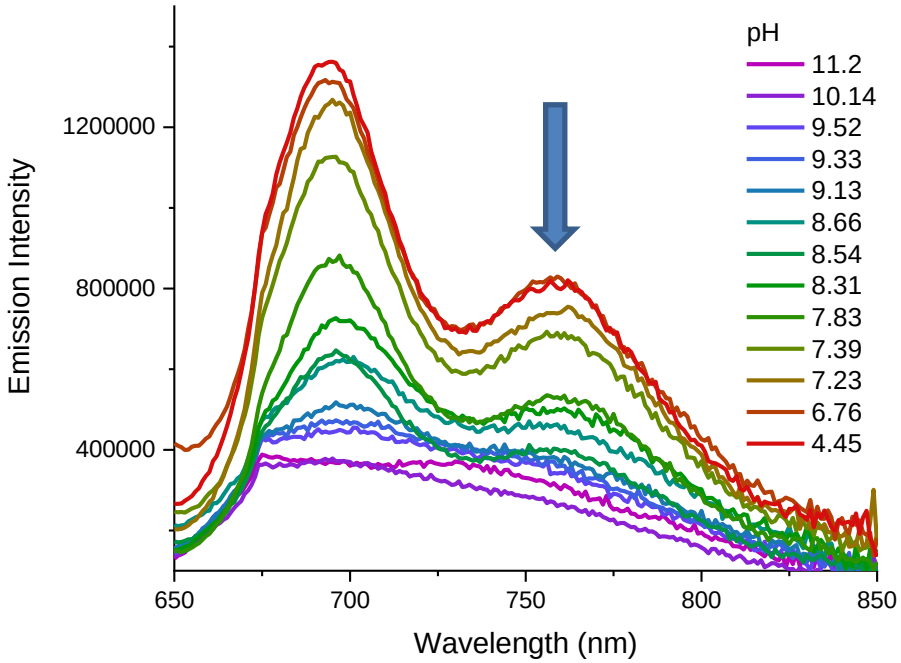

Figure S100. pH sensitive NIR emission of **Pd-2-MSN-F127**.

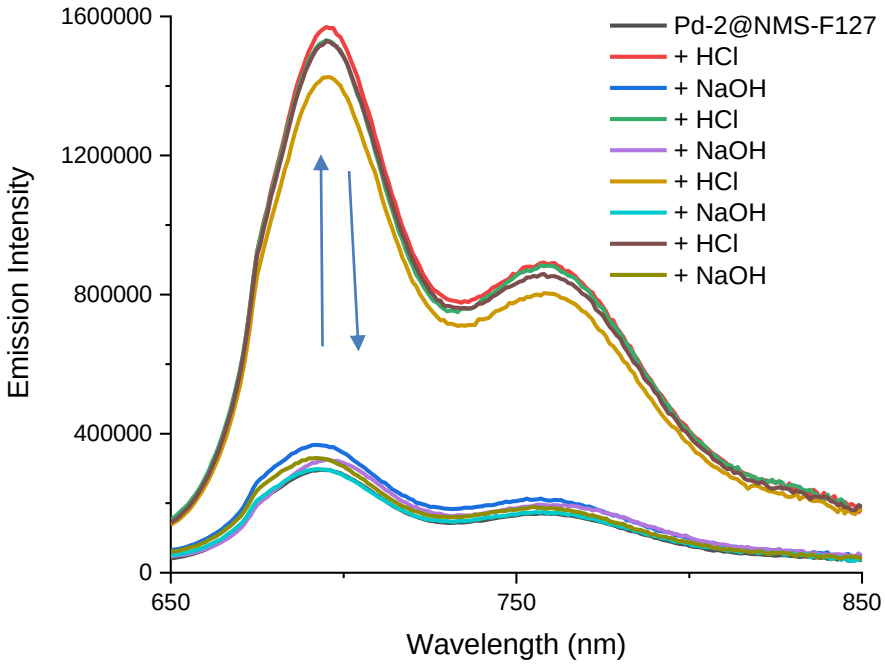

Figure S101. Reversible switching on/off NIR emission of **Pd-2-MSN-F127** between pH 5 and 10.

4. Reference.

1. a) G. M. Sheldrick, *Acta. Crystallogr. A*, 2008, **64**, 112-122; b) G. M. Sheldrick, *Acta Crystallogr. C*, 2015, **71**, 3-8.
2. O. V. Dolomanov, L. J. Bourhis, R. J. Gildea, J. A. K. Howard and H. Puschmann, *J. Appl. Crystallogr.*, 2009, **42**, 339-341.
3. A. L. Spek, *Acta Crystallogr D Biol Crystallogr*, 2009, **65**, 148-155.
4. a) C. Lee, W. Yang and R. G. Parr, *Phys. Rev. B: Condens. Matter Mater. Phys.*, 1988, **37**, 785–789; b) A. D. Becke, *J. Chem. Phys.*, 1993, **98**, 5648–5652.
5. M. J. Frisch, G. W. Trucks, H. B. Schlegel, G. E. Scuseria, M. A. Robb, J. R. Cheeseman, G. Scalmani, V. Barone, B. Mennucci, G. A. Petersson, H. Nakatsuji, M. Caricato, X. Li, H. P. Hratchian, A. F. Izmaylov, J. Bloino, G. Zheng, J. L. Sonnenberg, M. Hada, M. Ehara, K. Toyota, R. Fukuda, J. Hasegawa, M. Ishida, T. Nakajima, Y. Honda, O. Kitao, H. Nakai, T. Vreven, J. A. Montgomery, J. E. P. Jr., F. Ogliaro, M. Bearpark, J. J. Heyd, E. Brothers, K. N. Kudin, V. N. Staroverov, R. Kobayashi, J. Normand, K. Raghavachari, A. Rendell, J. C. Burant, S. S. Iyengar, J. Tomasi, M. Cossi, N. Rega, J. M. Millam, M. Klene, J. E. Knox, J. B. Cross, V. Bakken, C. Adamo, J. Jaramillo, R. Gomperts, R. E. Stratmann, O. Yazyev, A. J. Austin, R. Cammi, C. Pomelli, J. W. Ochterski, R. L. Martin, K. Morokuma, V. G. Zakrzewski, G. A. Voth, P. Salvador, J. J. Dannenberg, S. Dapprich, A. D. Daniels, Ö. Farkas, J. B. Foresman, J. V. Ortiz, J. Cioslowski and D. J. Fox, *Gaussian 09 (Revision E.01)*, Gaussian Inc., Wallingford CT, 2009.
6. a) M. M. Francl, W. J. Petro, W. J. Hehre, J. S. Binkley, M. S. Gordon, D. J. DeFree and J. A. Pople, *J. Chem. Phys.*, 1982, **77**, 3654-3665; b) P. C. Hariharan and J. A. Pople, *Theor. Chem. Acc.*, 1978, **28**, 213.
7. P. J. Hay and W. R. Wadt, *J. Chem. Phys.*, 1985, **82**, 299-310.
8. a) D. Andrae, U. Haeussermann, M. Dolg, H. Stoll and H. Preuss, *Theor. Chim. Acta*, 1990, **77**, 123–141; b) J. M. L. Martin and A. Sundermann, *J. Chem. Phys.*, 2001, **114**, 3408–3420.
9. a) J. P. Foster and F. Weinhold, *J. Am. Chem. Soc.*, 1980, **102**, 7211-7218; b) A. E. Reed and F. Weinhold, *J. Chem. Phys.*, 1985, **83**, 1736-1740.
10. a) S. G. Chiodo and M. Leopoldini, *Comput. Phys. Commun.*, 2014, **185**, 676-683; b) X. Gao, S. Bai, D. Fazzi, T. Niehaus, M. Barbatti and W. Thiel, *J. Chem. Theory Comput.*, 2017, **13**, 515–524.
11. a) Y. L. Niu, Q. A. Peng, C. M. Deng, X. Gao and Z. G. Shuai, *J. Phys. Chem. A*, 2010, **114**, 7817-7831; b) Q. Peng, Y. Niu, Q. Shi, X. Gao and Z. Shuai, *J. Chem. Theory. Comput.*, 2013, **9**, 1132-1143; c) Z. G. Shuai, Q. Peng, Y. L. Niu and H. Geng, *MOMAP, a molecular materials property prediction package, revision 0.2.004*, Tsinghua University: Beijing, China, http://www.shuaigroup.net/, 2014; d) Q. Peng, D. Fan, R. Duan, Y. Yi, Y. Niu, D. Wang and Z. Shuai, *J. Phys. Chem. C*, 2017, **121**, 13448-13456; e) Y. Niu, W. Li, P. Qian, G. Hua and Z. Shuai, *Mol. Phys.*, 2018, **116**, 1-13.
12. a) F. Santoro, *FCclasses, a Fortran 77 code*, http://village.ipcf.cnr.it; b) F. Santoro, R. Improta, A. Lami and V. Barone, *J. Chem. Phys.*, 2007, **126**, 184102; c) F. Santoro, R. Improta, A. Lami, J. Bloino and V. Barone, *J. Chem. Phys.*, 2007, **126**, 084509; d) F. Santoro, R. Improta, A. Lami, J. Bloino and V. Barone, *J. Chem. Phys.*, 2008, **128**, 224311; e) F. Santoro and V. Barone, *Int. J. Quantum Chem.*, 2010, **110**, 476-486.